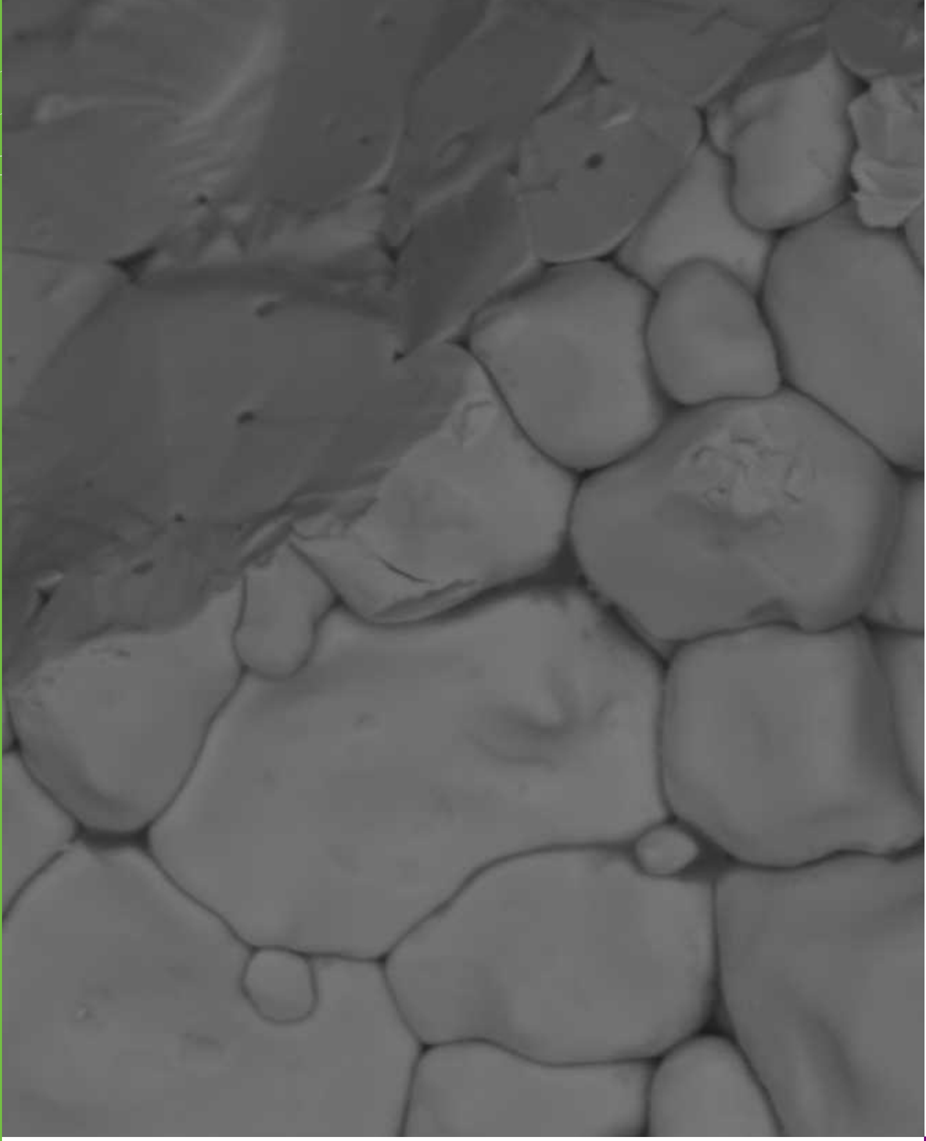

SCIENCE•TECHNOLOGY•RESEARCH HIGHLIGHTS•VISIONS

Dissertation
156

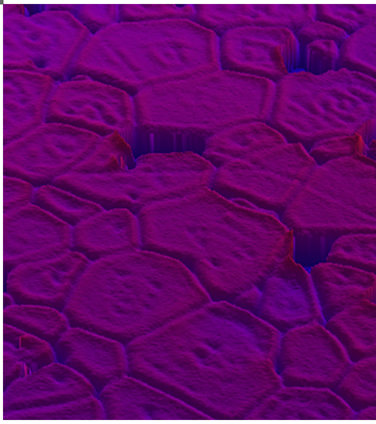

Investigation of ThO_2 as a structural analogue for spent nuclear fuel dissolution under repository conditions

Emmi Myllykylä

VTT SCIENCE 156

Investigation of ThO_2 as a structural analogue for spent nuclear fuel dissolution under repository conditions

Emmi Myllykylä

ACADEMIC DISSERTATION

To be presented, with permission of the Faculty of Science of the University of Helsinki, for public examination in lecture hall A110, Deparment of Chemistry, on 16th of June 2017, at noon.

ISBN 978-951-38-8547-2 (Soft back ed.)
ISBN 978-951-38-8546-5 (URL: http://www.vttresearch.com/impact/publications)

VTT Science 156

ISSN-L 2242-119X
ISSN 2242-119X (Print)
ISSN 2242-1203 (Online)
http://urn.fi/URN:ISBN:978-951-38-8546-5

JULKAISIJA – UTGIVARE – PUBLISHER

Teknologian tutkimuskeskus VTT Oy
PL 1000 (Tekniikantie 4 A, Espoo)
02044 VTT
Puh. 020 722 111, faksi 020 722 7001

Teknologiska forskningscentralen VTT Ab
PB 1000 (Teknikvägen 4 A, Esbo)
FI-02044 VTT
Tfn +358 20 722 111, telefax +358 20 722 7001

VTT Technical Research Centre of Finland Ltd
P.O. Box 1000 (Tekniikantie 4 A, Espoo)
FI-02044 VTT, Finland
Tel. +358 20 722 111, fax +358 20 722 7001

Juvenes Print, Tampere 2017

CONTENTS

Supervised by

Associated Prof. Marja Siitari-Kauppi
Department of Chemistry
University of Helsinki

Senior Scientist, Kaija Ollila
VTT Technical Research Centre of Finland Ltd

Reviewed by

Prof. Nicolas Dacheux
Université Montpellier
Marcuole Institute for Separative Chemistry

Dr. Ian Farnan
Reader in Earth and Nuclear Materials
Department of Earth Sciences
University of Cambridge

Dissertation Opponent

Prof. Mats Jonsson
Applied Physical Chemistry
KTH Royal Institute of Technology

I would like to dedicate this thesis for the memory of my beloved grandfather.
He was the one, who taught me noble skills of debate and argument at the age of two.

ACKNOWLEDGEMENTS

"Sometimes you have to go up really high to understand how small you really are." - Felix Baumgartner

The Ph.D. journey has been like a long and challenging hiking path with slippery rocks, steep slopes, strong wind, refreshing rain and sometimes warm sunshine. From such an adventure, you cannot survive without excellent gear, skills and attitude. The bigger the challenge, the more crucial is the company and assistance of others. From this thesis project, I would have not survived without the help of others.

First of all, I like to express my warmest appreciation and thanks to my supervisor Marja Siitari-Kauppi, who has encouraged me and guided me through this. I have really enjoyed working with her, and she believed in me even on those very moments I did not. Special thanks go to three unique ladies, Kaija Ollila, Riitta Zilliacus and Maija Lipponen, who have long experience in research and science. I have been privileged to learn from them about dissolution studies and ICP-MS analytics. Thanks also to Professor Jukka Lehto and team leader Kari Rasilainen. They have provided good environment to conduct the research and write the thesis at the University of Helsinki and at VTT Technical Research Centre of Finland.

The research of this thesis has been mostly conducted in the frame of the EU project, REDUPP (2011-2014), funded from the European Atomic Energy Community's Seventh Framework Programme (FP7) under grant agreement No. 269903. Posiva, SKB, VTT, are acknowledged as partners of the REDUPP project. The research was continued in the PANCHO project in the research program SAFIR2018, and in the YTERA and the CHEMS doctoral schools. All are acknowledged for their financial support for this thesis.

I am grateful to all collaborators. Collaboration is the special spice of science, which makes research more inspiring and motivating. Special thanks go to REDUPP project group; Lena, Claire, Neil, Martin, Daniel, Pablo, Peter, Marjut, Piia, Kastriot, Christopher and Virginia. It was inspirational and supportive to collaborate with you! In addition, Jukka Marmo and Marja Lehtonen from the Finnish Geological Survey (GTK), whose knowledge and skills have helped me to produce better research results, are greatly acknowledged. Thanks, Kerttuli and Lauri from University of Helsinki, you have made a special contribution to this research with your skills and work.

Merja, I am grateful for your friendship and having a colleague like you at VTT. You have always had time for the ruminative discussions when those were needed, either to clarify results or my thoughts. I am also very thankful from the support and help I have received from my co-workers Tiina L, Jaana, Kirsti, Tiina H, Ulla, Perttu, Jori, Tommi, Wade and all others in the nuclear waste management team. Warm thanks to my family, relatives and friends, especially to my sister Meeri and my dad, you all know how important you are for me and I know that we are in each other thoughts, even if we have not seen each other for a while. You all have been there for me in up-hills and downhills. There is still a special bunch of friends to

be thankful to; the members of the volleyball team Kivenlahden Kiri. We all share a common passion - volley; our friendship and time we have spent together has been important for me to keep the balance in my life during this long project. Last, but not least, Mikko, the man I share my life with. Thanks for being there for me, especially on those days when continuous headwinds have blown and heavy rain has fallen on my (Ph.D.) hiking path.

Thank you all, you know you have special places in my heart!

“It always seems impossible, until it’s done” - Nelson Mandela

Espoo, 3 of May 2017

ABSTRACT

Currently, the preferred option for the long-term disposal of spent nuclear fuel (SNF) and potentially for future thorium-based fuels in Finland and Sweden is disposal in a geological repository. In deep bedrock, the release of Th, U and other radionuclides through man-made barriers and the geo- and biosphere will be controlled by the dissolution of the fuel by groundwater. Thorium dioxide is isostructural to uranium dioxide, sharing the same fluorite structure (space group Fm3m) and making it a useful analogue material for nuclear fuel, which mainly consists of UO_2 (>95%).

This thesis aimed to investigate the dissolution of ThO_2, which was synthesised to approximate as closely as possible the microstructure of UO_2 in a nuclear fuel matrix. The investigation consists of dissolution studies conducted using pellets, fragments (2 to 4 mm) and particles (80 to 160 µm) of $^{232}ThO_2$. The evolution of dissolving surfaces and grain boundaries were examined by combining different microscope imaging techniques (scanning electron microscopy (SEM), atomic force microscopy (AFM), SEM with electron backscattering diffraction detector (SEM-EBSD) and profilometer imaging). Part of the dissolution experiments were conducted in the presence of a ^{229}Th tracer to gain additional data on the dissolution and precipitation by following the change in isotopic ratio $^{229}Th/^{232}Th$. Furthermore, the pellets from these experiments were measured with direct alpha spectrometry to estimate the contents and thickness of the ^{229}Th-rich layer formed on the pellet surface.

The results of all dissolution studies showed a relatively fast release of thorium during the early stage of the experiment followed by a slow decrease in the thorium concentration and suppression of the dissolution rate as the experiments continued over 100 days. Microscopic studies revealed that the grain boundaries play a significant role in the initial release of thorium. It was also observed that the different surfaces of thorium dioxide particles behave differently either dissolving, precipitating or showing an almost inert nature, most likely due to the different surface energies of the heterogeneous material.

High-resolution (sector field) inductively coupled plasma mass spectrometry (SF/HR-ICP-MS) was used for the thorium isotope analyses of leached solutions. The developed method was powerful for analysing thorium isotopes. In addition, alpha spectrometry was used for thorium analysis for comparative purposes. The alpha spectrometry yielded a lower detection limit for ^{229}Th and a higher detection limit for ^{232}Th than SF-ICP-MS, which was 1×10^{-12} mol for both isotopes. Thus, these methods provided comparable results for the analysed ^{229}Th concentration. However, the chemical separation needed before alpha spectrometry is very time consuming compared to the sample preparation necessary for HR-ICP-MS.

When combined with simulations, direct alpha analysis confirmed that during leaching a new layer, with a maximum thickness of 0.1 µm, formed on the surface of ThO_2 pellets. Alpha spectrometry also provided interesting insight into the dissolution and co-precipitation behaviour of ^{229}Th and ^{232}Th decay series daughter nuclides. The surface layer contained not only ^{229}Th and its daughters, but also an elevated concentration of daughters from the ^{232}Th decay series, indicating that they were first released from the bulk during the leaching experiment, subsequently co-precipitating or adsorbing onto the surface of the pellet.

LIST OF ORGINAL PUBLICATIONS

I. Emmi Myllykylä, Tiina Lavonen, Martin Stennett, Claire Corkhill, Kaija Ollila and Neil Hyatt. Solution composition and particle size effects on the dissolution and solubility of a ThO_2 microstructural analogue for UO_2 matrix of nuclear fuel, Radiochim. Acta 2015; 103(8): 565–576.

II. Claire L. Corkhill, Emmi Myllykylä, Daniel J. Bailey, Stephanie M. Thornber, Jiahui Qi, Pablo Maldonado, Martin C. Stennett, Andrea Hamilton and Neil C. Hyatt. Contribution of Energetically Reactive Surface Features to the Dissolution of CeO_2 and ThO_2 Analogues for Spent Nuclear Fuel Microstructures, ACS Applied Materials & Interfaces, 2014; 6: 12279−12289.

III. Emmi Myllykylä, Tiina Lavonen, Lauri Koivula, Kaija Ollila and Marja Siitari-Kauppi. Dissolution of ThO_2: study of dissolution process with initial ^{229}Th spike, Journal of Radioanalytical & Nuclear Chemistry, 2017; 311(1): 225–235.

IV. Emmi Myllykylä, Lauri Koivula, Merja Tanhua-Tyrkkö, Kerttuli Helariutta, Tiina Lavonen, Kaija Ollila and Marja Siitari-Kauppi. Direct alpha spectrometry for analysing the leached ThO_2 pellets, Journal of Nuclear Materials (submitted 28 December 2016).

The author was responsible for the thorium analyses using high-resolution sector-field inductively coupled mass spectrometer (SF-ICP-MS), carried out at VTT Technical Research Centre of Finland (articles I, II and III).

The author planned and executed all dissolution experiments in article I and wrote the article. The ThO_2 pellets were fabricated by the co-authors at the University of Sheffield. Micrometre scale ThO_2 fragments were produced using the Selfrag pulse fragmentation apparatus at the Geological Survey of Finland (GTK). SEM imaging was performed by the author at GTK under the supervision of Marja Lehtonen.

The ThO_2 dissolution experiments described in article II were conducted at the University of Sheffield. The author participated in the ThO_2 work during her research visit to Sheffield. She participated in the surface analysis using several microscopic techniques (VSI, AFM and SEM-EBSD) under the supervision of Claire Corkhill and took part in writing article II.

The author planned and initiated the dissolution experiments conducted in article III. The author performed the radiochemical separations of the solutions and partially carried out the alpha measurements (articles III and IV). She wrote the first and final drafts of articles III and IV. The advanced alpha-spectrometric simulations (AASI) were carried out by the co-authors.

ABREVIATIONS

AASI	Advanced alpha-spectrometric simulation
AFM	Atomic force microscopy
BSE	Backscattered electrons
CCD	Charge coupled device
EBSD	Electron backscatter diffraction
GTK	Geological Survey of Finland (Geologian tutkimuskeskus)
HR-ICP-MS	High resolution inductively coupled mass spectrometer
IAEA	International Atomic Energy Agency
ICP	Inductively coupled plasma
ICP-MS	Inductively coupled plasma mass spectrometry
ICP-OES	Inductively coupled plasma optical emission spectrometer
IRF	Instant release fraction
LIBD	Laser-induced breakdown detection
MS	Mass spectrometry
PFA	Perfluoroalkoxy
PP	Polypropylene
REE	Rare-earth elements
SEM	Scanning electron microscopy
SF-ICP-MS	Sector field inductively coupled plasma mass spectrometer
SNF	Spent nuclear fuel
VSI	Vertical scanning interferometry
XRD	X-ray diffraction

1. INTRODUCTION

Plans have been laid to dispose spent nuclear fuel (SNF) in a geological repository at a depth of over 400 m in bedrock. The repository concept consists of a multiple barrier system, including a copper canister with a cast-iron insert, a bentonite buffer surrounding the canister, backfill materials of the excavated tunnels and, finally, the bedrock itself. However, under anoxic conditions, the fuel matrix UO_2 has a very low solubility and functions as the first release barrier for most fission products. Thus, the release of radioactivity from the repository is controlled mostly by the dissolution of spent fuel by groundwater. There are some isotopes, fission gases (Xe,Kr) and volatile elements (I, Cs and Cl), which are expected to be released rapidly, if the metal waste package and fuel cladding will breakdown. These isotopes are considered to represent the instant release fraction (IRF), which is not limited by the UO_2 matrix. However, some uncertainties associated with an understanding of the dissolution behaviour of the fuel still remain. For instance, we do not yet understand the contribution of energetically reactive surface sites on the dissolution rate of UO_2. The fractional dissolution rates of SNF vary in the range 10^{-6} to 10^{-8} per year, indicating that complete dissolution occurs either within 1 million or 100 million years, respectively. In nature, uraninite ores (UO_2) are known to be stable under diminishing conditions for far longer than 100 million years, that is, for periods of billions of years. In general, experimentally conducted dissolution rates are often found to be higher than the corresponding weathering rates in nature. When crushed UO_2 samples have been leached sequentially, the dissolution rates of UO_2 also appeared to decrease, indicating the progressive stabilisation of dissolving surfaces as they re-leach. [1-11]

The EU-funded project REDUPP (Reducing Uncertainty in Performance Prediction) aimed to reduce the uncertainties related to the dissolution of the UO_2 matrix of SNF. In addition to UO_2 dissolution under natural groundwater conditions, dissolution studies were conducted using the analogue materials ThO_2 and CeO_2. Although having a similar fluorite than UO_2, ThO_2 as an analogue material is not redox sensitive, which allows for the analysis of dissolving surfaces using different microscopic techniques without the problems associated with oxidation during surface analysis. Whereas, Ce may appear with two oxidation states; Ce^{3+} and Ce^{4+}, but lacks the alpha active characteristics of U and Th. [12].

Significant discrepancies in the literature exist regarding the solubility values of sparingly soluble ThO_2 and the hydrolysis constants of Th [13-15]. These discrepancies most likely stem from thorium’s tendency towards polynucleation, colloid formation and adsorption onto surfaces accompanied by the very low solubilities of Th(IV) hydroxide and hydrous oxide. The solubility product values vary depending on the crystallinity of ThO_2. Many previous dissolution studies [16-19] were conducted with the amorphous phases, yet some studies [21] were performed using crystalline ThO_2.

Crystalline ThO_2 is sparingly soluble and the solubility of thorium hydroxide is even lower than ThO_2(cr) requiring a quite sensitive analytical method in order to measure the thorium concentration in leached solutions. Traditionally, alpha active nuclides such as thorium have been measured using radiometric techniques, such as alpha spectrometry. Since techniques exploiting inductively coupled plasma (ICP), such as ICP optical emission spectrometry (OES) and ICP mass spectrometry (MS) have become more common in laboratories, their application in thorium analysis has also increased. In this study, the double focusing sector field ICP-MS with a higher sensitivity than conventional quadrupole ICP-MS was used to analyse thorium in leached solutions.

The next generation application of nuclear energy appears to be interest towards ThO_2 based fuels. ThO_2 possesses many beneficial properties such as a high-fusion temperature, resistance against radiation damage, a good sintering capability, a greater abundance in the Earth's crust compared to U and the possibility of transmutation [22]. However, a number of issues remain related to the availability and accuracy of the nuclear and material properties of ThO_2, all of which require resolution before its commercial use as a fuel may move forward [23]. Additional knowledge is needed, for example, from the microstructural behaviour, matrix dissolution behaviour and irradiation history of ThO_2 [22].

This thesis aims to investigate the dissolution of $ThO_{2,}$ which was synthesised to approximate as closely as possible the microstructure of UO_2 in the nuclear fuel matrix. In addition to aqueous analyses, the surfaces of ThO_2 were studied by applying atomic force microscopy (AFM), vertical scanning interferometry (VSI), electron backscattering diffraction (EBSD) and scanning electron microscopy (SEM). Furthermore, sector field inductively coupled plasma mass spectrometry (SF-ICP-MS) was used for the thorium isotope analyses of leached solutions. In addition, alpha spectrometry was used to analyse thorium for comparative purposes. Direct alpha analysis with simulations were applied to investigate the surface processes from leached pellets. Figure 1 provides a schematic view of the contents of this thesis and the accompanying articles upon which it is based.

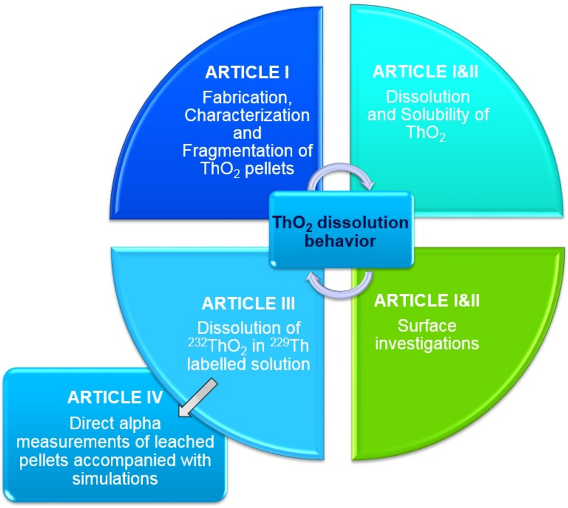

Figure 1. Schematic view of the contents of this thesis and the articles upon which it is based.

2. BACKGROUND

2.1 History and utilization of thorium

As early as 1815, Swedish chemist and mineralogist Berzelius thought that he had identified a new element from a rare mineral, naming it thorium after Thor, the Norse God of thunder and weather in Scandinavian mythology. Unfortunately, ten years later, that mineral turned out to be xenotime (yttrium phosphate) [24-25].

In 1828, Reverend Morten Trane Esmark discovered a black mineral from Løvøya Island in the county of Telemark in Norway. He gave this interesting specimen to his father, Jens Esmerk, a noted mineralogist and professor at the University of Oslo [26]. The elder Esmerk was unable to identify the unknown mineral and sent it to Berzelius, who published his findings in 1829 identifying the new element as the thorium-form silicate mineral 'thorite' ($(Th, U)SiO_4$). [27-30]

Thorium was initially used as a light source in portable gas mantles in 1884 by C. Auer von Welsbachand. The mantle produces a bright light from the incandescence of very hot ThO_2 when heated in a gas flame. Later in 1898, two scientists—German chemist Gerhard Carl Schmidt and the Polish-French physicist Marie Curie—independently identified its radioactive properties. Thorium was the second element identified as being radioactive. Two years earlier in 1896, Henri Becquerel had discovered the radioactivity of uranium [31-33].

Previously, thorium was used as an alloying agent to produce strong alloys. Thorium coating of tungsten welding rods is used to provide a hotter arc. The coating is also applied to electronic equipment, in which it improves the emission of heated tungsten cathodes. In addition, thorium oxide has been used to produce high-temperature crucibles and glass with a high index of refraction for optical applications such as high-quality lenses for cameras and scientific instruments. ThO_2 is also used as a chemical catalyst for example in the conversion of NH_3 to HNO_3 and in the production of H_2SO_4 [24-25].

2.2 Thorium in nature

Thorium enjoys a relatively high abundance in nature. Whilst sources in the literature vary, the abundance in the Earth's crust varies from 8 ppm to 10 ppm [22, 34]. This is roughly 3.5 times more abundant than uranium (2.3 ppm) and almost equals that of lead. However, due to its low solubility, thorium concentrations in natural waters appear fairly low, reaching levels of less than 1 µg/L in oxidic ground waters and approximately 1.5 ng/L in seawater. For uranium, concentrations vary from 0.1 ug/L to 1 mg/L in ground waters and from 2 ug/L to 4 ug/L in seawaters. [34]

Thorium occurs in nature as a nearly pure ^{232}Th isotope, containing less than one part in 10^{10} of ^{228}Th originating from its own decay chain (4n family) [24-25]. Thorium appears in association with uranium and rare-earth elements (REE) in diverse minerals: as veins of thorite ($ThSiO_4$), as thorianite (ThO_2), as uranothorite ($(Th,U)SiO_4$) and as monazite $(Ce,La,Nd,Th,Y,Dy,Sm)(PO_4)$. As a result of isostructuralism to uranium dioxide, ThO_2 and

UO_2 form solid-state solutions with names depending on the uranium content of mixtures. Thorianite contains 75 to 100 mol % of ThO_2, urananothorianite 25 to 75 mol % of ThO_2, thorian uraninite 15 to 25 mol % of ThO_2 and uraninite 0 to 15 mol %. In addition, thorium minerals accompany rock types including syenites, pegmatites, granites and other acidic intrusions [22]. If uranium is present in the same ore, the isotopes ^{231}Th and ^{227}Th from a decay chain of ^{235}U present in quite minor quantities. The decay chain of ^{238}U also generates ^{230}Th and ^{234}Th isotopes [24-25]. Figure 2 illustrates the decay chains of natural ^{232}Th and ^{238}U isotopes. The primary source of thorium is monazite, a lanthanide phosphate mineral. The thorium contents of monazite can grow to as high as 12% [34]. Thorium minerals are known to be sparingly soluble and chemically inert [22, 24-25].

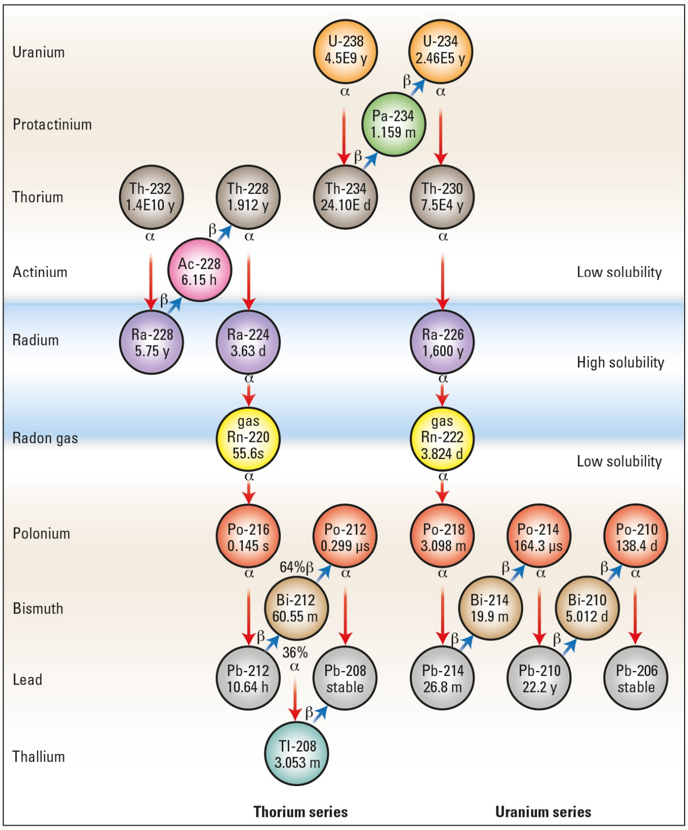

Figure 2. The decay series of natural isotopes ^{232}Th and ^{238}U, which produce minor amount of other Th nuclides in nature (Reproduced from Nelson et al. [35]).

Artificial isotope ^{229}Th is commonly used in the yield determination of alpha spectroscopy for natural Th isotopes [34]. ^{229}Th stands as the first product from the alfa decay of man-made ^{233}U decay series [24-25]. The reaction between ^{232}Th and thermal (slow) neutrons leads to the formation of fissionable ^{233}U as follows:

$$^{232}\text{Th}(n,\gamma)\,^{233}\text{Th} \rightarrow \beta- + {}^{233}\text{Pa} \rightarrow \beta- + {}^{233}\text{U} + \alpha \rightarrow {}^{229}\text{Th} \qquad [34].$$

This reaction is the main reason ^{232}Th is considered nuclear material under International Atomic Energy Agency (IAEA) and Euratom legislation, meaning that it is regulated under nuclear safeguards (that is, the record keeping for nuclear bomb materials). [36-38]

2.3 Chemistry of thorium

Thorium carries the atomic number of 90 with the electron configuration of $[\text{Rn}]6d^27s^2$, meaning that it has four electrons on the outer electron shells. In practice, this means that thorium appears only in the oxidation state +IV [34].

Elemental thorium is a bright silvery metal that turns black when exposed to air because it forms oxide [24-25]. Yet, thorium is a member of the actinides in the periodic table of elements, while the chemistry of thorium resembles that of Group 4 metals Ti, Zr and Hf [34]. Natural thorium is relatively weakly radioactive due to the long half-life (1.4×10^{10}) of isotope ^{232}Th. Its low radioactivity and the single prevailing oxidation state are the primary reasons thorium is commonly used as a chemical analogue for other tetravalent actinide ions (U^{4+}, Np^{4+} and Pu^{4+}) in conditions where other actinides may have several oxidation states.

Thorium is the largest tetravalent actinide ion and the least hydrolysable. In contrast to redox active uranium, thorium has only one prevailing oxidation state Th(IV) under natural conditions. The prevailing form of thorium at pH ≤ 1 is Th^{4+} ion, after which it starts to form a hydrolysed species. In weak solutions, this leads to the formation of mononuclear mono-, di-, trihydroxy species between pH 1 and 4. At pH 4, $Th(OH)_4$ begins to prevail [34]. At higher concentrations, polynuclear species such as $Th_2(OH)_2^{6+}$, $Th_4(OH)_8^{8+}$ and $Th_6(OH)_{15}^{9+}$ appear and colloids form easily at moderately high concentrations. Figure 3 illustrates the Th speciation in 0.1 M NaCl with low and high total thorium concentrations. In general, Th^{4+} forms weak complexes because it is a large tetravalent ion. However, it has moderately strong complexes with fluoride, sulphate, phosphate and carbonate, all of which may increase the solubility of thorium. In aquatic environments, the carbonate complex formation is particularly important, affecting thorium solubility [24-25,34]. A one order of magnitude increase in $[CO_3^{-2}]$ has been shown to increase the solubility of hydrous ThO_2(am) by up to five orders of magnitude [39]. In addition, two mononuclear carbonate complexes of Th(IV), $Th(OH)_3CO_3^-$ and $Th(CO_3)_5^{6-}$ have been reported [39-40]. In the Th(IV)-H_2O-CO_3^{2-} system, a considerably higher Th(IV) solubility indicated the presence of highly charged a pentacarbonate species [39). Kim et al. [41] have thermodynamically modelled the formation of ternary complexes such as $Th(OH)_3CO_3^-$, $Th(OH)_2(CO_3)_3^{4-}$,$Th(OH)(CO_3)_5^{5-}$, $Th(OH)_2CO_3$(aq), $Th(OH)_2(CO_3)_2^{2-}$,$Th(OH)_4(CO_3)^{2-}$, finding that these aqueous Th(IV) species most likely predominate under many natural conditions.

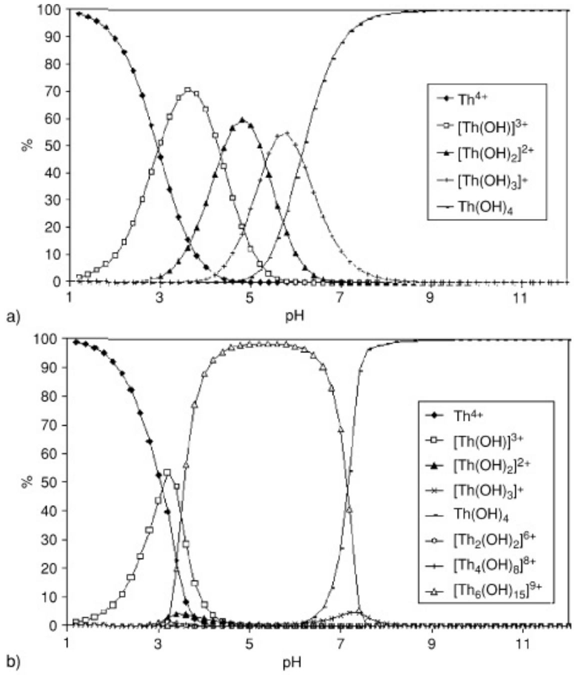

Figure 3. Th speciation in a non-complexing aqueous solution calculated for 0.1 M NaCl using the PHREEQC program. (a) Species distribution for low concentrations of Th(IV) (= 10^{-8} M). (b) Species distribution for $[Th_{tot}]$ = 0.1 M considering the possible formation of only three polynuclear species [24-25].

2.4 Characteristics of thorium dioxide

Thoria (ThO_2 (s)), also called thorianite, is a white, solid oxide with a fluorite structure (space group Fm3m). ThO_2 is somewhat hygroscopic and has the highest melting point, 3350°C, of all oxides. In comparison, the melting point of UO_2 is 2800°C [22]. Sintered thorium oxide is also one of the most refractory substances known [24-25]. The solubility of thoria is known to be quite low; according to the literature, aqueous nitric acid with a small percentage of HF or sodium fluorosilicate can provide a reasonable amount of Th in solution [24-25]. Figure 4 illustrates the solubility curves for crystalline thorium dioxide and amorphous $Th(OH)_4$ based on literature values with some experimental values expressed with symbols [42-43]. As we see here, ThO_2 is sparingly soluble and the solubility of Th^{4+} hydroxide and hydrous oxide appear even lower. As previously mentioned, thorium also has a strong tendency towards polynucleation and colloid formation, and hydrolysed species have a strong tendency towards sorption onto surfaces. All of these features of thorium, together with its very low solubility, stand as the primary reasons why large discrepancies in the oxide/hydroxide solubility products and hydrolysis constants appear in the literature [13-14].

The solubility product values vary depending of the crystallinity and crystalline size of thorium dioxide and the hydroxide or oxohydroxide phase. According to the literature, the solubility product value ($\log K{\circ}\mathrm{sp}$) for ThO_2 (microcryst.) is −53 ± 0.5, whereas the value for amorphous $Th(OH)_4$(am) is −46.7 ± 0.9 [42, 44-45].

Figure 4 also provides the calculated and experimental solubility of ThO_2(cr) in comparison to that of Th(IV) hydroxide or hydrous oxide [45]. The experimental data for ThO_2(cr) includes the values determined by titration–laser-induced breakdown detection (LIBD). In this figure, we also see the data for crystalline ThO_2 presented by Moon [43]. In addition, the solubility data for amorphous precipitates were taken from several sources [40, 43, 45-48]. The solubility curves were calculated for two kinds of solids, based on the hydrolysis constants selected by Neck and Kim (2001) and on the solubility products $\log K^{\circ}_{sp}(ThO_2\,(cr)) = -(54.2 \pm 1.3)$ [49] and $\log K^{\circ}_{sp}(Th(OH)_4\,(am)) = -(47.0 \pm 0.8)$ [45,50].

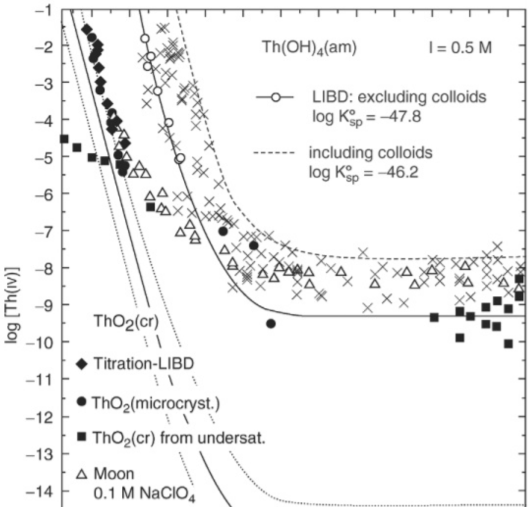

Figure 4. Experimental (symbols) and calculated data (curves) for the solubility of thorium dioxide by Neck et al. [42] and the references therein [40, 43, 45-48, 50]. The solid symbols describe the solubility data for ThO_2(cr) by Neck et al. 2003 and the open triangles represent the data by Moon [43]. The solubility data for amorphous precipitates, determined in the references mentioned above are expressed using the × symbols [42].

Figure 4 illustrates that the crystalline phases follow the solubility of ThO_2(cr) under acidic conditions. However, above pH 3, dissolved thorium starts to hydrolyse and form amorphous phases, leading to the solubilities near amorphous thorium oxide/hydroxide.
A comparison of the solubilities of crystalline and amorphous thorium oxide to the solubility values found in this study are presented in chapter 5.2.5 below.

Some of the solubilities from undersaturated dissolution experiments are below the expected equilibrium values. In these experiments, the equilibrium might not have been reached, because ThO_2(cr) has very slow dissolution kinetics [21, 43, 45]

The results of Hubert et al. [21] indicated that the high temperature crystallized ThO_2 was two orders of magnitude less soluble than hydrous ThO_2. They also suggested that the sintering temperature and precursor used affected the specific surface area, surface state and size of the aggregates, thus also affecting ThO_2 dissolution. In addition to the degree of crystallinity, other factors may affect the dissolution of ThO_2. For example, the effects of the surface morphology, such as the grain boundaries and crystallographic defects, have been discussed in the literature [21, 14, 24].

In general, quite often minerals such as feldspar and quartz exhibited experimental dissolution rates higher than the corresponding weathering rates under natural conditions [6-9]. Often, sample preparation under laboratory conditions creates sharp edges and other surface defects. Atoms located at the point of the defect or irregularity in the structure exhibit fewer chemical bonds and a higher surface energy than atoms in bulk, leading to their removal during dissolution. The dissolution rates of UO_2 decreased when the same crushed UO_2 samples were leached sequentially. This indicates a progressive stabilisation in the dissolving surfaces as they are re-leached [10-11].

According to the dissolution theories of crystalline structures, the saturation state of the solution and the surface energy of the dissolving surface control the dissolution mechanisms and changes in topography [51-52]. In under-saturated conditions, the surface tends to lose atoms, causing the nucleation of new etch pits consequently increasing the surface area. However, the formation of new each pit is limited by the appearance of higher energy sites, such as kink and step sites (see Figure 5) which tend to dissolve faster. Thus, the principle of minimising surface energy is typically linked to the minimisation of the density of high-energy surface sites and surface areas.

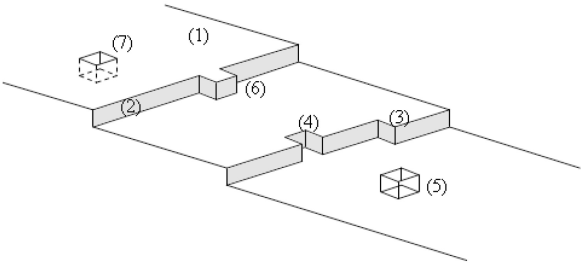

Figure 5. Schematic view of the evolving surface, including topological features such as (1) terrace, (2) step, (3) kink-site, (4) vacancy at a step, (5) adatom on a terrace, (6) adatom at a step and (7) vacancy on a terrace mofified from [53].

2.5 The role of spent nuclear fuel in final disposal

Finland and Sweden stand at the forefront of planning and building facilities for the final disposal of SNF. SNF is a quite complex and challenging material. After fissioning in a reactor, it still primarily consists of uranium oxide (96%). Other fractions consist of fission products (3%) and transuranium elements (1%), which are either incorporated into the UO_2 fuel matrix or migrated to the grain boundaries or to the gap between the fuel pellet and the zircaloy alloy cover. Thus, recently irradiated fuel is highly active producing alpha, beta and gamma radiation and contains many different isotopes of various periodic table elements. Alpha radiation is considered the dominant radiation field since the lifetime of the fuel increases to close to 10 000 years. In addition, uranium is a redox-active element, meaning that the presence of either oxidative or reductant species in the vicinity of the fuel surface greatly affect the rate of dissolution. UO_2 is orders of magnitude more soluble under oxidative conditions because U becomes a relatively soluble U(VI) instead of a sparingly soluble U(IV) [34].

Various engineered barrier systems have been designed in many countries to keep the fuel rods intact and to isolate the high-level nuclear waste from the environment. The Scandinavian concept is known as KBS-3, in which the fuel bundles are placed in a cast-iron insert surrounded by a copper canister after an average cooling time (30 to 50 years depending on the burnup of the fuel) (see Figure 6). These containers are placed deep underground (400-500 m) and, then, the drill hole in the granitic rock is filled with bentonite clay blocks. However, the first two release-limiting phases can be considered the UO_2 matrix of the fuel and the zircaloy cladding surrounding the pellets in the fuel rod. UO_2 has a fairly low solubility under reducing conditions, which should prevail after the closure of the repository. The geosphere—that is, the bedrock itself—also plays a radiation-shielding and radionuclide migration–regressing role in the barrier system. [54-55]

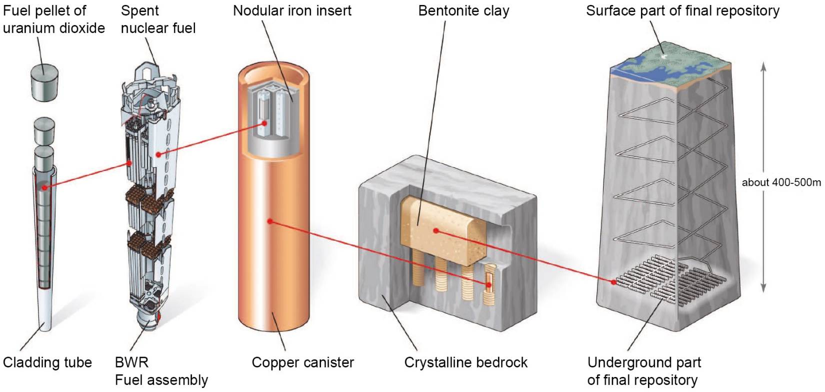

Figure 6. The engineered barrier system of the KBS-3V disposal concept. reproduced with modifications from Sellin and Leupin [55]

2.6 Thorium dioxide as analogue material for Uranium dioxide

After irradiation in the reactor, the matrix of the spent fuel remains primarily uranium dioxide with a fluorite structure (space group Fm3m) as the fission products and heavier actinides incorporate into the structure (see Figure 8). Ceramic oxides such as ThO_2 and CeO_2 have the same fluorite-type structure (see Figure 7) and are relatively sparingly soluble similar to UO_2 under reducing conditions. Thus, they have been used as structural analogues in different UO_2 and fuel behaviour studies [56-58]

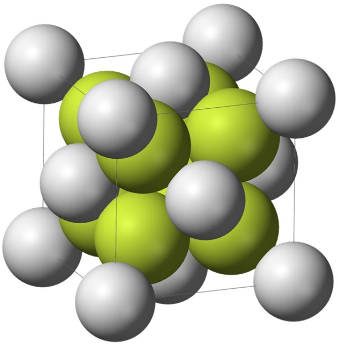

Figure7. Fluorite structure of ThO_2. Grey spheres represent thorium and green spheres represent oxygen atoms [59]. In the fluorite structure of UO_2, Th atoms are substituted by uranium atoms.

The primary difference between uranium and thorium is that U is a redox-active element and has two oxidation states [U(IV) and U(VI)] in nature. Sparingly soluble $U(IV)O_2$ prevails under reducing conditions while $U(VI)O_2$ prevails under oxidising conditions; thorium appears in only one oxidation state Th(IV). However, the redox sensitivity and radioactivity of UO_2 set limitations on the microscopic techniques and research methods that can be applied to uranium dioxide, not to mention highly active SNF. The use of structural analogues such as ThO_2 and CeO_2 becomes valuable, rendering necessary an understanding of the surface behaviours during the matrix dissolution processes. For such purposes, sophisticated microscopic techniques are essential.

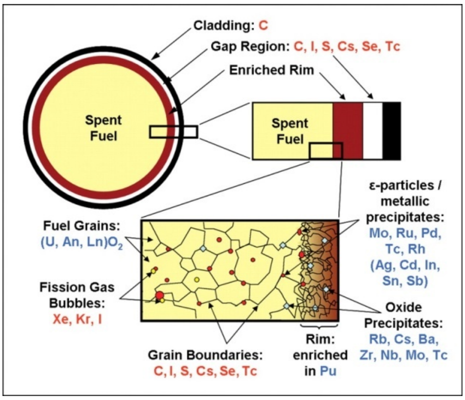

Figure 8. Schematic view of the structural and elemental composition of a spent nuclear fuel pellet inside the cladding illustrating the microstructural variation between the fuel and rim region and the appearance of the elements in the different parts of the structure. Elements in red are released rapidly after initial contact with water. The elements in blue are expected to release as the UO_2 matrix corrodes [60].

As we see in Figure 8, the structure and chemistry of SNF is more heterogeneous and complex compared to the dioxides used as structural analogues or fresh UO_2 fuel. However, the release of the many elements present in the fuel grains, oxide precipitates and metallic precipitates is limited by the UO_2 matrix dissolution. Thus, a profound understanding of the dissolution behaviour of UO_2, ThO_2 and CeO_2, with their fluorite structure, is essential.

Fission gases such as Xe and Kr and volatile elements such as I, Cs and Cl will rapidly release after the breakdown of the metal waste package and fuel cladding. These are already located in the fission gas bubbles, at the grain boundaries or segregated into the gap region between the fuel and zircaloy cladding. These isotopes appear to represent the instant release fraction (IRF), which is not limited by the UO_2 matrix. Their segregation in fuel depends on the fuel burnup and the reactor operating conditions. For example, the temperature gradient from the centre to the edge of the UO_2 pellet during operation represents a critical parameter [60]. Understanding this instant release requires dissolution studies conducted using SNF. However, analogue material studies providing insights of grain and grain boundary evolution during dissolution may explain, for example, the migration behaviour of gases to the gap.

2.7 Thorium dioxide in future fuel concepts

The use of ThO_2 as a nuclear fuel has been researched since the 1950s. As a fuel, thoria possesses many beneficial properties, such as a high fusion temperature, a good sintering capability, resistance against radiation damage, a greater abundance in the Earth’s crust compared to U and the possibility of transmutation [22]. Thus, ThO_2-based fuel is considered a potential advanced fuel for generation IV nuclear energy systems [61]. In addition, the main interests in ThO_2 as a nuclear fuel lie in its potential to burn weapons-grade plutonium [62], its high capability to aqueous corrosion resistance, its very low solubility [21, 63], its isomorphism with other tetravalent actinide dioxides and the production of fewer minor actinides [64]. As a fuel, ThO_2 is generally mixed with other actinide oxides since a fissile isotope such as ^{233}U, ^{235}U or ^{239}Pu is needed to ignite the nuclear reaction in a reactor. The sparingly soluble oxide could even be considered disposed of directly into a deep geological repository. However, as s part of the safety assessment of irradiated nuclear fuel, it is crucial to predict the behaviour of ThO_2 and the release of radionuclides from the fuel. A number of issues related to the availability and accuracy of nuclear and material properties of thoria remain that require resolution before its availability for commercial use as a fuel [23]. For example, the inertness of ThO_2 causes difficulties in dissolving oxide into HNO_3. The short-life daughters of ^{233}U induce high-energy gamma radiation, which challenge reprocessing and refabrication. In addition, thorium causes problems during reprocessing. The thorium fuel cycle produces problematic protactium, also requiring resolution.

In light of waste management, thoria-based fuels seem appealing because ThO_2 is chemically stable and ThO_2 is almost insoluble in groundwater. The highest oxidation state of thorium is +IV unlike that of uranium, which oxides comparatively easily from oxidation state +IV to +VI. Under oxidising conditions, UO_2 can be converted to the relatively soluble uranyl cation UO_2^{2+} and its complexes. But, for ThO_2 fuel, the oxidative dissolution of the matrix is not an issue [22-23]. The low solubility and high chemical stability of thoria represent suitable features for the geological disposal of ThO_2-based fuels. However, the reprocessing path of thorium appears more complex than the PUREX process for UO_2 fuel due to the high stability of ThO_2. The thorium-specified separation process THOREX requires the use of HF for dissolution and should generate 50% to 70% more glass waste in volume than the PUREX process [22].

In UO_2 fuel, the potential environmental release and subsequent radiation are dominated by the instant release of soluble and mobile products which segregate into the gap region between the fuel pellet and the cladding (see Figure 8). The nuclides rich at the grain boundaries may also be released more rapidly in comparison to the matrix dissolution. The matrix dissolution of ThO_2 is likely slower than the dissolution of the UO_2 matrix. The primary cause for the fission gas release to the gap region in UO_2 fuels is the grain growth in the central region of the oxide fuel pellets. These gases and other elements incompatible with the crystal structure are swept from their original locations becoming concentrated at the grain boundaries, thus forming noble metal particles and fission gas bubbles.

Thorium oxide is a slightly better thermal conductor than UO_2. Cation diffusion in ThO_2 is slower and ThO_2 has a higher melting point than UO_2. These minor differences indicate that in the same fuel geometry, microstructure and power history, thorium oxide should run cooler and undergo less grain growth, also producing somewhat less fission gas release. However, our knowledge of the irradiation history, microstructural behaviour and matrix dissolution behaviour of ThO_2 remains limited [22].

3. EXPERIMENTAL

3.1 Fabrication and characterisation of ThO_2 pellets $^{I\ \&\ II}$

Crystalline ThO_2 pellets were made to resemble the microstructure of the UO_2 matrix in fuel pellets [56, 65-66]. The pellets were sintered from ThO_2 powder (British Drug Houses Ltd., lot number G83757/541012). The purity of the powder was confirmed by x-ray diffraction (XRD) prior to sintering. Approximately 1 g of powder was uniaxially pressed in a 10-mm-diameter hardened stainless-steel die with a load of 100 MPa. The sintering temperature varied from 1300 to 1750°C in a standard air atmosphere muffle furnace at a ramp rate of 5°C min^{-1}. The density and grain size increased as the sintering temperature increased. Sintering was optimised at 1750°C (dwell time 4 h) to produce pellets with randomly orientated 10 to 30 µm grains and a 94% density of the theoretical density (10.00 g cm^{-3}) of ThO_2. In addition to the optical microscopy images and pole figures of the annealed pellet surfaces reported in article I, one pellet was measured using confocal profilometry (CP). The confocal profilometers were developed to image the sample surface. Polished surface heights were measured using a profilometer at depths of 0.7 to 10 µm. The pellet was sawed horizontally in the middle and the polished inner and top surfaces of the pellet were imaged using a profilometer and SEM-EBSD.

3.2 Production of ThO_2 fragments for the dissolution experiments ^{I}

Different particle sizes were used to estimate the effect of the surface area on the dissolution rate and solubility of ThO_2. Some experiments were conducted using intact pellets, while all other particles sizes were produced from the same batch of ThO_2 pellets.

Millimetre-size fragments were produced by crushing pellets using a percussion mortar and selecting fragments 2 to 4 mm in size. To minimise the amount of fine fragment surfaces, fragments were sequentially washed with isopropanol and ethanol.

ThO_2 is a hard and refractory material, proving problematic in the production of micrometre particles using a conventional grinding and sieving method. Powders ground by ball mill were contaminated with different ball mill materials, steel and agate.

A solution to this grinding problem was found through the Selgfrag electrodynamic fragmentation method [67-68]. Smaller-sized particles (80–160 µm) were produced from intact ThO_2 pellets using this method, which uses electrical energy in the form of repeated high-voltage pulses. The samples were immersed in a dielectric process liquid—that is, water—which has a high dielectric strength. The voltage rise time was kept below 500 ns. Under such conditions, the discharges are forced to occur through the immersed material. Plasma channels and explosions are generated inside the pellets and the resulting shockwaves produce fracturing and a physical breakdown. Fragmentation using Selfrag was completed at the Geological Survey of Finland (GTK). Fragments smaller than a millimetre produced using Selfrag were washed and magnetically separated from any impurities generated from the apparatus materials during fragmentation. Different size fractions were separated by sieving through different sized sieving canvases. The fraction sizes consisted of the following: <45 µm, 45 to 80 µm, 80 to 160 µm and >160 µm.

3.3 Dissolution and solubility experiments [I]

3.3.1 Pre-experiments

Pre-experiments aimed at conducting ThO_2 dissolution experiments under atmospheric conditions helped to refine the research plan for the more detailed experiments. Pre-experiments were conducted with 2 to 4 mm fragments (m ≈ 300 mg) at 25°C under atmospheric conditions. Simplified groundwater, 50 ml, was added into a polypropylene (PP) test vessel (60 ml). The solution compositions mimicked the salinity and carbonate concentrations at the disposal site (Olkiluoto, Finland). The composition used was one of the following:

- 0.1 M NaCl solution; 30 d pH 5.8, BLANK 5.6 or
- 0.01 M NaCl with 2 mM $NaHCO_3$; 30 d pH 8.2, BLANK 8.3.

The experiments were run in triplicate using an additional blank, which did not contain any ThO_2 in the solution used. Experiments were sampled by withdrawing 2.5-ml aliquot of the solution after leaching for 0, 1, 3, 6, 15, 24, 31, 41, 48, 79, 100 and 115 days. Sample aliquots were filtered using a Pall Mall ultrafiltration device (10 kDa molecular cut off (≈1 nm)) after centrifugation (1 h, 6000 rpm). Filtrated samples were acidified with an ultrapure concentrated HNO_3 (ULTREX II by J.T.Baker) solution, while thorium concentrations were analysed using sector field inductively coupled plasma mass spectrometer (SF-ICP-MS) (Element 2 by ThermoScientific). The evolution of the thorium concentration was followed up for 115 days.

3.3.2 Dissolution and solubility experiments with fragments [I]

This study aimed to investigate the effect of the particle size on the dissolution rate of ThO_2. At the end of the experiments, the solubility levels were compared to the thermodynamic equilibrium data for ThO_2 and $Th(OH)_4$ [NEA/TDB].

Dissolution experiments were conducted using 2 to 4 mm fragments (m ≈ 300 mg) and ThO_2 powder (80 to 160 µm sized particles) at 25°C under Ar atmosphere ($O_2 < 0.15$ ppb in water) under glove box conditions to exclude carbon dioxide dissolution from air into the solution. The experiments were conducted using two different solutions:

- 0.1 M NaCl with an initial pH of 8 or
- 0.01 M HNO_3 with an initial pH of 2.

In a nitric acid solution, the aqueous phase (50 ml) was added in a high-density PP test vessel (60 ml). The experiments using 0.1 M NaCl solution were carried out in perfluoroalkoxy (PFA) Teflon vessels in order to decrease the potential adsorption of Th to the reaction vessel under near-neutral conditions.

The experiments were run in duplicate with an additional blank, and sampled by withdrawing 2.5-ml aliquot of the solution after leaching for 0, 1, 2, 5, 7, 9, 14, 21, 30, 43, 57, 70 and 89 days. Sample aliquots were filtered using the Pall Mall ultrafiltration device (10-kDa molecular cut off (≈1 nm)) after centrifugation (1 h, 6000 rpm). Filtrated samples were acidified using an ultrapure concentrated HNO_3 (ULTREX II by J.T.Baker) and thorium concentrations were analysed using SF-ICP-MS (Element 2).

Dissolution rates were calculated from the thorium released from the solid phase to the solution.

3.3.3 Dissolution experiments for surface investigations I & II

The highly radioactive nature of SNF and the redox properties of uranium provide many limitations to using microscopic techniques to investigate the surface characteristics of SNF or the UO_2 matrix during dissolution. In this part of the study, the evolution of the surfaces of the analogue actinide oxide material ThO_2 was observed by different surface characterization and microscopic techniques. As such, this phase focused on gaining insights into surface phenomena taking place on the solid surfaces of materials with a fluorite structure. In addition, article II contains details regarding studies conducted using another analogue oxide, CeO_2. This summary considers only those experiments conducted using ThO_2. However, the supplementary results of the microscopic studies of CeO_2 are used when interpreting the results related to ThO_2.

Dissolution experiments for surface analyses can be divided into two categories:

1. Pre-dissolution study by scanning electron microscopy (SEM) (article I)
2. Dissolution study of the grain boundary inspection using SEM-EBSD and AFM (article II).

The first study was conducted using 80 to 160 µm particles and 2 to 4 mm fragments under an elevated temperature and acidic conditions. Such harsh conditions irrelevant to the final disposal were applied in order to evaluate the appearance of surface changes of an almost insoluble oxide during a relatively short time span (a few weeks). The morphological changes at the particle surfaces were studied using SEM.

The particles or fragments were placed into PP reaction vessels (60 ml) and 50 ml of 1 M HNO_3 (~ pH 1) was added under an Ar atmosphere in the glove box. The reaction vessels were sealed into a steel container under Ar atmosphere and exported from the glove box to a heating chamber and maintained 80°C. The particles and fragments were separated from the acidic solution after two and four weeks, and the solids were studied using SEM (JEOL JSM-900LV, Oxford Instruments) using an accelerating voltage of 20 kV and a beam size of 10 µm at GTK. The results were compared for the surfaces analysed before leaching.

The second surface study (article II) focused specifically on the evolution of the grain boundaries and other surface features of the ThO_2 and CeO_2 analogues during dissolution. It was carried out using polished and annealed ThO_2 pellet surfaces at the University of Sheffield.

Monolith surfaces were ground and polished to a 0.25-µm finish using SiC paper and a diamond paste. The polishing of ThO_2 became a quite complex task. The oxide seemed to pull out grains while polishing, causing new scratches during the polishing process. The final polishing step required the use of a 0.06-µm silica-colloid solution to obtain surfaces flat enough for imaging analysis using EBSD [69] and AFM. After polishing, the grain boundaries were defined by heating to 1500°C (annealing) at a ramp rate of 5°C min^{-1}. The resulting grains ranged in size from 5 to 30 μm, and the grains were randomly orientated.

Integrated imaging using profilometry, EBSD and AFM allowed us to study the surface evolution. The dissolution experiments were performed at a high temperature and in acidic media. The following dissolution experiments were conducted:

- annealed ThO_2 (and CeO_2) dissolution at 90°C in 0.01 M HNO_3.

Dissolution experiments 3 were sampled for thorium analysis at 1, 3, 7, 21, 28 and 35 days. One monolith of each triplicate experiment was removed for surface characterisation at each sampling point and returned into the dissolution solution after analysis.

3.3.4 Dissolution experiments with a ^{229}Th tracer III

The tracer experiments aimed at investigating the initial release of thorium and the dissolution process and behaviour of ThO_2. The tracer was used to evaluate the amount of dissolved and precipitated thorium. In addition, alpha spectrometry was used to validate the ICP-MS data.

The dissolution experiments were conducted using either single solid pellets or 2 to 4 mm particles in a 0.01 M NaCl solution under an Ar atmosphere at 25°C ($O_2 < 0.15$ ppb in water) for 104 days with additional sampling at 534 days. Four experiments (A, B, E, F) were spiked with ^{229}Th in the aqueous phase in the initial stage of the experiment. Parallel experimental series (C, D, G, H) were also conducted without a ^{229}Th spike in the liquid phase as a reference. At the same time, the tracer experiments simulate the oversaturation dissolution experiment, whereas the starting point represents the undersaturation for experiments without a ^{229}Th tracer. Table 1 provides the experimental matrix and Figure 9 shows the experiments with ThO_2 fragments and a single pellet.

SF-ICP-MS (Element 2) was used to analyse the concentration of ^{232}Th and the isotopic ratio of ^{229}Th/^{232}Th in non-filtered samples. Rather exceptional compared to previous studies, the samples here were not filtered to follow the amount of ^{232}Th released from the $^{232}ThO_2$ pellet and the isotopic ratios ^{229}Th/^{232}Th in the aqueous phase.

In addition, the thorium isotopes were also analysed using the alpha spectrometric method for a few selected liquid samples to compare the analytic methods and to validate the mass spectrometric analysis. Prior to alpha detection, thorium was separated using anion exchange chromatography (see Figure 13 in section 4.4) and co-precipitated from solution with CeF. The $(Ce/Th)F_4$ precipitate was measured using the Canberra 450 PIPS detector and the analytical program MAESTRO for Windows Model A65-332.

Table 1. Experimental matrix using 2 to 4 mm particles and solid pellets.

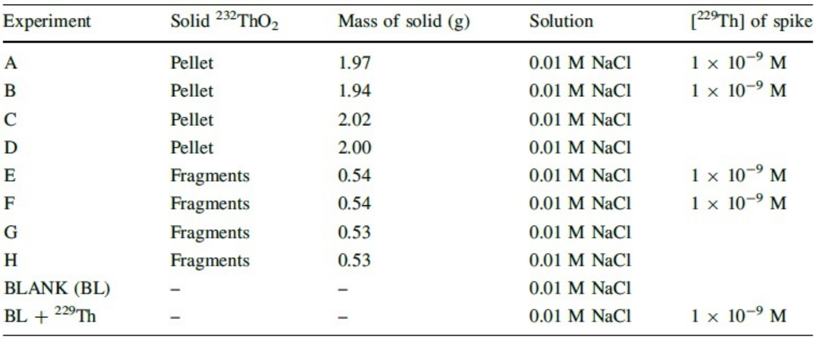

Experiment	Solid $^{232}ThO_2$	Mass of solid (g)	Solution	[^{229}Th] of spike
A	Pellet	1.97	0.01 M NaCl	1×10^{-9} M
B	Pellet	1.94	0.01 M NaCl	1×10^{-9} M
C	Pellet	2.02	0.01 M NaCl	
D	Pellet	2.00	0.01 M NaCl	
E	Fragments	0.54	0.01 M NaCl	1×10^{-9} M
F	Fragments	0.54	0.01 M NaCl	1×10^{-9} M
G	Fragments	0.53	0.01 M NaCl	
H	Fragments	0.53	0.01 M NaCl	
BLANK (BL)	–	–	0.01 M NaCl	
BL + ^{229}Th	–	–	0.01 M NaCl	1×10^{-9} M

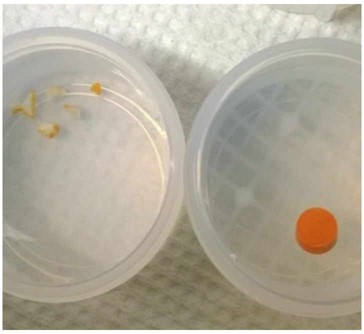

Figure 9. A Picture of the ^{229}Th tracer experiment with fragments and a single pellet of ThO_2.

4. ANALYSIS TECHNIQUES

4.1 Sector field inductively coupled plasma mass spectrometry[I, II & III]

Inductively coupled plasma mass spectrometry (ICP-MS) is the most frequently used analytical method for elements and isotopic ratios in the trace and ultratrace concentration range [70]. Compared to the widely used ICP optical emission spectrometry (ICP-OES), ICP-MS also enables the analysis of different isotopes [71]. The ICP technique permits an easy quantification procedure using aqueous standard solutions and a simple sample introduction in an ion source operating under atmospheric pressure [72].

The basic principle of mass spectrometry is that the elements in the sample—also called the analytes—are atomised, ionised and separated using the mass-to-charge ratio before detection. In the case of a liquid sample, this means that the analytes appearing in molecules, complexes or as atoms in the solution, which are then decomposed and ionised in inductively coupled plasma [70, 73]. The sample liquid is injected into the nebuliser producing a fine mist with the help of a sample gas in the spray chamber, in which the larger droplets are rejected due to gravity and only the finest mist goes to the plasma torch in a stream of the sample aerosol. ICP is an electrode-less discharge formed in gas, maintained by the energy coupled to it from the radio frequency generator [73]. Argon serves as the most used plasma gas to maintain the plasma with a suitable coupling coil, which functions as the primary radiofrequency transformer. The temperature (8000 K) of the ICP torch can vaporise, atomise and ionise elements to a high degree (>90% for most elements) [70]. From the plasma under atmospheric pressure, the positively charged ions are extracted via the interface into the high-vacuum system of the spectrometer. They are then separated through mass filters of either the quadrupole-type time-of-flight, or a combination of electrostatic and magnetic sectors before measurement by an ion detector. The elemental specific mass, ionisation energy and interferences, and the sensitivity of the instrument, affect the achievable detection limit of ICP-MS. Depending upon the element and the instrument used, the detection limits vary from 10^{-15} to 10^{-8} g. Figure 10 shows the inner compartments of the double-focusing SF-ICP-MS instrument (Element 2 by Thermoscientific). In the low-resolution mode, the sensitivity of the double-focusing SF-ICP-MS is generally higher than that achieved using conventional quadrupole ICP-MS instruments, especially for non-interfered and heavy elements, because the magnetic sector entrance and exit-slit design results in flat top peaks [74].

According to Hou and Roos [70], the precision of the isotope ratio measurements using the double focusing SF-ICP-MS with a single ion detection is slightly better than that for the quadrupole ICP-MS (around 0.1% or better vs. 0.1–0.5% for quadrupole). Furthermore, a one order of magnitude better precision for isotope ratio measurements can be achieved by using a multi-ion collector detector in SF-ICP-MS.

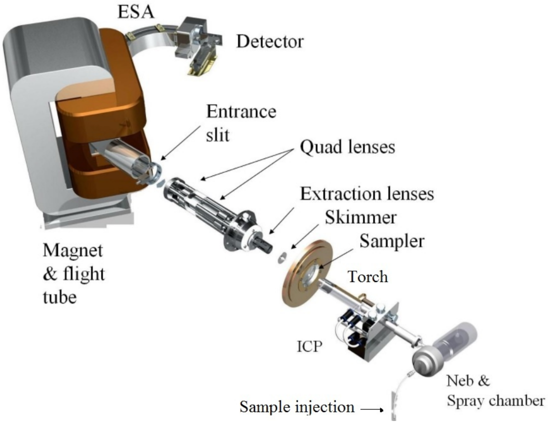

Figure 10. The schematic view of the inner compartments of Element 2, a double focusing SF-ICP-MS instrument. Modiefied from [75].

A better mass resolution for the double-focusing SF-ICP-MS may resolve some of the isobaric and polyatomic interferences that occur nominally at the same mass. These include, for example, the isotopes ^{238}U and ^{238}Pu or ^{75}As from its polyatomic interference of ^{40}Ar^{35}Cl, of which at least the latter can be resolved [70, 76].

An Element 2 SF-ICP-MS by Thermoscientific was used for analysis of ^{232}Th and the isotopic ratio of ^{229}Th/^{232}Th in liquid samples. The concentration of ^{232}Th was examined by applying the counting mode and using a low resolution ($R \approx 300$). The standards for ^{232}Th, containing 0.01, 0.05, 0.5, 1 and 5 ppb of thorium, were diluted with 1 % HNO_3 from Reference Standard solution SQS-01 from Accutrace TM. Same 1 % nitric acid was used as blanks in the analysis sequence. Whereas the samples from the blank experiments were analysed as a samples and were taken into account if they varied from concentration level of 1 % HNO_3.All of the measured samples, standards, and blanks contained 10 ppb of indium, which was used as the internal standard to control for the variation in the pulses. Control samples prepared from a CLMS-1 standard solution (from SPEX) were used to validate the concentration analysis of ^{232}Th. The samples were injected through a SeaSpray nebulizer (0.4 ml/min) and a double-pass spray chamber equipped with a Peltier cooling unit. The sample injection system was washed for 3 min in between sample injections. The detection limit for Th was calculated by multiplying the standard deviation of the ion counts obtained for the sample blanks (ten replicates) with factor of 6 and dividing it by the sensitivity of thorium in 1 ppb standard solution.

Analysis of the isotopic ratio ^{229}Th/^{232}Th was performed using the speed-scanning mode. The main differences in the isotope analytical method included the narrower peak mass and integration windows in comparison to ^{232}Th concentration analytical method. In isotope ratio analysis the samples per peak were also increased to 25 from 10 in ^{232}Th concentration analysis, to acquire more counts with narrower peaks.

4.2 Scanning electron microscopy (SEM) and electron backscattering diffraction detector (EBSD) [I & II]

An SEM microscope uses an electron beam, collimated by electromagnetic condenser lenses, focussed by an objective lens and scanned across the surface of the sample using the electromagnetic deflection coils under a vacuum. The focused beam of the high-energy electrons generates a variety of signals at the surface of the solid specimens from the electron–sample interactions generating information on the sample's external morphology (texture), chemical composition and crystalline structure as well as the orientation of the sample materials [77]. Electron microscopy uses rapidly moving electrons. In comparison to visible light at wavelengths of 4000 to 7000 Å, electrons accelerated to 10 000 KeV have a shorter wavelength of 0.12 Å. While the resolution of optical microscopes is limited to a magnification of about 100 diameters, electron microscopes are capable of magnification reaching roughly 1 000 000 diameters [78].

The collection of secondary electrons released from the sample by the beam represents the primary imaging method produced using SEM. SEM allows imaging of the surface topography in the micro- to nanometre range [77-78]. Because the beam of high electrons generates a variety of signals when interacting with the sample material, several imaging options are available in SEM depending upon the detector mode [78]. Backscattered electron (BSE) imaging uses high-energy electrons that emerge nearly 180° from the illuminating beam direction. The BSE yield is a function of the average atomic number of each point on the sample, thus yielding compositional information showing heavier elements more brightly illuminated and lighter ones less brightly [78].

In article I, the SEM and BSE images of crushed ThO_2 fragments (80 to 160 µm) were captured using JEOL JSM-900L with an accelerating voltage of 20 kV and a beam size of 10 µm at GTK. The images were taken from the original particles after two and four weeks of leaching in nitric acid at an elevated temperature.

Electron backscatter diffraction (EBSD) is a crystallographic and microstructural characterisation technique mounted into SEM. This combined technique is used to study the orientation, structure and phase of crystal and polycrystalline materials. For using the EBSD technique, a sample with a flat and highly polished surface is placed in the SEM chamber at a highly tilted angle (~70°) towards the diffraction camera, and the surface is scanned by a beam of electrons diffracted though the crystal surface. Reflections from the electrons collide with the phosphor screen located in the specimen chamber forming Kikuchi patterns which are imaged via a focusing lens in the charge coupled device (CCD) camera (see Figure 10). The reflection of the crystallographic orientation—the Kikuchi pattern—originating from the structure and the orientation of the crystalline material are compared to the reflection library to identify its structure and orientation [79-80]

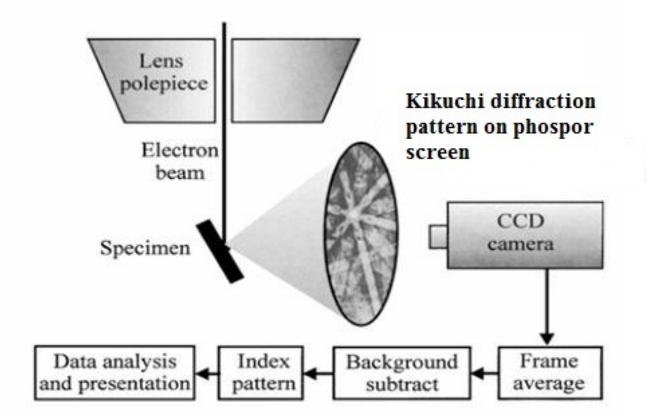

Figure 11. Scheme of the basic EBSD set-up (modified from [81])

EBSD serves as a useful tool for characterising aspects of the crystallographic orientation of microstructures at lengths ranging from tens of nanometres to millimetres. With the advent of high-speed digital cameras and the use of EBSD, using the EBSD detector as an imaging device similar to a backscatter (or forward-scatter) detector has become practical. Using the EBSD detector in this manner enables imaging that allows for a comparison of the topographic, atomic density and orientation contrasts at rates similar to slow scanning using a conventional SEM method. One challenge for EBSD work lies in locating a suitable area along the sample to collect EBSD data [80.].

In article I, EBSD was applied to the analysis of the crystallographic orientation and grain size distribution of the ThO_2 pellet surface. Analyses were performed using EBSD (Oxford Instruments) in conjunction with a Sirion Field Emission SEM. EBSD maps of 100 μm^2 were obtained at an accelerating voltage of 20 kV and a 0.5 µm step size. Grain orientation analysis was performed on >10 000 grains using the HK Channel 5 software (Oxford Instruments).

In article II, SEM-EBSD analyses were accompanied by VSI and AFM analyses. Combining these microscopic techniques allowed us to investigate the evolution of grain boundaries at different misorientation angles. In addition, the analysis of the crystallographic orientation was performed using EBSD (Oxford Instruments, Abingdon, Oxfordshire, UK) in conjunction with an FEI Sirion field-emission SEM. the map size ,accelerating voltage and used software were similar to previous measurement, but the step size was 0.25 µm instead of 0.5 µm.

4.3 Atomic force microscopy (AFM) II

Atomic force microscopy (AFM) is a microscopy technique in which the surface is scanned along the X–Y grid with a sharp tip attached to the cantilever (see Figure 12). The surface topography is imaged by deflecting a laser beam off the cantilever to the photodiode detector and recording the Z position (height variation). The Z position of the tip is adjusted by the feedback mechanism in order to keep the input parameter of the cantilever constant. For the Z axis, a resolution as low as 0.1 nm can be achieved since the resolution of the X–Y direction is about 20 nm. In the contact mode, the tip is in direct contact with the sample and dragged across the surface. Due to the repulsive mechanical force, tip sticking under ambient conditions becomes a disadvantage in the contact mode. Under ambient conditions and in the aqueous phase, most samples develop a liquid meniscus layer, allowing for the tapping mode. When the tip is brought sufficiently close to a sample, surface detection is based on the short-range atomic forces (Van der Waals) [79, 82].

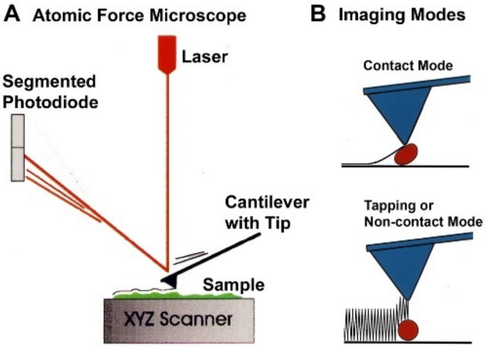

Figure 12. Illustration of the atomic force microscope (AFM) and the two most common AFM imaging modes (modified from [83]).

Surface morphology changes, primarily the evolution of the grain boundaries during ThO_2 dissolution, were measured using AFM (article II). Surface analyses were conducted as *ex situ* measurements performed using the Veeco Dimension 3100 microscope operated in the tapping mode and using high aspect ratio AFM tips.

4.4 Alpha spectrometry combined with chemical separation procedure^{III}

Alpha spectrometry is a common analytical technique for the detection and concentration analysis of alpha-active nuclides. Normally, analytes as measured isotopes are chemically separated from the sample matrix, and then a thin ‘massless’ sample is produced using electro-precipitation or co-precipitation. The ‘massless’ thin preparate is needed because otherwise the energy of alphas absorb in the medium itself. The space between the alpha source and detector is kept to a minimum and measurements are usually conducted in a vacuum because even the air molecules decrease the path length of the alpha particles.

Figure 13 shows the chemical separation procedure used in this work. In order to validate the results of the isotopic ratio analyses using SF-ICP-MS, unfiltered 7 ml samples were taken from the ^{229}Th tracer dissolution experiments. The procedure consists of separating thorium isotopes from the other radionuclides present (uranium and daughter nuclides of ^{232}Th, ^{228}Th and ^{238}U), co-precipitating thorium and filtrating the precipitate to produce a thin sample preparate for alpha measurement. Radiochemical procedures like this are frequently used in environmental studies [34; 84-85].

The separation procedure was needed because the standard solution for alpha measurements contained both ^{236}U and ^{229}Th and their daughter nuclides. In the first phase, thorium was flushed through a column with 9 M HCl, whereas the uranium (and Po) was retained in the anion exchange resin (Dowex 1x4 by Sigma Aldrich) as an $UO_2Cl_4^{2-}$ complex. The eluted fraction containing thorium was dried out on a hot plate and concentrated nitric acid was added to the residue to remove impurities from the sample. After dilution to HNO_3, thorium was retained in a Dowex 1 x 4 column as a $Th(NO_3)_6^{2-}$ complex, while the other nuclides were eluted from the column. Th^{4+} was removed from the column using HCl, evaporated to dryness and diluted to 1 M HCl again. Thorium was co-precipitated as ThF_4 with CeF_4 by adding 200 µl of a Ce carrier and concentrated HF. The precipitate kept overnight in a refrigerator was filtrated onto a 0.1 µm Millipore filter membrane. Dry filter membranes were glued to the sample holder prior to the alpha measurements.

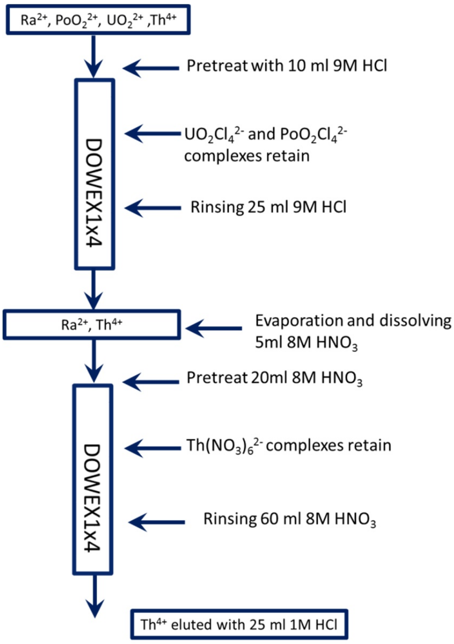

Figure 13. Radiochemical separation procedure used for thorium separation [article III].

The measurement of the alpha preparate was conducted in a vacuum with the Canberra 450 PIPS detector. Energy calibration was performed using the reference sample, which contained ^{244}Cm ($E_{\alpha1}$ = 5805 keV, I = 76.4%), ^{241}Am ($E_{\alpha1}$ = 5486 keV, I = 84.5%) and ^{237}Np ($E_{\alpha1}$ = 4788 keV, I = 47 %). The MAESTRO program for Windows Model A65-332 was used for data acquisition and analysis. The energy resolution for the four detectors used in the measurements ranged from 23 keV to 48 keV.

The ^{228}Th and ^{229}Th peaks were identified from the spectra and their pulses were integrated to calculate the activity of the isotopes in the sample. The activities of ^{229}Th were converted to moles allowing for the comparison of results from the concentrations as moles analysed using SF-ICP-MS.

4.5 Direct alpha spectrometry and advanced alpha-spectrometric simulations (AASI)^{IV}

After the dissolution experiments, the surface of ThO_2 pellets were analysed using alpha spectrometry accompanied by simulations to gain further information about the near-surface characteristics of the pellets. These pellets likely contained some precipitates on their surface after leaching for 534 days.

Normally, in alpha spectrometry, radiochemical separation methods are used to produce less than 100 nm thin samples creating clear and good-quality peaks in the measured alpha spectrum [86], as described above (see chapter 4.4). Thick samples make the analysis of radionuclides difficult, or even hinder it, since the alpha particles reach the detector from varying depths of the sample. This produces considerable peak widening, resulting in a step-like spectrum rather than a spectrum with narrow peaks.

Advanced alpha-spectrometric simulation (AASI) was developed by the Radiation and Nuclear Safety Authority of Finland to simulate the propagation of alpha particles in samples taken from the Earth's crust, air and detector materials [87]. Using nondestructive direct alpha measurement together with the AASI simulation program, the factors influencing the shape of the detected alpha spectrum can be examined. A few studies have already employed this method for either the analysis of Thule particles [86] or the analysis of air filters containing alpha-active particles [88-89].

AASI is based on the Monte Carlo methods and derives the spectrum from a large number of simulated initial decay incidents. It can be used for qualitative and quantitative analyses of alpha-active sources containing a comprehensive repertoire of isotopes. The geometry of the source medium and the distribution of the isotopes inside the medium can vary along with the properties of the detector and the distance between the source and the detector. In addition, the alpha emissions from different depths in the material layers can be calculated. When simulating, the nuclide content and physical properties of the source are varied until the isotope composition and possible precipitate layer thickness reproducing the measured source are found [86]. Thus, the individual isotopes underneath the surface can be examined in detail by studying the shape of the energy spectrum along the tail of the peaks [87].

Pellets A and B with a ^{229}Th tracer solution and pellets C and D without a tracer in the reference solution were analysed using direct alpha detection after 534 days of dissolution experiments. In addition, an intact ThO_2 pellet was analysed in order to compare it to leached pellets. Pellets 3.8 mm thick were measured using the same Canberra alpha-spectrometry system as described above (see chapter 4.4) at a distance of ~9 mm. The energy resolution of the detectors for the measurements varied between 23 and 48 keV (for samples A and B); unfortunately, higher resolutions were detected for samples C and D and for the intact sample. The geometric efficiency of the measurements reached about 0.19 ± 0.04 and the measurement time varied from 6 to 117 hours. Background spectra were measured for three to seven days, scaled to the measuring time of the sample spectrum and subtracted from the sample alpha spectra. The measured spectra were compared to the simulation values obtained using the AASI software program. The theoretical basis for these simulations is explained in further detail in article IV.

5. RESULTS AND DISCUSSION

5.1 Characteristics of sample pellets and fragments

5.1.1 ThO_2 pellets

The purity of the starting material, ThO_2 powder, for pellet fabrication was confirmed by XRD analysis. The characteristics necessary for a suitable UO_2 fuel analogue include a grain size on the order of 8 µm to 15 µm, a theoretical sintered density of >95.5% and randomly orientated grains. Figure 14 illustrates how the density of sintered pellets (defined as the percentage of the theoretical density, 10 g/cm^3) increases as the sintering temperature increases. The maximum density, 93% of the theoretical density, was achieved at a temperature of 1750°C. The final density of the ThO_2 pellets was slightly below the optimal density of the UO_2 fuel analogue. On the other hand, the density of SNF tends to decrease and porosity increase with fission gas bubble formation. The increasing density accompanying the increasing sintering temperature is consistent with the decreasing porosity and increasing grain size, as shown in the optical microscopic images of ThO_2 pellets in Figure 15. We found that the grain size increases from 2 µm to 10 µm at 1650°C and from to 10 µm to 30 µm at 1750°C. The grain size and crystallographic orientation of the optimal ThO_2 pellets were determined using EBSD analysis, which yielded an average grain size of 13 µm (based on the analysis of >10 000 grains). The results showed optimal grains randomly orientated in the ⟨111⟩, ⟨100⟩ and ⟨101⟩ crystal planes [article I]. The resulting grains ranged from 5 to 30 µm and were observed to be randonmly orientated, which is consistent with the microstructures of UO_2 and SIMFUEL [91-92]

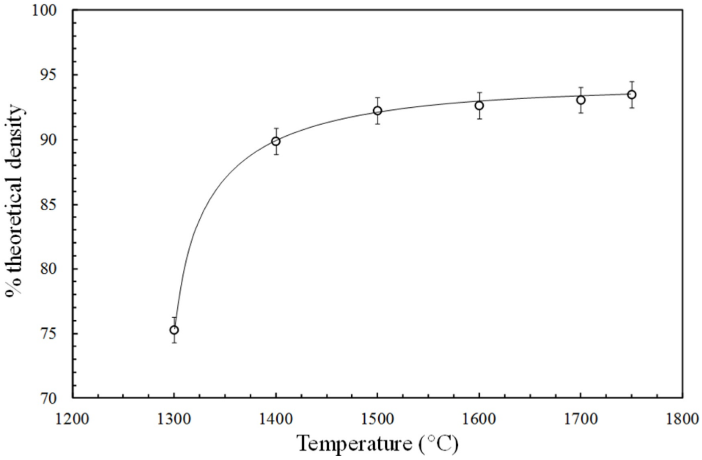

Figure 14. Density of sintered ThO_2 as a function of the sintering temperature [article I].

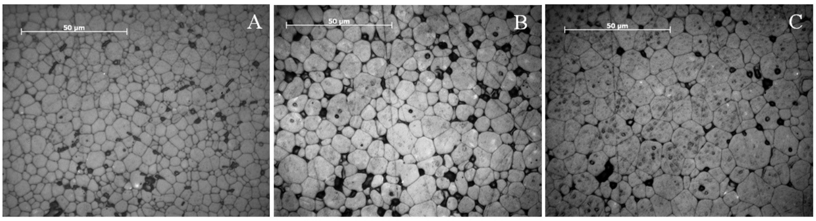

Figure 15. Optical microscope images of the ThO_2 pellet surfaces sintered at 1600 (A), 1700 (B) and 1750°C (C) [article I].

Figure 16 shows the profilometry image from the top of ThO_2 pellet A and from the surface of a vertical cross section of pellet B. In the image, the colour scale runs from blue to red. The bluish colours are below the median and can be considered ‘a valley’ while the reddish and yellow colours fall above the median. On the top surface, clear grain boundaries exist, yet no pores are observed, indicating a very low porosity. In the profilometry image of the cross section, however, pores are clearly visible and the grain boundaries are blurry. This indicates a higher porosity inside the pellet.

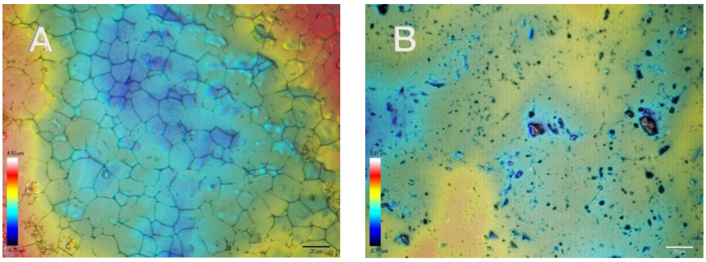

Figure 16. Confocal profilometer images of the outer surface of a pellet (A) and the cross section of the surface (B) of a ThO_2 pellet. The bluish colours lie below the median and can be considered ‘a valley’, while the reddish and yellow colours fall above the median [partly published in [93]].

5.1.2 ThO_2 fragments

Fragmentation of the ThO_2 pellets with SelFrag using the apparatus produced randomly shaped ThO_2 particles, as confirmed by optical (Figure 17) and electron microscopy (Figure 18). The particles produced using conventional comminution techniques (e.g. grinding) exhibit similar randomly broken grains, but have normally adhered fines on their surface. Due to the pulse fragmentation procedure, we could not observe adhered fines on those particles produced using the Selfrag apparatus. Adhered particle-free surfaces represent the ideal samples for the dissolution experiments undertaken in this study.

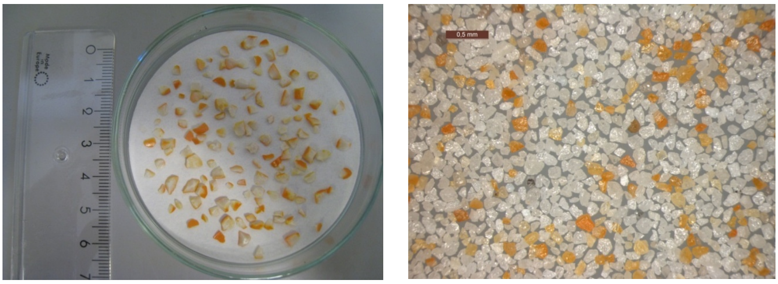

Figure 17. Photo of the 2 to 4 mm ThO_2 fragments (left) and optical microscopic image of 80 to 160 um particles produced from ThO_2 pellets for the dissolution experiments (right) [93].

The particles exhibited two main textures: those with a grain boundary texture and those without, as shown in Figure 18. The grain boundary texture of the surfaces of the original pellets was developed through high-temperature annealing. This boundary texture may also be possible on surfaces resulting from the pulse fragmentation process, which forces liquid through the grain boundaries breaking the particles apart and leaving behind several surfaces with grain boundary textures.

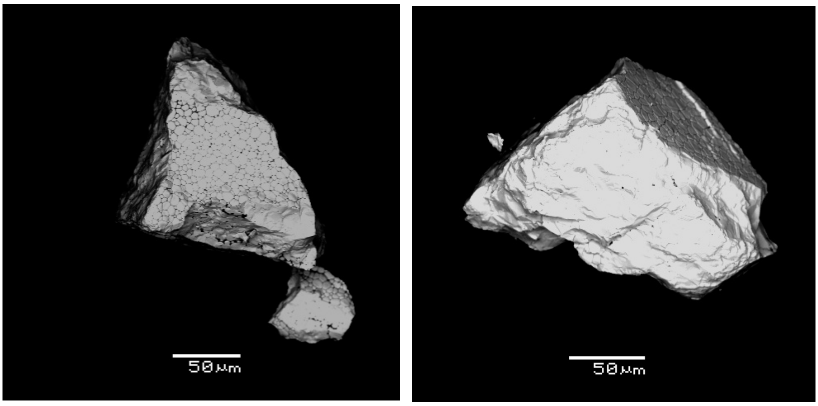

Figure 18. Backscattered electron (BSE) images of pulse-fragmented 80 to 160 µm particles [article I].

5.2 Results of the dissolution and solubility of ThO_2[I]

5.2.1 Pre-experiments under atmospheric conditions

The dissolution data for ThO_2 particles (2–4 mm) leached in 0.1 M NaCl or in 0.01 M NaCl with 2 mM $NaHCO_3$ are shown in Figure 19. In the solution with carbonate addition (Figure 19 B), a maximum thorium concentration of ~10^{-10} mol/L was achieved after 6 days of dissolution. The concentration in the ultrafiltered sample was only 3 x 10^{-13} mol/L after leaching for 6 days. In the ultrafiltered samples, the concentration increased steadily from 10^{-13} mol/L to 5 x 10^{-12} mol/L over 40 days, after which the Th concentrations levelled to between 10^{-11} and 10^{-12} mol/L in both non-filtered and ultrafiltered samples. The initial pH of 8.4 decreased slightly to pH 8.2 during the first 35 days of the experiment.

In a 0.1 M NaCl solution, the increase in the Th concentration was not obvious; the concentrations in both the non-filtered and ultrafiltered samples are scattered most likely due to the concentrations measured close to the analytical detection limit (1 × 10^{-13} mol/L) (see Figure 19 A). The Th concentration decreased below the detection limit in the ultrafiltered samples after 48 days. The initial pH of the 0.1 M NaCl increased from 5.4 to 5.8 during the first 35 days of the experiment. There is a clear difference in temporal behaviour of filtered and non-filtered samples in both solutions. This indicates fast Th release and formation of colloidal phases in the early stage, but later solubility inhibiting layer may be formed.

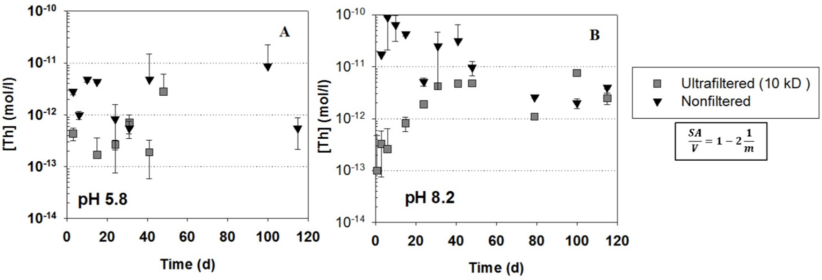

Figure 19. The evolution of the Th concentration in pre-experiments conducted in 0.1 M NaCl (A) and in 0.01 M NaCl with 2 mM $NaHCO_3$ (B).

Table 2 presents the initial dissolution rates calculated from the dissolution data for the two leaching solutions. The dissolution rate (r^{232}Th [mol g^{-1} s^{-1}]) for ThO_2 was calculated by using Equation (1)

$$r_{232Th} = \frac{V}{m}\frac{dc_{232Th}}{dt} \qquad (1)$$

,where V is the volume of the solution [L], m is the mass [g] of ThO_2 and dc/dt is the slope (linear fit) determined from the evolution of ^{232}Th release as function of time.

When comparing the results of the two experiments, the solubility and the dissolution rates were greater in the solution containing carbonate, likely due to the formation of Th-containing carbonate/hydroxide complexes. In the absence of carbonate, however, no clear trend emerged. If the dissolution rate is calculated from the ultrafiltered samples, the obtained value was an order of magnitude less than that in the carbonate-containing solution. Dissolved carbon dioxide from the atmosphere may have a slight solubility increasing effect in the experiments under atmospheric conditions in a 0.1 M NaCl solution.

Table 2. The initial dissolution rates [mol $g^{-1}s^{-1}$] calculated from the dissolution data of pre-experiments conducted on 2 to 4 mm particles in 0.1 M NaCl and 0.01 M NaCl with 2 mM $NaHCO_3$ solutions under atmospheric conditions.

Solution	**Filtration**	**pH**	**Rate [mol g^{-1} s^{-1}]**
0.1 M NaCl	non-filtered	6	6.1×10^{-19}
0.1 M NaCl	ultra-filtered	6	4.1×10^{-20}
0.01 M NaCl (2 mM $NaHCO_3$)	non-filtered	8	1.1×10^{-17}
0.01 M NaCl (2 mM $NaHCO_3$)	ultra-filtered	8	2.0×10^{-19}

To support the rate results, the effect of carbonate complexation on the solubility of thorium was evaluated in each of the applied experimental conditions by geochemical modelling (PHREEQC) shown in Figure 20. $Th(OH)_4$ and other hydroxide species prevail in 0.1 M NaCl, while in 0.01 M NaCl with 2 mM $NaHCO_3$ the carbonate and mixed carbonate–hydroxide complexes occur, thus increasing the solubility. The following sets of experiments were, therefore, conducted in an inert Ar atmosphere to exclude such effects.

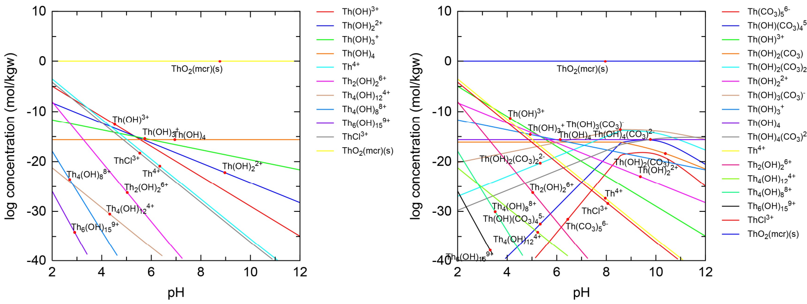

Figure 20. Thorium speciation in 0.1 M NaCl and 0.01 M NaCl (2mM $NaHCO_3$). Modelled using PHREEQC applying Andra's database Thermochimie7b [93].

5.2.2 ThO_2 dissolution in anaerobic conditions

The dissolution data resulting from the leaching of 2 to 4 mm particles of ThO_2 in 0.1 M NaCl in an Ar atmosphere are shown in Figures 21 (a–d). Unfiltered samples resulting from the smaller size fraction (80 to 160 µm) demonstrated a relatively rapid initial increase in the Th concentration to ~8 × 10^{-10} mol/L after 2 days of dissolution, followed by a progressive decrease to 4 × 10^{-11} mol/L during 89 days (Figure 21a). Under the same conditions, ultrafiltered samples (Figure 21b) yielded a maximum Th concentration of ~4 × 10^{-10} mol/L after 7 days of leaching. After 9 days of dissolution, the concentration of Th decreased to below 1 × 10^{-11} mol/L and remained at ~2 × 10^{-12} mol/L after 57 days.

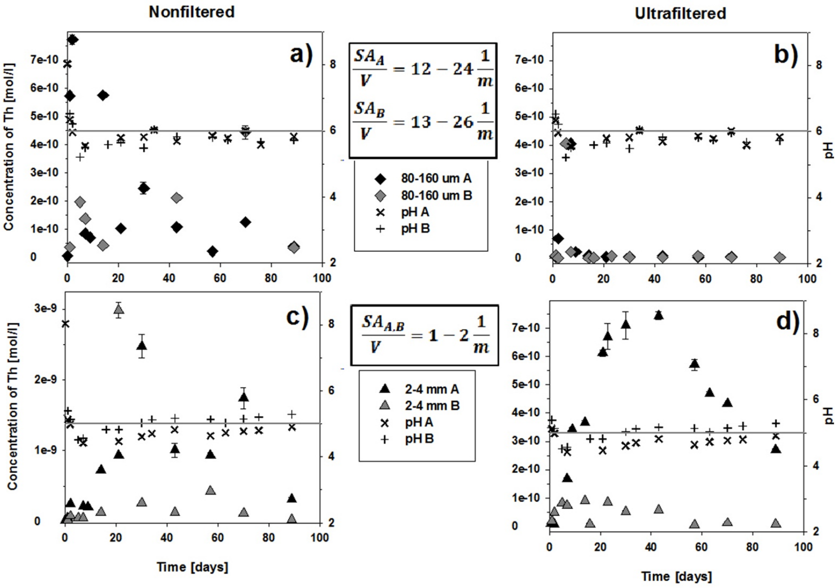

Figure 21. The evolution of the Th concentration and pH in 0.1 M NaCl using 80 to 160 µm particles (a, b) and 2 to 4 mm fragments (c, d). The figures on the left (a, c) show the results from the non-filtered samples while those on the right (b, d) show the results for ultrafiltered samples.

In the experiments on fragments with a fraction of 2 to 4 mm, maximum Th concentrations of 3 × 10^{-9} mol/L and 7.4 × 10^{-10} mol/L were reached after 23 days for non-filtered and ultrafiltered samples, respectively (Figures 21c and 21d). This suggests that the dissolution and precipitation–sorption kinetics are slower in these samples compared to those with a smaller particle size and larger surface area. In the experiments using 2 to 4 mm fragments, less surface area was available for the sorption and precipitation of secondary Th compounds, so the saturation limit is reached slowly. In parallel experiments, the ultrafiltered concentration (Figure 20d) showed an almost one order of magnitude variation, at 7 × 10^{-12} mol/L in experiment A and 3 × 10^{-10} mol/L in experiment B. This may be due to the influence of the pH ranging from 4.8 to 5.3 in the test solutions. While the pH differences were quite small, these findings suggest that the solubility of ThO_2 is highly dependent on the H^+ activity in the solution (see Figure 4 chapter 2.4 above). The initial pH in the 2 to 4 mm ThO_2 dissolution experiments decreased rapidly from pH 8 to between 5 and 6, where it remained for the duration of the experiment. This unexpected result is likely due to the leaching of H^+ from incompletely rinsed reaction vessels.

To further investigate the influence of the particle size on the dissolution of ThO_2, experiments were conducted in 0.01 M HNO_3 solutions, the detailed results for which appear in article I. In nitric acid, the dissolved Th concentrations far exceeded the analytical detection limit of Th by SF-ICP-MS. Compared to the experiments in the 0.1 M NaCl solution, the Th concentrations were approximately two orders of magnitude higher with clear trends seen over time. However, a difference of one order of magnitude was observed between parallel tests using 2 to 4 mm fragments. This might result from the significant differences between the surface morphology of the parallel fragments. The morphology and the heterogeneity of fragments may vary depending upon from which part of the ThO_2 pellet they originate, as illustrated in Figure 16 (see chapter 5.1.1).

The initial dissolution rates of ThO_2 were calculated from the evolution of the Th concentrations during the release period of Th into the solution, which took between 5 to 30 days depending on the liquid phase in question. The variables used in the linear regression model and the calculated rates appear in Table 3.

Table 3. The initial dissolution rates [mol $g^{-1}s^{-1}$] calculated for parallel experiments A and B or E and F (Rate 1 for A or E, Rate 2 for B or F) conducted under anaerobic conditions at room temperature.

Solution	Particle size	Filtration	pH	Rate 1 [mol g^{-1} s^{-1}]	Rate 2 [mol g^{-1} s^{-1}]
0.1 M NaCl	80-160 µm	non-filtered	5-6	1.7×10^{-15}	5.6×10^{-16}
0.1 M NaCl	80-160 µm	ultra-filtered	5-6	2.1×10^{-16}	1.1×10^{-16}
0.1 M NaCl	2-4 mm	non-filtered	4-5	1.5×10^{-16}	2.3×10^{-17}
0.1 M NaCl	2-4 mm	ultra-filtered	4-5	1.0×10^{-16}	2.1×10^{-17}
0.01 M HNO_3	80-160 µm	non-filtered	2	1.3×10^{-13}	3.5×10^{-14}
0.01 M HNO_3	80-160 µm	ultra-filtered	2	2.7×10^{-14}	2.2×10^{-14}
0.01 M HNO_3	2-4 mm	non-filtered	2	2.4×10^{-14}	1.7×10^{-14}
0.01 M HNO_3	2-4 mm	ultra-filtered	2	2.3×10^{-14}	1.7×10^{-14}

The calculated dissolution rates depend most on pH, supporting previous findings from ThO_2 solubility data (see Figure 4 in chapter 2.4). The highest rates were achieved under acidic conditions, while the rates decreased under neutral and basic conditions. Furthermore, the presence of carbonate slightly increased the dissolution rate. A smaller particle size owing to the bigger surface area also increased the initial dissolution rate. Small differences were also observed between parallel experiments (A and B or E and F; Rate 1 vs. Rate 2) and in the comparison between rates calculated from non-filtered and ultrafiltered samples.

5.2.3 **The solubility of ThO_2**

Figure 21 presents the solubility levels at the end of the dissolution experiments, which were compared to the equilibrium data of ThO_2 and $Th(OH)_4$ taken from the ThermoChimie database [NEA/TDB]. It should be noted that in some experiments the Th concentration did not achieve a clearly constant level, but rather decreased at the end of 90 days. For example, in the experiment on 2 to 4 mm fragments in 0.1 M NaCl in Ar, the solubility level did not stabilise to a steady-state during the experiments. In addition, the experiments with 2 to 4mm fragments in 0.01 M HNO_3 showed decreasing trend at the point of 90 days and the system might not have been in equilibrium state.

As can be seen, the solubilities measured at pH 2 were at a lower level than would be expected from the thermodynamics. Yet, the solubility at pH ranging from 4 to 8 fell between the theoretical solubilities of crystalline ThO_2 and amorphous $Th(OH)_4$ (see Figure 22). Solubilities below the theoretical solubility of ThO_2 (cr) have also been observed in other undersaturated dissolution experiments conducted in acidic conditions [14, 42]. Neck et al.'s experiments [42] also showed that the value of the solubility product was dependent upon the crystallite size. At a higher pH range, the data here reached lower levels compared to the values presented by Neck et al. [42] and Vandenborre et al. [14]. These values may result from the higher crystallinity or due to the relatively high sintering temperature of the ThO_2 utilised in this study. Previously, Rand et al.[94] have reported the solubility decreasing effect of ThO_2(cr) as a function of increasing crystallite size. Even thought the experiments were conducted in undersaturated conditions, in most cases the maximum concentration was achieved during the early stages of the experiments, after which the thorium concentration began to level out indicating that a secondary precipitation occurred.

SF-ICP-MS enabled an extremely accurate analysis of the dissolved Th concentrations. The detection limit was 10^{-12} mol/L, which is about two decades lower than that achieved using conventional quadrupole ICP-MS such as that used in previous Th solubility studies [19, 21, 61, 95-97].

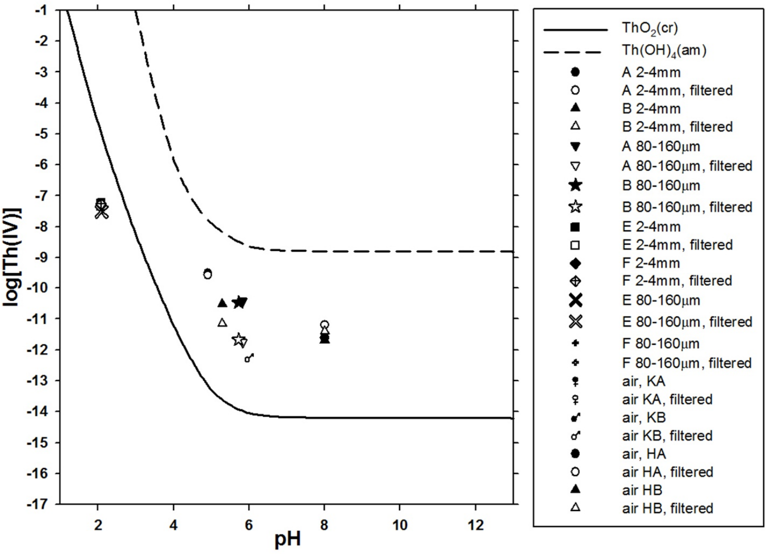

Figure 22. The solubility levels of thorium after approximately 100 days investigated in this work using crystalline ThO_2. The thermochemical equilibrium data for ThO_2 and $Th(OH)_4$ [NEA/TDB] are shown as solid and dashed lines, respectively. Letters A and B refer to parallel experiments conducted in 0.1 M NaCl, whereas parallel experiments E and F were conducted in 0.01 M HNO_3. KA refers to 0.1 M NaCl, with pH 6 and HA to 0.01 M NaCl (2 mm $NaHCO_3$) with pH 8 [article I].

5.3 Results of the surface investigations$^{I\ \&\ II}$

5.3.1 SEM imaging of leached ThO_2 surfaces^{I}

The SEM images of acid-leached ThO_2 particles revealed that the particle leaching behaviour can differ enormously (see Figure 23). Some particles (Figure 23A) did not differ from fresh and unreacted particles (cf. Figure 18, chapter 5.1.2). However, for a single particle, some surfaces showed grain rounding and widening along the grain boundaries indicating grain boundary dissolution (Figure 23B), while other surfaces appeared to host a ‘blanket’ of secondary phases precipitated from the solution. In addition, some particles showed characteristics of either a higher initial porosity, a more vigorous dissolution or both (Figure 23C).

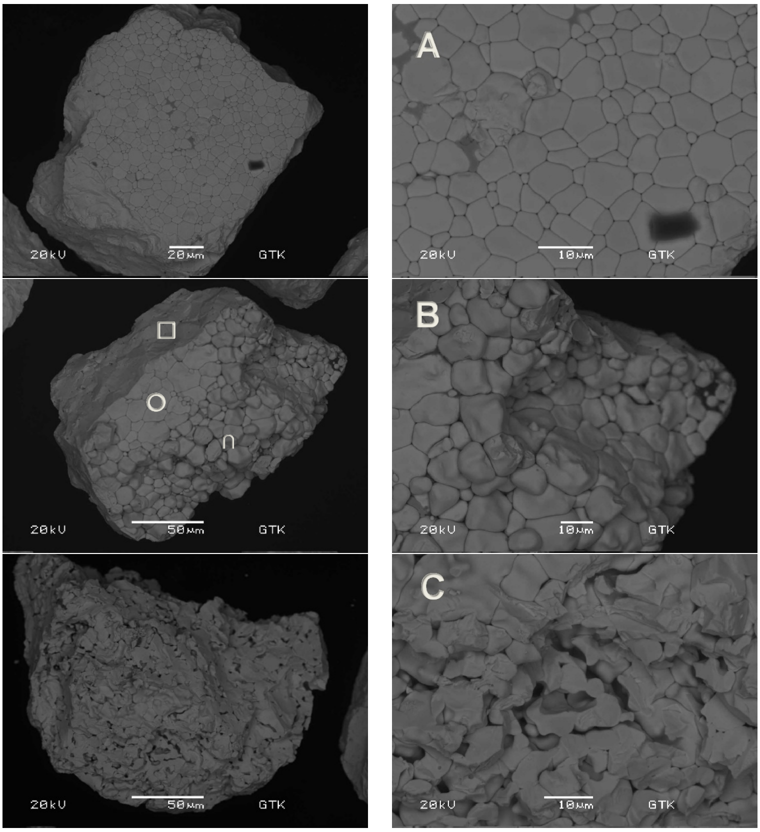

Figure 23. BSE images of 80 to 160 µm particles leached in 1 M HNO_3 at 80 °C for 4 weeks. A leached particle resembling a fresh one (A). One particle (B) first showing areas of clear dissolution (∩), second no reaction with grain boundaries (○) and third an area with no grain boundaries (□) indicating precipitation on that surface. The last particle (C) showed deeper dissolution, which had deformed grain boundaries and some cavities were formed.

These dissolution differences may result from the different particle morphologies originating from the different parts of the intact pellets. As described above (see chapter 5.1.1), the structure of the original pellets was not homogenous. This most likely results from the upper particle with clear grain boundaries originating from the pellet surface which features a more stable grain structure compared to other particles. The last particle (C) may feature a more porous structure, as we see in the cross section of the original ThO_2 pellet (see Figure 16, chapter 5.1.1).

5.3.2 Integrated imaging with VSI, AFM and SEM-EBSD[II]

The thorium concentration dissolved from annealed ThO_2 pellets at 90°C in nitric acid showed a similar behaviour to previous experiments (article I). The concentration increased rapidly during the initial days of the experiment, decreasing to a constant level after ten days of dissolution (see Figure 1c in article II). The initial dissolution rate of the annealed ThO_2 samples was $5.23 \pm 0.1 \times 10^{-7}$ ($g\,m^{-2}\,d^{-1}$) ($\approx 3 \times 10^{-15}$ $mol\,g^{-1}\,s^{-1}$) at 90°C, which is approximately one order of magnitude slower than the rates for particles and fragments in 0.01 M HNO_3 at room temperature (Table 3). Despite the higher temperature, the decreased rate is most probably observed due to more stable surfaces of annealed pellet with less defect sites in comparison to surfaces of crushed particles. Similar observations were done for CeO_2 surfaces in article II.

Figure 24 shows the selected grains of CeO_2 and their AFM profiles measured as a function of leaching time. The grain surfaces are measured against the inert reference surface at a constant height. In article II, the AFM or SEM-EBSD images of the ThO_2 surfaces were not presented; these appear here in Figure 25. In addition, Table 4 lists the grain orientations, grain boundary misorientations and the depths from the integrated imaging approach. The evolution of the surface and depth of the grain boundaries using different misorentation angles preceded AFM as a function of time.

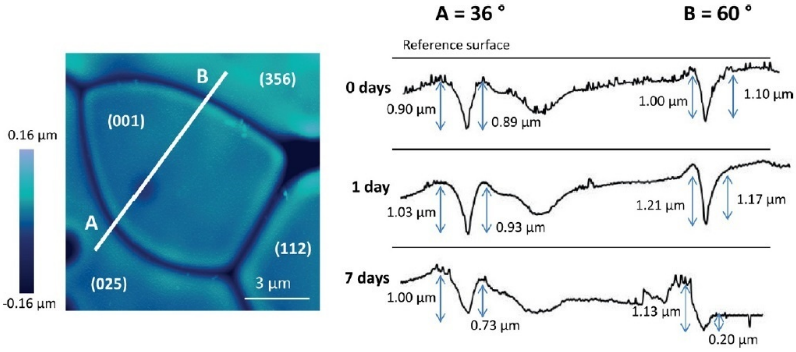

Figure 24. Atomic force microscopy (AFM) image and cross sections of CeO_2 grains with the grain boundaries of low (A) and high (B) misorientation angles. The grain surfaces are measured against the inert reference surface at a constant height. The cross sections show the change in the depth of the grain boundaries and grain surfaces with time during dissolution at 90°C in 0.01 M HNO_3. [article II]

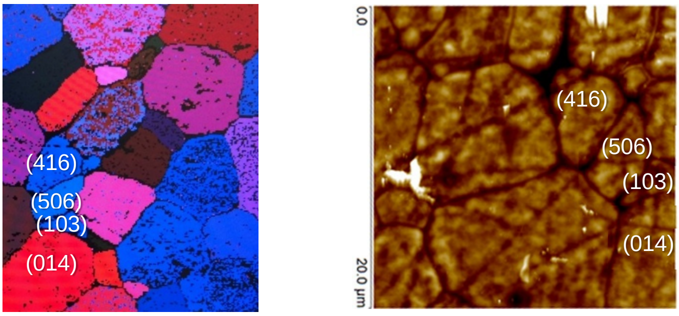

Figure 25. Electron backscattering diffraction (EBD) and atomic force microscopy (AFM) image of a monitored ThO_2 surface area and grains with their crystallographic orientations.

At the beginning of the experiment between, 0 and 1 days, it was observed that the retreat rates of the CeO_2 grain boundaries were greater than the surface retreat rates. In both CeO_2 and ThO_2, the retreat rate of the different grain boundaries was greatest for the high misorientation angle boundaries compared to the low misorientation angle grain boundaries. The retreat rate of the highest ThO_2 misorientation angle (56°) was more than twice that of the misorientation angle of 23.91°. These observations indicate a strong crystallographic control over dissolution and that an instant release takes place at the grain boundaries. After seven days of dissolution, measuring the grain boundaries was no longer possible in ThO_2 due to the appearance of a surface layer. This agrees with the dissolution data, showing a decrease in the thorium concentration after an initial release. The disappearance of the grain boundaries was observed for some ThO_2 particles using SEM imaging (Figure 23B) indicating the formation of a surface layer after the initial release. Previously, Rai et al. [98] demonstrated that the amorphous ThO_2(am) phases were converted to crystalline ThO_2(cr) upon heating at 90°C in an acidic solution. Therefore, recrystallized ThO_2 may form some kind of layer on the surface. The formation of relatively stable secondary phases might explain the observed dissolution behaviour of ThO_2.

Table 4. Grain boundary depths of CeO_2 and ThO_2 grains at different grain orientations and grain boundary misorientation angles (presented in Figures 24 and 25) as a function of time during dissolution at 90°C in 0.01 M HNO_3 [article II].

			grain boundary depth (µm)			
analogue composition	grain orientations	grain boundary misorientation angle (deg) (±0.01)	0 days (±0.01)	1 day (±0.01)	7 days (±0.01)	grain boundary retreat rate (µm d−1) (±0.001)
CeO_2	(025)/(001)	36.01	0.9	1.03	1.00	0.014
	(001)/(356)	59.84	1.01	1.21	1.13	0.017
ThO_2	(103)/(506)	23.91	0.04	0.05	0.09	0.007
	(103)/(014)	39.33	0.04	0.14	0.15	0.012
	(416)/(506)	56.05	0.07	0.12	0.17	0.015

5.4 Results from dissolution experiments with a ^{229}Th tracer^{III}

5.4.1 Solution results with SF-ICP-MS

In all experiments, ^{232}Th was released relatively rapidly from $^{232}ThO_2$ during the initial days of the experiment, as illustrated in Figure 26. The dissolution experiments with a ^{229}Th tracer (A, B, E and F) approached equilibrium from oversaturation, whereas those experiments without a tracer (C, D, G and H) began from undersaturation. A fast initial release occurred despite the excess ^{229}Th in the aqueous phase. The results indicate that the initial dissolution is particularly driven by the surface stability of the dissolving $^{232}ThO_2$ surfaces and grain boundaries rather than by chemical equilibrium. These observations are in agreement with previous findings from the broader study (articles I and II).

The concentrations of ^{229}Th clearly decreased during the initial 20 days, most likely due to the precipitation and adsorption of the Th hydroxide species on the vessel and the ThO_2 surfaces. In most of the tracer experiments, the ^{229}Th and ^{232}Th concentrations converge and fall to between 10^{-11} and 10^{-10} mol/l within 60 days (see Figure 26). Yet, none of those concentrations achieved a constant level, since a slight decrease was still observed at 104 days. The ^{232}Th concentrations in the undersaturation experiments (C, D, G and H) showed quite similar trends, although exhibiting slightly lower ^{232}Th concentrations than their reference experiments (A, B, E and F) with a ^{229}Th tracer.

The results of parallel experiments all agreed with one another except for the one order of magnitude difference in the thorium concentrations between ThO_2 pellets A and B. In addition, the difference in the dissolution and precipitation behaviours was observed in the release calculations of ^{232}Th using the isotopic dilution method. This method showed that pellet A dissolved up to day 40, whereas the experiment B reaction becomes a net precipitation after 20 days (see Figure 5 in article III). This raises a question regarding which factors cause such a difference. The initial near-neutral pH increased to up to about 9 over 104 days, and the pH difference between parallel samples was 0.8 to 0.5 pH units. However, under basic conditions the pH should not significantly affect the solubility (see Figure 4, chapter 2.4). Another possible explanation may lie in the pellet surfaces, whereby the grain sizes and grain boundaries were non-identical and dissolution differed due to the pellet surface energies (see Figure 23).

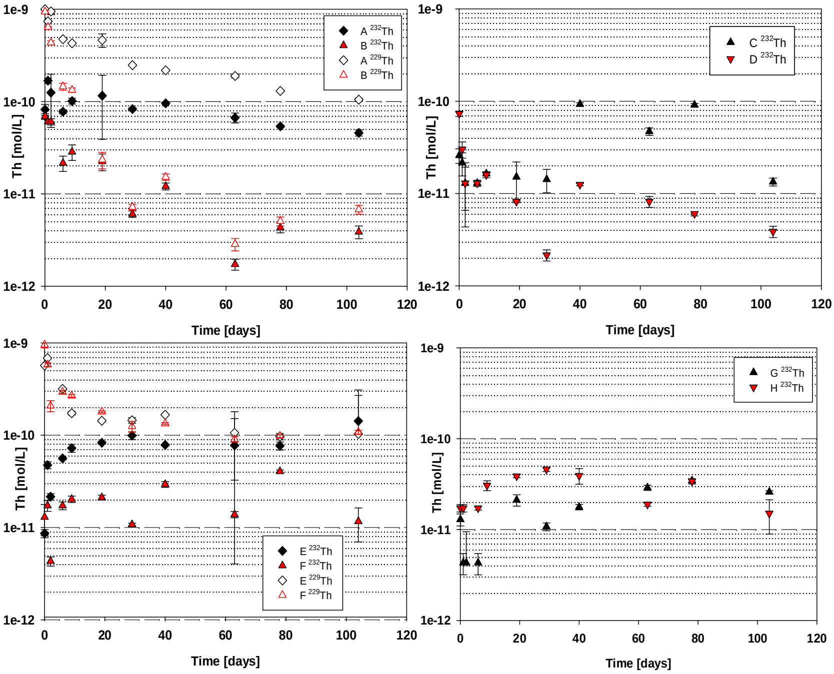

Figure 26. Evolution of thorium concentrations (using SF-ICP-MS) in the dissolution experiments conducted with pellet (A–D) and fragment (E–H) samples. Experiments A, B, E and F contained 10^{-9} mol/L of a ^{229}Th tracer in the aqueous phase at the initial stage of the experiments [article III].

When comparing the results from non-filtered and ultrafiltered samples after 534 days of dissolution, the concentrations in the ultrafiltered samples were close to or below the detection limit of 10^{-12} mol/L, whereas the concentration in non-filtered samples increased. This increase was significant for the experiments between 104 and 534 days, particularly among the fragmented samples (E, F, G and H) (see the table in Figure 26). This indicates that most of the thorium in an aqueous solution was present in the colloidal form. Thorium has a strong tendency to form polynuclear species and colloids under slightly basic conditions [24-25, 34]. The elevated ^{232}Th concentrations indicate the increase of colloidal phases in a solution as dissolution proceeds from 104 to 534 days. The amount of adsorbed or precipitated thorium along the reaction vessel walls was estimated by leaching the vessels with 1 M HNO_3.The polynuclear and colloidal species strongly tend towards adsorption onto surfaces, which was also observed from the results of the vessel leachates (Figure 27). The concentration of ^{232}Th in the vessel leachates was one to two orders of magnitude higher than the concentration in the aqueous phase after 534 days of dissolution, indicating that a significant amount of dissolved thorium was sorbed or precipitated to the vessel surfaces.

The thorium hydroxides and oxyhydroxides precipitated or adsorbed onto the pellet surface most likely resulting in the slight difference in the ^{232}Th concentrations observed between the dissolution experiments with and without a ^{229}Th tracer. Due to the excess ^{229}Th, it probably precipitates or adsorbs during the early stage of the oversaturation experiment. Yet, in the undersaturation experiments lacking ^{229}Th in the aqueous phase, the sorption sites are fulfilled from the fraction of ^{232}Th, which is first dissolved from the solid phase.

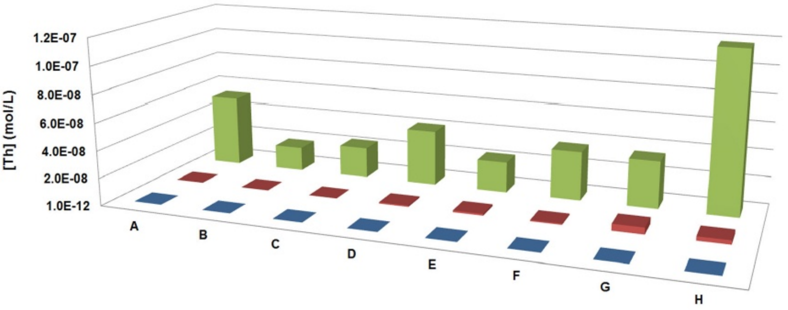

	A	A error	B	B error	C	C error	D	D error
🟦 Solution (104 d)	$4.57\cdot10^{-11}$	$0.34\cdot10^{-11}$	$0.39\cdot10^{-11}$	$0.06\cdot10^{-11}$	$1.34\cdot10^{-11}$	$0.13\cdot10^{-11}$	$0.39\cdot10^{-11}$	$0.01\cdot10^{-11}$
🟥 Solution (534d)	$2.21\cdot10^{-11}$	$0.02\cdot10^{-11}$	$6.91\cdot10^{-11}$	$0.05\cdot10^{-11}$	$3.51\cdot10^{-11}$	$0.03\cdot10^{-11}$	$93.85\cdot10^{-11}$	$4.44\cdot10^{-11}$
🟩 Vessel leachates	$5.25\cdot10^{-08}$	$0.07\cdot10^{-08}$	$1.78\cdot10^{-08}$	$0.02\cdot10^{-08}$	$2.29\cdot10^{-08}$	$0.04\cdot10^{-08}$	$4.08\cdot10^{-08}$	$0.10\cdot10^{-08}$

	E	E error	F	F error	G	G error	H	H error
🟦 Solution (104 d)	$14.22\cdot10^{-11}$	$16.68\cdot10^{-11}$	$1.16\cdot10^{-11}$	$0.47\cdot10^{-11}$	$2.59\cdot10^{-11}$	$0.06\cdot10^{-11}$	$1.51\cdot10^{-11}$	$0.04\cdot10^{-11}$
🟥 Solution (534d)	$128.55\cdot10^{-11}$	$1.45\cdot10^{-11}$	$85.45\cdot10^{-11}$	$1.26\cdot10^{-11}$	$488.25\cdot10^{-11}$	$471.26\cdot10^{-11}$	$295.48\cdot10^{-11}$	$2.98\cdot10^{-11}$
🟩 Vessel leachates	$2.27\cdot10^{-08}$	$0.02\cdot10^{-08}$	$3.59\cdot10^{-08}$	$0.03\cdot10^{-08}$	$3.46\cdot10^{-08}$	$0.03\cdot10^{-08}$	$11.73\cdot10^{-08}$	$0.24\cdot10^{-08}$

Figure 27. ^{232}Th results from 104- and 534-day dissolution experiments in 0.01 M NaCl and from the reaction vessel leachates (1 M HNO_3) measured using SF-ICP-MS.

The isotopic ratios were analysed to calculate the total dissolution of thorium by using the isotope dilution method [99], which takes into account the precipitation and sorption out from solution. This method provides the total amount of thorium released into a solution from the solid phase from the measured ^{229}Th/^{232}Th ratio and the concentration of ^{232}Th in a solution. The calculations are described in further detail in article III.

The ^{229}Th/^{232}Th ratios decreased in all tracer experiments (A, B, E and F), as illustrated in Figure 27. The ratio decreased significantly already during the first day, which agrees with the initial fast release of ^{232}Th from the solid phase (see Figure 26). Over 104 days, the isotopic ratio approached 1 and clearly decreased to below 1 after 500 days. The isotopic ratios continuously decrease as expected. This suggests that the dissolution and precipitation reactions also continue in the equilibrium state.These observations support the theoretical hypothesis that the, solid-solution equilibrium is dynamic as the chemical equilibrium in dissolution process involves the two way transfer of material from and to the ThO_2 surface. In nature, reactions like these can lead to the isotopic fractionation of lighter elements like Mg, O or Ca [100-101]. The precipitating mineral phase may favor the lighter isotope as their mass difference is relatively high (~8 %). However, in the case of ^{229}Th tracer experiments the mass difference between ^{229}Th and ^{232}Th is only 1.3 % and there is a huge excess of ^{232}Th isotope. In pellet experiment, the molar ratio $^{229}Th/^{232}Th$ in the system is 6.6×10^{-9}.

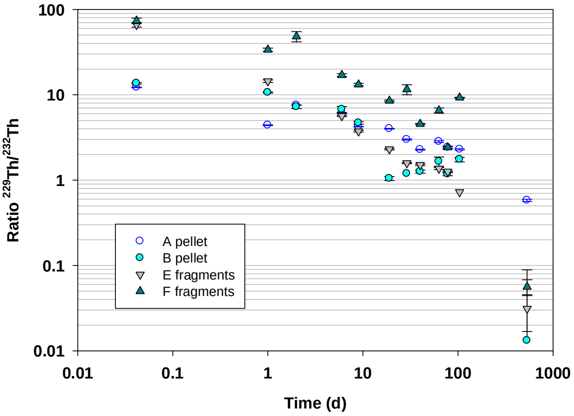

Figure 28. Evolution of the $^{229}Th/^{232}Th$ ratios analysed using SF-ICP-MS in the dissolution experiments conducted using a ^{229}Th tracer (A, B, E and F) over 534 days.

For comparison, isotopic ratios were measured from the vessel-out leachates (see Table 5). The results illustrate that in most cases the amount of ^{229}Th is higher along the vessel walls than in the solution. However, the ratios are remarkably lower after 534 days than the ratios measured in the aqueous phase at the beginning of the experiment. This suggests that dissolution and precipitation reactions occur not only on the solid surface of ThO_2, but also along the vessel walls. In most cases (B, E and F), the ratio in the aqueous phase is substantially lower during the solution phase than along the vessel walls, indicating that the surface sites were primarily occupied by ^{229}Th, but equilibrated with the aqueous phase over time.

Table 5. $^{229}Th/^{232}Th$ ratios (by SF-ICP-MS) in the dissolution experiments conducted with a tracer (A, B, E and F) in a solution and along the vessel walls (in vessel leachates) after 534 days.

Sample type	**A**	**B**	**E**	**F**
Solution 534 d	0.580	0.013	0.031	0.056
Vessel leachate 534 d	0.336	0.515	1.095	0.983

The complete release of ^{232}Th was calculated using the isotopic method from the measured ^{232}Th concentrations and isotopic ^{229}Th/^{232}Th ratios. The release data for thorium were plotted as a function of time. Table 6 displays the resulting rates. The linear regression models were fitted using the calculated data points from 0 to 10 days to evaluate the initial release and dissolution rates. The data for experiments A and E showed a linear nature over 104 days. Thus, for those experiments, the second rates appearing after 20-day dissolution were also calculated. The amount of released ^{232}Th and the dissolution rates are higher using the isotopic method than when measuring only the concentration of ^{232}Th in the solution. As we see here, the second rates are slightly lower than the initial rates. In addition, the second rates are probably closer to the long-term dissolution rates when most of the high-energy surface sites are already dissolved.

Table 6. The initial dissolution rates (10 days) of ThO_2 using the isotopic dilution method and the values used in the calculations (dc/dt, masses for the solids and volumes for the solutions; 2nd refers to the secondary rate after 20 days).

Tracer experiment	dc/dt (mol l^{-1} day^{-1})	Mass of solid (g)	Volume of solution (L)	Rate (mol g^{-1} s^{-1})
A	1.55E−11	1.97	0.05	4.6E−18
A (2nd)	8.94E−12	1.97	0.05	2.6E−18
B	1.35E−11	1.94	0.05	4.0E−18
E	2.54E−11	0.54	0.05	2.7E−17
E (2nd)	3.22E−12	0.54	0.05	3.5E−18
F	6.78E−12	0.54	0.05	7.3E−18

The difference between the fragmented and pellet rates appears quite small. The fragmented samples yielded slightly higher rates in comparison to the ThO_2 pellets. When compared to the rates for the ThO_2 fragments calculated previously using a normal dissolution method, the rates here (pH ~8) fall between 10^{-19} mol g^{-1}s^{-1} determined under aerobic conditions (pH 6) and 10^{-17}-10^{-16} mol g^{-1}s^{-1} determined under anaerobic conditions (pH 5).

5.4.2 **Dissolution results by ICP-MS compared with alpha spectrometry**

The results from the ICP-MS analyses were compared with those from the radiochemical technique, a method that uses chemical separation and alpha spectrometry. The 534-day samples with a ^{229}Th tracer were separated, precipitated and measured using alpha spectrometry. The peaks of the tracer ^{229}Th and ^{228}Th, a daughter nuclide of ^{232}Th, were clearly detected in the spectrum, whereas ^{232}Th ($t_{1/2} = 1.4 \times 10^{10}$) appears as a very small peak. The ^{229}Th activities integrated from the measured peaks were converted to concentrations.

The concentrations of ^{229}Th determined through alpha spectrometry and SF-ICP-MS appear in Table 7. The two methods yielded comparable results. The biggest difference was found for pellet sample B, which has the lowest concentration, causing more uncertainty in the results for both the alpha and ICP measurements. In this sample, the concentration of ^{229}Th analysed using ICP-MS was four times lower than that measured using alpha spectrometry.

Table 7. ^{229}Th concentrations measured using alpha spectroscopy and SF-ICP-MS in 534 day samples. Concentrations were determined from ^{232}Th and the isotopic ratio of ^{229}Th/^{232}Th.

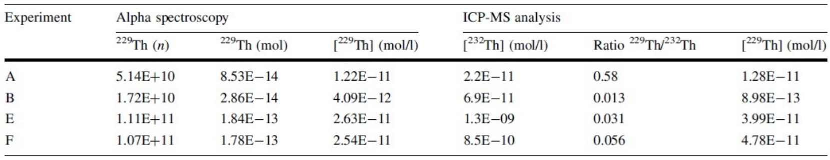

Experiment	Alpha spectroscopy			ICP-MS analysis		
	^{229}Th (n)	^{229}Th (mol)	[^{229}Th] (mol/l)	[^{232}Th] (mol/l)	Ratio ^{229}Th/^{232}Th	[^{229}Th] (mol/l)
A	5.14E+10	8.53E−14	1.22E−11	2.2E−11	0.58	1.28E−11
B	1.72E+10	2.86E−14	4.09E−12	6.9E−11	0.013	8.98E−13
E	1.11E+11	1.84E−13	2.63E−11	1.3E−09	0.031	3.99E−11
F	1.07E+11	1.78E−13	2.54E−11	8.5E−10	0.056	4.78E−11

The detection limit of ^{232}Th (and ^{229Th}) in the ICP-MS analyses varied from 1 x 10^{-12}mol/l to 4 x 10^{-12}mol/l depending on the daily efficiency of the instrument. The detection limit of ^{232}Th in alpha spectrometry was 7.6 x 10^{-11} mol/l (0.0007 Bq/l) calculated using the Currie method [102]. This is more than a decade higher than the detection limit achieved by SF-ICP-MS, preferred given its sensitivity as a technique for ^{232}Th. By contrast, the detection limit of ^{229}Th was 1.34 x 10^{-16} mol/l (0.00024 Bq/l), significantly better than that for SF-ICP-MS.

The detection limit of ^{232}Th via the activity measurement is higher than that for ^{229}Th due to its longer half-life ($t_{1/2}$(^{232}Th) = 14 x 10^9 years) compared to $t_{1/2}$(^{229}Th) = 7340 years) and thus its lower specific activity. In alpha spectroscopy, we must take into account that the separation procedure is time-consuming and tedious, and the benefit of the lower detection limit is not easily achieved.

5.5 Direct alpha measurement of pellets and advanced simulations^{VI}

The intact ThO_2 pellet (sample E) and the leached pellet (sample C) were measured using alpha spectrometry. Their measured and background-subtracted spectra are shown in Figure 29. The spectrum of the intact pellet shows only the step-like characteristics of the mother nuclide ^{232}Th and its daughters ending at ^{212}Po with the highest energy. The spectrum of the leached pellet, however, clearly shows detectable peaks diverging from the step-like spectrum. The peaks of the daughter nuclides (^{228}Th, ^{224}Ra, ^{220}Rn, ^{216}Po and ^{212}Po) indicate increasing amounts of daughter nuclides at the surface of the leached pellet in comparison to the intact pellet. The relatively high solubilities of Ra and Rn (gas) in comparison to the nearly insoluble Th probably increase the amount of Ra, Rn and following daughters in the solution phase from which they are co-precipitated by forming thorium hydroxides after the fast initial release of thorium. In addition, the high concentration of ^{228}Th is notable, which is possibly due to the alpha recoil process where the daughter nuclides reside in the damaged crystallographic sites within the pellet, from where they may more readily mobilise [103].

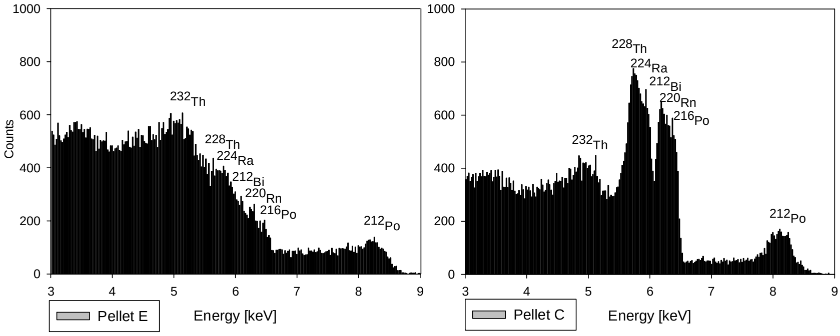

Figure 29. The measured spectra of the intact ThO_2 pellet E and ThO_2 pellet C leached in 0.01 M NaCl for 534 days.

The alpha energies of the ^{232}Th and ^{229}Th series daughter nuclides were used to interpret the peaks and steps in the measured spectra (Figures 29 and 30). The observed counts and the frequency of decay incidents in the spectrum depend on the nuclides half-lives—the shorter the half-life, the higher the observed counts at the energy of the alpha daughter for similar numbers of decaying atoms. The simulated spectrum of the intact ThO_2 pellet is shown in Figure 30. This simulation appears as a rough step-like spectrum with no clear peaks, continuing as steps for the daughters through the last unstable alpha-active isotope ^{212}Po with an extremely short half-life. Because the energy calibration of pellets E and C shifted slightly during the analysis, the fit of the simulations to the measured spectra proved challenging. This can be seen as a difference for ^{212}Po steps in Figure 30.

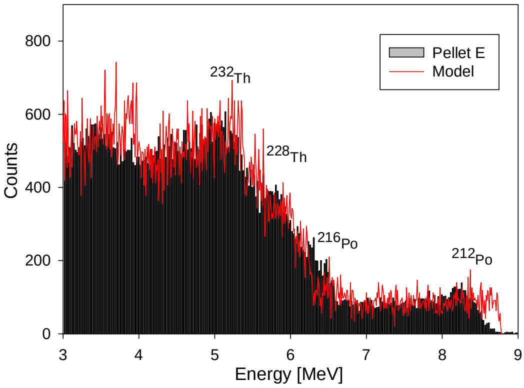

Figure 30. Simulated spectrum of the intact $^{232}ThO_2$ sample (pellet E, red) accompanied by the histogram of the measured spectrum (black).

After the reference pellets (C and E) were measured, pellet A—leached in a ^{229}Th tracer–labelled solution—was also measured using alpha spectrometry. The spectrum was simulated as shown in Figure 31. The measured spectrum has relatively narrow alpha peaks for ^{229}Th and the daughter nuclides of the ^{232}Th and ^{229}Th decay series. No clear peak for ^{232}Th is seen, indicating that the primary component of the pellet spreads homogeneously throughout the medium. Yet, the distinct peaks for the ^{232}Th and ^{229}Th alpha daughters suggest the presence of differing amounts of those isotopes in a thin layer above the pellet compared to the bulk $^{232}ThO_2$. Below the peak spectrum a clear step-like structure for both decay chains of ^{232}Th and ^{229}Th is observed (article IV). In addition, the step-like spectrum of ^{229}Th and its daughters suggests that they penetrate into the $^{232}ThO_2$ bulk pellet beneath the surface layer. These findings were examined with subsequent AASI simulations.

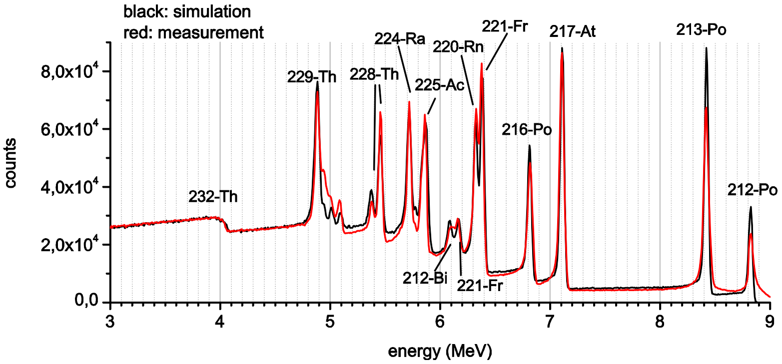

Figure 31. Measured (red) and simulated (black) spectra of $^{232}ThO_2$ pellet A using a concentrated layer of ^{229}Th and daughter nuclides (of both decay series) on top of the pellet.

For AASI simulations, the dimensions of the pellets and their measurement positions were needed to calculate the geometric efficiency. In addition, the density of the pellet was used to run the simulations. Separate simulations were run for the relative concentrations in the bulk medium and the various thicknesses of the surface layers. By using both the bulk and surface layer, we allowed a better fit for the simulations. The spectrum was simulated iteratively until a qualitative match was obtained.

The thin layer was simulated at a maximum thickness of 0.1 µm. A thinner medium did not yield a better fit to the measurements because of the limited energy resolution of the detector. The surface layer quite likely contains mostly ^{232}Th, although a clear alpha peak for ^{232}Th remains unseen because of its homogenous nature to bulk $^{232}ThO_2$ beneath the surface.

The direct alpha measurement and simulations of the ThO_2 pellet were in good agreement with the results of the dissolution experiments, in which the drop in [Th](aq) after fast initial dissolution indicates adsorption or precipitation (articles I, II and III). The layer formation was also observed by AFM after 7 days leaching of pellet in 0.01 M HNO_3 at 90 °C (article II). The chemical form of the surface layer in both cases is unknown. Most probably some amorphous

$ThO_x(OH)_y \cdot H_20$ first adsorbs from the solution onto the pellet surface, but later they may transform towards ThO_2(cr) with time. Previously, Neck and Kim (2001) have suggested that in their experiments the surface of ThO_2 (cr) was covered by amorphous $Th(OH)_4$ layer, which serves as solubility limiting phase. Rai et al. [98] have shown that these amorphous phases are capable to recrystallization. In their experiments the ThO_2(am) was converted to crystalline ThO_2(cr) upon heating at 90°C in acidic solution. Under near neutral conditions the layer appears most probably mainly as amorphous $ThO_x(OH)_y \cdot H_20$. However, it is more pronounced that solid transformations are slow under near neutral or basic conditions at 25°C [94]. In those conditions, the surface layer remains longer in amorphous $ThO_x(OH)_y \cdot H_20$ form, but may show significant decrease in Th solubility due to ageing affect, which is more probable in higher $[Th]_{aq}$.

In addition, the alpha spectrometry provided interesting information on the behaviour of the daughter nuclides, present at such low concentrations that many other methods cannot reach such low detection limits. Similar to leached pellet C, the relatively high solubilities of Ra and Rn likely lead to increased amounts of Ra, Rn and the resulting daughters in the solution phase [35]. After the relatively fast initial dissolution of thorium, the daughter nuclides can be co-precipitated or adsorbed as thorium begins to form low solubility hydroxides.

The fact that ^{229}Th and all its daughter nuclides, initially present in solution, showed step like characteristics in the alpha spectrum indicates that the route or mechanism for intrusion would be same for all nuclides. The results from article II show that the grain boundaries play a significant role during the initial release and dissolve relatively quickly to more stable grains. In the same article, the results for CeO_2 suggested that the dissolution occurs preferentially along the grain boundaries and that the boundaries may act as conduits for solution ingress during dissolution. Vandenborre et al. [14] determined that 80% of the surface of sintered ThO_2 featured less reactive crystalline thorium oxide grains. The remaining 20% was largely composed of grain boundaries and corresponded to the more reactive $ThO_{(x)}(OH)_{(y)}(H_2O)_{(z)}$. They suggested that the latter is involved in solid–solution exchange mechanisms. Thus, the grain boundaries are the most probable route for ^{229}Th and its daughter nuclides to intrude below the <0.1 µm surface layer, deeper into the bulk of $^{232}ThO_2$ pellet. The prevailing secular equilibrium of ^{229}Th and its daughters does also support this hypothesis. The formation of solid solution in the ThO_2 matrix cannot be excluded totally.

6. CONCLUSIONS

The effort to produce ThO_2 pellets with similar microstructures to the UO_2 in fuel matrix was successful. The grain size was close to 10 to 20 microns and the grains showed a random crystallographic orientation. However, microscopic studies showed that the pellet microstructure remains heterogeneous and thus might introduce some variation in the leaching behaviour. The heterogeneity of the original pellets—that is, the difference in the porosity and grain size of ThO_2—likely significantly affects experiments conducted using a few 2 to 4 mm fragments, possibly originating from the different locations of the original pellet.

A faster initial dissolution was observed in the experiments with particles 80 to 160 µm in size. Subsequent adsorption and/or precipitation was also relatively fast, most likely due to the higher surface area, which controls both dissolution and precipitation. In comparison, a slower release rate was found in the experiments with fragments 2 to 4 mm, yet the resulting maximum Th concentration was higher. This could indicate that release of Th took place along high-energy surface sites such as the grain boundaries, more common among fragments 2 to 4 mm in size than in smaller particles. However, in these fragments, a smaller surface area exists than in smaller particles and less of the released Th could be adsorbed or precipitated.

In the experiments, the effect of the carbonate complexation was observed, but we found that the magnitude of dissolution in these experiments was primarily dependent on pH. The dissolution rates of thorium in pellets and fragments fell within the range of 10^{-16} mol $g^{-1}s^{-1}$ and 10^{-19} mol $g^{-1}s^{-1}$ in NaCl solutions and between 10^{-13} mol $g^{-1}s^{-1}$ and 10^{-15} mol $g^{-1}s^{-1}$ in HNO_3 solutions. The dissolution rates decreased over time in the leaching experiments. The rates after the fast initial release days are likely closer to the long-term dissolution rates when most of the high-energy surface sites are already dissolved and the adsorption or precipitation already block some of the sites. The amount of released ^{232}Th and the dissolution rates are higher when using the isotopic method than when measuring only the concentration of ^{232}Th in the solution by SF-ICP-MS.

The dissolution process appears to be controlled not only by the chemical equilibrium but also by the surface stability of the dissolving sample surfaces. The fast release most likely occurs due to ‘high-energy surface site’ dissolution. These sites consist of grain boundaries and crystallographic defects which play a significant role in early-stage dissolution. The original characteristics of the material, such as the grain size and grain boundary features, and heterogeneous morphology, have most likely affect the dissolution behaviour. The crystallization state, sample preparation and pre-leaching have also an effect on dissolution behaviour. Thus, the high sintering temperature of the fabricated ThO_2 pellets used in this investigation compared with previous studies might have caused slightly lower solubility values.

The release of thorium from the ThO_2 surface leads to the saturation of the solution with respect to it forming amorphous $ThO_x(OH)_y·H_2O$ or even polynuclear $Th_x(OH)_y$ species. These amorphous phases are capable of recrystallizing, especially under elevated temperatures and acidic conditions. Under higher pH (≥ 4) layer consist most probably $ThO_x(OH)_y·H_2O$ (am) with low solubility. Amorphous layer can evolve slowly via solid state transformation to less soluble phases while ageing. This kind of layer can serve as solubility limiting phase, providing a barrier to further dissolution and leading to the formation of surfaces that precipitate rather than dissolve. In this study, the formation of a layer onto the ThO_2 pellet slows thorium dissolution as observed using AFM. The results of the leaching experiments showed that the different particles in the same experiment yield quite variable dissolution and precipitation processes occurring simultaneously, most likely due to the different local surface energies of different particles and grains.

The ^{229}Th tracer experiments showed that the dissolution process involves the two way transfer of material from and to the ThO_2 surface taking place at a very early stage in the experiments. Adsorption and/or precipitation leads to the formation of a ^{229}Th-rich layer at the top of the $^{232}ThO_2$ pellet. This observation was supported by the direct alpha measurements accompanied with AASI, which together showed that the layer did not exceed a thickness of 0.1 µm. By the end of the ^{229}Th tracer experiments, the solution leached from the vessel walls revealed that a significant amount of ^{232}Th adsorbed or precipitated along those vessel walls. The isotopic ratio measurement revealed a ratio closer to that measured in the solution at the end of the experiment than that at the beginning, indicating that precipitation on the vessel wall surface together with the precipitation on the pellet surface accompany adjustments to the solubility equilibrium.

All experiments conducted at $pH > 2$ showed temporal variation between the non-filtered and ultra filtered solution concentrations of Th, indicating that colloids play a role in these conditions. In the long-term experiments, a remarkable increase in the concentration of Th in a solution after between 104 and 534 days of leaching was observed, suggesting an increase in the colloidal phases in a solution as dissolution of the solid phase proceeds. These polynuclear and colloidal species also have a high tendency towards sorption on the surfaces, agreeing with various previous observations. Yet, we must ask, what really happens between 100 and 534 days? Is the capacity of the surface to adsorb the formed thorium hydrous phases fulfilled? Further sampling points and techniques more sophisticated than those employed here would allow us to study the chemistry of the surfaces and to identify the thorium species such as colloids.

One goal of this study aimed to validate the method developed to analyse the ^{229}Th/^{232}Th isotopic ratio using the SF-ICP-MS technique. Towards this aim, the other method employed here relied on alpha spectrometry. These two methods yielded comparable results for ^{229}Th concentrations. The congruent results appear to validate the thorium concentration measurements by SF-ICP-MS. The direct alpha measurement yielded interesting insight into the dissolution and co-precipitation behaviour of the alpha daughter nuclides of the ^{229}Th and ^{232}Th decay series. The concentrated layer of ^{229}Th also contained concentrated amounts of the daughters of the ^{232}Th decay series, suggesting that they were released from the bulk before they co-precipitated onto the surface layer. In general, the daughter nuclides are located at the grain boundaries and defect sites, and can, therefore, more easily mobilised. The solubilities of Ra and Rn are also known to exceed the solubilities of thorium, leading to a higher release of them and the following daughter nuclides. By contrast, the presence of ^{229}Th and its daughters was also observed in the bulk beneath the surface layer. The grain boundaries and pores appear to be the primary paths into the bulk pellet matrix, although the formation of a solid solution cannot be completely discounted.

This study has brighten the understanding of dissolution behavior sparingly soluble ThO_2. It has also been an example case of 4+ actinide release mimicking the dissolution of UO_2 under strict reducing conditions and with no localized oxidation, in deep geological repository.

REFERENCES

1. Alexander, W. R., McKinley, L. E. (ed.): Deep Geological Disposal of Radioactive Waste, Elsevier Series Radioactivity in the Environment, Vol. 9 (2008).

2. Combie, C., Pescatore, C., Smith, P., van Luik, A.: Geological Disposal of Radioactive Waste, Review of Developments in the Last Decade, OECD Publications, 2, rue André-Pascal, 75775 PARIS CEDEX 16, France (66 1999 17 1 P) ISBN 92-64-17194-0 –No. 51101 (1999).

3. Fuel and Canister Process Report for the Safety Assessment SRSite. SKB Tech. Rep. (2010) TR-10-46.

4. Smellie, J., Karlson, F. A Reappraisal of some Cigar Lake Issues of Importance to Performance Assessment. SKB Tech. Rep. (1996) TR 96-08.

5. Gauthier-Lafaye, F., Holliger, P., Blanc, P. L. Natural Fission Reactors in the Franceville Basin, Gabon: A Review of the Conditions and Results of a “Critical Event” in a Geologic System. Geochim. Cosmochim. Acta 60 (1996) 4831−4852.

6. Knauss, P., Wolery, T. J. Dependence of Albite Dissolution Kinetics on pH and Time at 25 °C and 70 °C. Geochim. Cosmochim. Acta 1986, 50, 2481−2497.

7. White, A. F., Bullen, T. D., Schulz, M. S., Blum, A. E., Huntington, T. G., Peters, N. E. Differential Rates of Feldspar Weathering in Granitic Regoliths. Geochim. Cosmochim. Acta 65 (2001) 847−867.

8. White, A. F., Brantley, S. L. The Effect of Time on the Weathering of Silicate Minerals: Why do Weathering Rates Differ in the Laboratory and Field? Chem. Geol. 202 (2003) 479−506.

9. Zhu, C., Veblen, D. R., Blum, A. E., Chipera, S. J. Naturally Weathered Feldspar Surfaces in the Navajo Sandstone Aquifer, Black Mesa, Arizona: Electron Microscopic Characterisation. Geochim. Cosmochim. Acta 70 (2006) 4600−4616.

10. Ollila, K., Oversby, V. M. Dissolution of Unirradiated UO_2 and UO_2 Doped with ^{233}U Under Reducing Conditions. SKB Tech. Rep. (2005) TR-05-07.

11. Ollila, K. Dissolution of Unirradiated UO_2 and UO_2 Doped with ^{233}U in 0.01 M NaCl Under Anoxic and Reducing Conditions. Posiva Oy Rep. 2006, 2006−08.

12. Zetterström Evins, L., Juhola, P., Vähänen M., REDUPP Final Report, Posiva Working (2014) Report 2014-12

13. Vandenborre J., Abdelouas A., Grambow B., Discrepancies in Thorium Oxide Solubility Values: a new experimental approach to improve understanding of oxide surface solid/solution. RadioChim. Acta. 96 (2008) 515-520.

14. Vandenborre J., Grambow B., Abdelouas A. Discrepancies in Thorium Oxide Solubility Values: Study of Attachment/Detachment Processes at the Solid/Solution Interface. Inorg. Chem. 49 No. 19 (2010) 8736-8748.

15. Neck, V., Kim, J. I.: Solubility and hydrolysis of tetravalent actinides. Radiochim. Acta 89, 1 (2001)

16. Bundschuh, T., Knopp, R., Müller, R., Kim, J., Neck, V., Fanghänel, T.: Application of LIBD to the determination of thesolubility product of thorium(IV)-colloids. Radiochim. Acta 88 ,No. 9-11/2000, (2000). 625

17. Rothe, J., Denecke,M., Neck, V., Müller, R., Kim, J.: XAFS investigation of the structure of aqueous thorium(IV) species, colloids, and solid thorium(IV) oxide/hydroxide. Inorganic Chemistry 41, 2 (2002).. 249–258

18. Bitea, C., Müller, R., Neck, V., Walther, C., Kim, J.: Study of the generation and stability of thorium(IV) colloids by LIBD combinedwith ultrafiltration. Colloids and Surfaces A: Physicochemical and Engineering Aspects 217,1 (2003). 63–70

19. Altmaier, M., Neck, V., Fanghänel, T.: Solubility and colloid formation of Th(IV) in concentrated NaCl and MgCl2 solution Radiochimica Acta 92 (2004) 537–543

20. Walther, C., Fuss, M., Buchner, S.: Formation and hydrolysis of polynuclear Th(IV) complexes- a nano-electrospray massspectrometry study. Radiochim. Acta 96, (2008) 411–426

21. Hubert, S., Barthelet, K., Fourest, B., Lagarde, G., Dacheux, N., Baglan, N.: Influence of the precursor and the calcination temperature on the dissolution of thorium dioxide. Journal of Nuclear Materials 297, 2 (2001) 206–213.

22. Dekoussar V., Dyck G.R., Galperin A., Ganguly C., Todosow M., Yamawaki M., Thorium fuel cycle – Potential benefits and challenges. IAEA, IAEA-TECDOC-1450, Vienna, (2005)

23. IAEA TECDOC-1654, Advanced Fuel Pellet Materials and Fuel Rod Design for Water Cooled Reactors (2010)

)24. Morss, L. R., Edelstein, N. M., Fuger, J., Katz, J. J., 2006. The Chemistry of the Actinide and Transactinide Elements, Springer

25. Wickleder, M., Fourest, B., Dorhout, P., Chapter 3, Thorium, in The Chemistry of the Actinide and Transactinide Elements, 3rd edition. Springer, 2006. ISBN 1402035985.

26. Henriksen, P., ed., 2007. "Morten Thrane Esmark". Store norske leksikon (in Norwegian). Oslo: Kunnskapsforlaget. Retrieved 16 May 2009.

27. Berzelius, J. J.,1829. Untersuchung eines neues Minerals und einer darin erhalten zuvor unbekannten Erde (Investigation of a new mineral and of a previously unknown earth contained therein), Annalen der Physik und Chemie. 16 (7): 385–415. Bibcode:1829 AnP....92..385B. doi:10.1002/andp.18290920702. (modern citation: Annalen der Physik, 92, no. 7 (1829) 385–415)

28. Berzelius, J. J., 1829. Undersökning af ett nytt mineral (Thorit), som innehåller en förut obekant jord (Investigation of a new mineral (thorite), as contained in a previously unknown earth), Kungliga Svenska Vetenskaps Akademiens Handlingar (Transactions of the Royal Swedish Science Academy): 1–30.

29. Schilling, J. 1902. Die eigentlichen Thorit-Mineralien (Thorit und Orangit), Zeitschrift für Angewandte Chemie. 15 (37): 921–929. doi:10.1002/ange.19020153703.

30. Weeks, M. E. 1932. The discovery of the elements. XI. Some elements isolated with the aid of potassium and sodium: Zirconium, titanium, cerium, and thorium". Journal of Chemical Education. 9 (7): 1231. Bibcode: 1932JChEd...9.1231W. doi:10.1021/ed009p1231.

31. Curie, M.1898. Rayons émis par les composés de l'uranium et du thorium (Rays emitted by compounds of uranium and thorium), Comptes Rendus (in French). 126: 1101–1103. OL 24166254M.

32. Schmidt, G. C.. Über die vom Thorium und den Thoriumverbindungen ausgehende Strahlung (On the radiation emitted by thorium and thorium compounds), Verhandlungen der Physikalischen Gesellschaft zu Berlin (Proceedings of the Physical Society in Berlin) (in German). 17 (1898)14–16.

33. Schmidt, G. C. Über die von den Thorverbindungen und einigen anderen Substanzen ausgehende Strahlung (On the radiation emitted by thorium compounds and some other substances). Annalen der Physik und Chemie (in German). 65: 141–151. (modern citation: Annalen der Physik, 301(1898) 141–151).

34. Lehto, J., Hou, X., Chemistry and analysis of radionuclides: laboratory techniques and methodology. (2011) Wiley-VCH, Hoboken,

35. Nelson A.W., Eitrheim E.S., Knight A.W, May D., Mehrhoff M.A., Shannon R., Litman R, Burnett W.C, Forbes T.Z., Schultz M.K., Understanding the Radioactive Ingrowth and Decay Of Naturally Occuring Radioactive Materials in Environment: An Analysis of Produced Fluids from the Marcellus Shale; Environmental Health Perscepctives. 123, 7 (2015) 689-696.

36. Council Regulation (EC) No 428/2009 of 5 May 2009 setting up a Community regime for the control of exports, transfer, brokering and transit of dual-use items (Recast)

37. Comission Regulation (Euratom) No 302/2005 of 8 February 2005 on the application of Euratom safeguards

38. Treaty on the Non-proliferation of Nuclear Weapons, 1970. www.iaea.org/sites/default/files/publications/documents/infcircs/1970/infcirc140.pdf

39. Rai, D., Felmy, A.R., Moore, D.A., Mason, M.J., The solubility of Th solubility of Th(IV) and U(IV) hydrous oxides in concentrated $NaHCO_3$ and Na_2CO_3 solutions. In: Scientific Basis for Nuclear Waste Management XVIII, Part 2, T. Murakami and, R. C. Ewing (eds.),pp. 1143–1150, Materials Research Society Symposium Proceedings, Volume 353, Materials Research Society, Pittsburgh, Pennsylvania (1995).

40. Östhols, E., Bruno, J., Grenthe, I.: Ötshols, E., Bruno, J., Grenthe, I.: The solubility of microcrystalline ThO_2 in CO-H_2O media. Geochim. Cosmochim. Acta. 58, 2 (1994) 613–623

41. Kim, S., Baik, M., Choi, J., Shin, H., Yun, J.: The dissolution of ThO_2(cr) in carbonate solutions and a granitic groundwater.Journal of Radioanalytical and Nuclear Chemistry 286, 1 (2010).91–97.

42. Neck, V., Altmaier, M., Müller, R., Bauer, A., Fanghänel, Th. Kim, J. I. 2003. Solubility if crystalline thorium dioxide. Radiochim. Acta 91 (2003) 253–262

43. Moon, H.C., Equilibrium ultrafiltration of hydrolyzed thorium (IV) solutions. Bulletin of the Korean Chemical Society, 10 (1989) 270-272.

44. Fuger J., Rand M., Grenthe I., Neck V., Rai D., 2007. Chemical Thermodynamics of Thorium, OECD Nuclear Energy Agency. (2007)

45. Neck V., Müller R., Bouby M., Altmaier M., Rothe J., Denecke M.A, Kim J.I., Solubility of amorphous Th(IV) hydroxide – application of LIBD to determine the solubility product and EXAFS for aqueous speciation. Radiochim. Acta, 90 (2002) 485 –494.

46. Felmy, A. R., Rai, D., Sterner, S. M., Mason, M. J., Hess, N. J., and Conradson, S. D. J. Solution. Chem., Thermodynamic Models for Highly Charged Aqueous Species: Solubility of Th(IV) Hydrous Oxide in Concentrated $NaHCO_3$ and Na_2CO_3 Solutions, 26 (1997) 233–48.47

48. Neck, V. and Kim, J. I. An electrostatic approach for the prediction of actinide complexation constants with inorganic ligands-application to carbonate complexes, Radiochim. Acta, 88 (2000) 815–22.

49. Rai, D., Swanson, J. L., Ryan, J. L.: Solubility of $NpO_2 \cdot xH_2O$(s) in the presence of Cu(I)/Cu(II) redox buffer. Radiochim. Acta 42 (1987) 35

50. V. Neck, J. Kim, Solubility and hydrolysis of tetravalent actinides. Radiochim. Acta. 89 (2001) 1-16.

51. Lasaga A., Blum A. Surface Chemistry, etch pits and mineral- water resctions, Geochim and cosmichim. Acta 50 (1986) 2533-2550

52. Syner R and Doherty M., Faceted crystals shape evolution during dissolution or growth, AIChE J., 53 (2007)1337-1348

53. Mutter A. The bond Valence deficiency model, University of Münster, Doctoral dissertation, 2007

54. Pastina and Hellä, 2006, Models and Data Report (2010) POSIVA-raportti 2010-1: ISBN: 978-951-652-172-8

55. Patrik Sellin and Olivier X. Leupin, The Use of Clay as an Engineered Barrier in Radioactive-Waste Management –·Review, Clays and Clay Minerals, Vol. 61, No. 6, (2013) 477–498

56. Stennett M. C., Corkhill C.L, Marshall L. A., Hyatt N.C., 2013. Preparation, Characterisation and Dissolution of a CeO_2 Analogue for UO_2 Nuclear Fuel, J. Nucl. Mater, 432 (2013) 182–188.

57. Claparende L., Clavier N., Dacheux N., Moisy P., Podor R., Ravaux J., 2011. Influence of crystallization state and micro-structure on the chemical durability of Cerium-Neodynium mixed oxides, Inorg. Chem. 50 (2011) 9059-9072.

58. Edmonson P.D., Zhang, Y, Moll S., Navamar F., Weber W.J, 2012. Irradiadiation effects of microstructure change in nano-crystalline ceria – Phase, lattice stress, grain size and grain boundaries, Acta Materialia 60 (2012) 5408-5416

59. https://commons.wikimedia.org/w/index.php?curid=1012751

60. Rodney C. Ewing, Nature Materials 14, 252–257 (2015) Long-term storage of spent nuclear fuel

61. Heisbourg G., Hubert S., Dacheux N., Purans J., 2004. Kinetic and thermodynamic studies of the dissolution of thoria-urania solid solutions. Journal of Nuclear Materials. 335 (2004) 5-13.

62. Akie H.T., Muromura T., Takano H., Matsuura S., 1994. A New Fuel Material for Once-Through Weapons Plutonium Burning, Nucl. Techol., 107 (1994) 182-192.

63. Fourest B., Vincent T., Lagarde G., Hubert S., Baudoin P., 2000. Long-term behaviour of a thorium-based fuel, J. Nucl. Mater. 282 (2000)

64. Fourest B., Hubert S., Lagarde G., Vincent T., (2000) Thorium as a waste management option: residual risk of final disposal, project report nuclear Science and technology, edited by Gruppelaar H., Schapira J.P., EUR19142

65. Forsyth, R., Fuel rod D07/B15 from Ringhals 2 PWR: Source material for corrosion/leach tests in groundwater. Fuel rod/pellet characterisation program part 1. (1987) SKB technical report 87-02

66. Forsyth, R., Spent nuclear fuel. A review of properties of possible relevance to corrosion processes. (1995) SKB technical report 95-23

67. Andres, U., Timoshkin, I., Jirestig, J. Liberation of minerals by high-voltage electrical pulses. Powder Technology 104 (1999) 37–49,

68. Bluhm, H., Frey, W., Giese, H., Hoppe, P., Schultheiß, C.,Straßner, R. Application of Pulsed HV Discharges to Material Fragmentation and Recycling. IEEE Trans. On Dielectrics and Electrical Insulation 7, No. 5 (2000).

69. Papin, P.; Chen, C.-F.; Forsyth, R.; Luther, E.; Necker, C., Surface Preparation for Characterising Microstructure on Transuranic Oxides by Electron Backscatter Spectroscopy and Ion Beam Imaging, Microsc. Microanal, 18 (2012) 708

70. Hou X., Roos P., 2008. Review article, Critical comparison of radiometric and mass spectrometric methods for the determination of radionuclides in environmental, biological and nuclear waste samples, Analytica Chimica Acta 6 0 8 (2008) 105–139

71. Holmes L., Determination of thorium by ICP-MS and ICP-OES 2001. Radiat Prot Dosim 97(2) (2001) 117–122

72. Hou X.D., Chen W., He Y.H., Jones B.T., 2005. Analytical Atomic Spectrometry for Nuclear Forensics, Appl. Spectrosc. Rev. 40 (2005) 245–267.

73. Jarvis, K.E., Gray A.L., Houk, R.S., Handbook of Inductively Coupled Plasma Mass Spectrometry (1992) Blackie & Son Ltd. Galsgow and London 1992KUBA

74. Shen C-C, Edwards L.R., Cheng H., Dorale J.A., Thomas R.B., Moran S.B., Weinstein S.E., Edmonds H.N., Uranium and thorium isotopic and concentration measurements by magnetic sector field coupled plasma mass spectrometry. Chem Geol 185 (2002)165–178

75. http://houk.public.iastate.edu/instruments/elementicpms.html

76. Pröfrock D., Prange A., Inductively coupled plasma-mass spectrometry (icp-ms) quantitative analysis in environmental and life sciences: a review of challenges, solutions, and trends. Appl Spectrosc 66(8) (2012) 843–868

77. Mehta R., Chapter 2 in Scanning Electron Microscopy; Interactions, Imaging and Spectra in SEM, University of Central Arkansas, USA, published by Intech (open access)

78. Sampson A.R., Scanning Electron Microscopy 1996

79. José Ricardo Assunção Godinho, A surface approach to understanding the dissolution of fluorite type materials Implications for mineral dissolution kinetic models Stockholm, April 2013, Dissertation for the degree of Doctor of Philosophy in Science Godinho J. R. A. Department of Geological Sciences Stockholm University

80. Wright S.I., Nowell M. M., de Kloe R., Camus P , Rampton T., Electron imaging with an EBSD detector, Ultramicroscopy 148 (2015) 132–145

81. Humphreys F.J. Review grain and sub grain characterization by electron backscatter diffraction, Journal of Materials Science; 36 (2001) 3833-3854

82. Egerton, R.F., Physical Principles of Electron Microscopy, An Introduction to TEM, SEM, and AEM

83. http://web.physics.ucsb.edu/~hhansma/biomolecules.htm

84. Rozmaric M, Ivsic AG, Grahek Z Determination of uranium and thorium in complex samples using chromatographic separation ICP-Ms and spectrophotometric detection. Talanta 80 (2009) 352–362

85. Kiliari T, Pashalidis I., Thorium determination in aqueous solutions after separation by ion-exchange and liquid extraction. J Radionanal Nucl Chem 288 (2011) 753–758

86. R. Pöllänen, T. Siiskonen, M. Moring, J. Juhanoja, Direct alpha spectrometry for charactherising hot particle properties, Radiation Measurements, 4, 10 (2007) 1666–1673.

87. T. Siiskonen, R. Pöllänen, Advanced simulation code for alpha spectrometry, Nuclear Instruments and Methods in Physics Research Section A: Accelerators, Spectrometers, Detectors and Associated Equipment, 550, 1–2 (2005) 425–434.

88. R. Pöllänen, T. Siiskonen, Minimum detectable activity concentration in direct alpha spectrometry from outdoor air samples: continuous monitoring versus separate sampling and counting, Health Physics, 90 (2006) 167-175.

89. R. Pöllänen, T. Siiskonen, High-resolution alpha spectrometry under field conditions – fast identification of alpha particle emitting radionuclides from air samples, Journal of Environ-mental Radioactivity, 87 (2006) 279-288.

90. T. Siiskonen, R. Pöllänen, New approach to alpha spectrum analysis: Iterative Monte Carlo simulations and fitting, Progress in Nuclear Science and Technology, 2 (2011) 437-441.

91. O’Neil, K. D., He, H., Keech, P., Shoesmith, D. W., Semenikhin, O. A. Anisotropy of Local Conductivity of Hyper-Stoichiometric Uranium Dioxide Revealed by Current-Sensing Atomic Force Microscopy (CS-AFM). Electrochem. Commun. (2008) 10, 1805−1808.

92. Lucuta, P. G., Verall, V. R., Maztke, Hj., Palmer, B. J., Microstructural Features of SIMFUEL − Simulated High-Burnup UO_2-Based Nuclear Fuel. J. Nucl. Mater. (1991) 178, 48−60.

93. Zetterström Evins, L., Vähänen, M. (eds.) 2012: REDUPP First Annual Report, Posiva Oy, Olkiluoto, Finland, Posiva Working Report 2012-28 (2012). 44p.

94. Rand, M, Mompean, F., Perrone, J., and Illemasséne M., Chemical Thermodynamics of Thorium, 2008, OECD Publishing

95. Rousseau, G.; Fattahi, M.; Grambow, B.; Boucher, F.; Ouvrard, G., Coprecipitation of thorium and lanthanum with UO2þx(s) as host phase. Radiochim. Acta 94 (2006) 517-522

96. Heisbourg, G. Synthese, caracterisation et etudes cinetique et thermodynamique de la dissolution de ThO_2 et des solutions solides Th_1-xMxO_2 (M = U, Pu). Universite Paris XI, Orsay, (2003)

97. Jernström, J.; Vuorinen, U.; Hakanen, M. Solubility of thorium in 0.1 M NaCl solution and in saline and fresh anoxic reference groundwater; (2002)

98. Rai, D.; Moore, D. A.; Oakes, C. S.; Yui, M. Thermodynamic Model for the Solubility of Thorium Dioxide in the Na-Cl-OH-H_2O System at 23°C and 90°C, Radiochim. Acta, 88 (2000) 297-306

99. Ollila K., Albinson Y., Cowper M., Dissolution rates of unirradiated UO_2, UO_2 doped with ^{233}U, and spent fuel under normal atmospheric conditions and under reducing conditions using an isotope dilution method (2003) SKB Technical Report TR-03-13

100. Pearce, C., Saldi, G., Schott, J., Olkers E., Isotopic fractionation during congruent dissolution, precipitation and at equilibrium: Evidence from Mg Isotopes, Geochimica et Cosmochimica Acta 92 (2012) 170-183

101. Mavromatis V., Pearce, C., Shirokova L., Bundeleva I., Pokrovsky O., Benezeth, P., and Olkers E., Magnesium isotope fractionation during hydrous magnesium carbonate precipitation with and without cyanobacteria, Geochimica et Cosmochimica Acta 76 (2012) 161-174

102. Currie L.A. Detection and quantification limits: origins and historical overwiew. Anal Chim Acta 391 (1999) 127–134

103. Von Oertzen, G. and von Oertzen, D. (2012) Questions Answered About Uranium and Radiation, Chamber of Mines Uranium Institute.

PUBLICATION I

Solution composition and particle size effects on the dissolution and solubility of ThO_2 microstructural analogue for UO_2 matrix of nuclear fuel

In: Radiochim. Acta 2015; 103(8): 565-576

DE GRUYTER Radiochim. Acta 2015; 103(8): 565–576

Emmi Myllykylä*, Tiina Lavonen, Martin Stennett, Claire Corkhill, Kaija Ollila, and Neil Hyatt

Solution composition and particle size effects on the dissolution and solubility of a ThO_2 microstructural analogue for UO_2 matrix of nuclear fuel

Abstract: The objective of this study was to investigate the dissolution rate of ThO_2 which was synthesised to approximate, as closely as possible, the microstructure of UO_2 in a nuclear fuel matrix. The optimal sintering temperature for ThO_2 pellets was found to be 1750 °C, which produced pellets with a microstructure similar to UO_2 nuclear fuel pellets, with randomly oriented grains ranging in size from 10 to 30 µm. Dissolution was conducted using ThO_2 particles of different size fractions (80 to 160 µm and 2 to 4 mm) in the presence and absence of carbonate, in solutions with pH from 2 to 8 and at 80 °C. Dissolution rates were calculated from Th released from the solid phase to solution. Particles of ThO_2 were also leached with 1 M HNO_3 at 80 °C in order to investigate the morphological changes at the particle surfaces. The concentration of Th was found to be $\geq 10^{-9}$ mol/L at pH ≤ 4, lower than the theoretical solubility of crystalline ThO_2. At higher pH values, from 4 to 8, the measured concentrations (10^{-10} to 10^{-12} mol/L) were between the theoretical solubility of ThO_2 and $Th(OH)_4$. Grain boundaries were shown to exert an influence on the dissolution of ThO_2 particles. Using high resolution aqueous solution analysis, these data presented here extend the current understanding of Th solubility in solution.

Keywords: ThO_2, nuclear fuel analogue, dissolution, solubility, HR-ICP-MS.

DOI 10.1515/ract-2014-2271
Received March 31, 2014; accepted February 19, 2015

1 Introduction

Thorium dioxide (ThO_2) is isostructural to UO_2, sharing the same fluorite-type structure (space group Fm3m), making it a useful structural analogue for spent nuclear fuel, which is predominantly composed of UO_2 (> 95%). However, unlike $U^{(IV)}O_2$, $Th^{(IV)}O_2$ is not redox active since Th has only one prevailing oxidation state, +4 [1]. The next generation applications of nuclear energy have shown interest towards thorium [2]. As a fuel, thorium has many beneficial properties, such as high fusion temperature, good sintering capability, resistance against radiation damage, greater abundance in the Earth's crust compared to U, and the possibility for transmutation [2].

The preferred option worldwide for the long-term disposal of spent nuclear fuel, and potentially future Th-based nuclear fuels, is disposal in a deep geological disposal facility, several hundreds of metres below ground [3, 4]. In this environment, the release of Th and other radionuclides to the geo- and bio-spheres will be controlled by the dissolution of the fuel by groundwater. Hence it is necessary to understand the dissolution behaviour of the fuel and the solubility of radionuclides in groundwater.

In the literature, the solubility values for ThO_2, and also the hydrolysis constants of thorium, show great discrepancies e.g. Vandenborre et al. 2008, 2010 Neck and Kim, 2001 [5–7]. The main reasons for these differences include: the tendency of Th to undergo polynucleation and colloid formation, its strong absorption to surfaces, and the low solubility of Th(IV) hydroxide and hydrous oxide. The presence of complexing ligands like CO_3^{2-} [8] has also been shown to increase the solubility of ThO_2. These characteristics of thorium together with the relatively low solubility of ThO_2(cr) make solubility studies of ThO_2 challenging.

The solubility product values have been observed to vary between ThO_2 (microcryst.) ($\log K^\circ_{sp} = -53\pm0.5$) and $Th(OH)_4$ (am) ($\log K^\circ_{sp} = -46.7\pm0.9$) [9–11] depending on the crystallinity and crystallite size of the Th(IV) oxide and hydroxide or oxyhydroxide phase. The predicted value, ac-

---

***Corresponding author: Emmi Myllykylä,** VTT Technical Research Centre of Finland, Espoo, Finland, e-mail: emmi.myllykyla@vtt.fi
Tiina Lavonen, Kaija Ollila: VTT Technical Research Centre of Finland, Espoo, Finland
Martin Stennett, Claire Corkhill, Neil Hyatt: Immobilisation Science Laboratory, Department of Materials Science and Engineering, The University of Sheffield, Mappin Street, Sheffield, S1 3JD, UK

cording to the Equation of Schindler [12] and experimental data for ThO_2 (cr) is $\log K^{\circ}_{sp} = -54.2 \pm 1.1$ [9]. In addition to crystallinity, surface phenomena have been discussed as a possible factor affecting the solubility properties. Vanderborre et al. 2010 [6] combined investigation of solid surfaces with leaching experiments, and isotopic exchange methods to understand the discrepancy in solubility values and to describe the reversibility in the exchange mechanism. They observed that the dissolution mainly occurred at grain boundaries and showed variation between different sites, indicating "local solubility" effects. In addition, the usage of ^{229}Th spiking revealed dynamic dissolution/precipitation reactions on the solid/solution interface.

Many solubility studies have been conducted with amorphous phases of ThO_2 [13–17] because its solubility, compared to well-crystalline ThO_2, simplifies the analysis of Th in liquid phase. Crystalline phases of ThO_2 have also been studied [18, 19]. Hubert et al. [18] observed the effect of surface properties on the leachibility of solid ThO_2. Factors including specific surface area, surface state and size of aggregates were found to have influence on the apparent solubility. However, when the leaching rate was normalized to surface area, it seemed to be independent of the surface characteristics.

The aims of this study were to prepare crystalline ThO_2 pellets having a microstucture similar to that of spent UO_2 nuclear fuel pellets and to conduct dissolution experiments, in order to further evalauate the relative solubility of ThO_2 phases. We report the initial release rate of Th during the first 20 to 40 days of dissolution. Solubility studies were extended to 100 to 120 days to gain a thorough understanding of the solubility limit of different ThO_2 phases.

The first experiment series in the solubility and dissolution rate studies was conducted with 2 to 4 mm particles in 0.1 M NaCl and 0.01 M NaCl with 2 mM $NaHCO_3$ solutions under atmospheric conditions. The second experiment series was conducted with two particle sizes, 60 to 180 µm and 2 to 4 mm, in 0.1 M NaCl and 0.01 M HNO_3 solutions in an Ar glove box to exclude atmospheric carbon. In addition, several accelerated leaching experiments were run in 1 M HNO_3 solution and at 80 °C in order to observe surface changes during dissolution in a relatively short time scale.

2 Experimental

2.1 Preparation of ThO_2 pellets

Thorium dioxide pellets were prepared to approximate the microstructure of UO_2 fuel [19–21], with grain sizes in the range of 5–30 µm, with random crystallographic orientation. The precursor material was ThO_2 powder (BDH (British Drug House) Laboratory Reagents Ltd., Lot No: G83757/541012), which was confirmed as pure ThO_2 by powder X-ray Diffraction using STOE Cu-IP diffractometer, with a Cu K_α source (diffraction patterns were collected at $20 < 2\theta < 60^{\circ}$ at 2° min^{-1}, using a step size of 0.02°). 1 g of ThO_2 powder was placed within a 10 mm diameter hardened stainless steel die and uniaxially pressed with a load of 100 MPa. The green density (i.e. compacted density) of the pressed compacts was calculated prior to sintering by measuring the pellet mass and geometry. Green ThO_2 pellets, placed on stabilised zirconia setter plates, were sintered in triplicate for 4 h at temperatures between 1300 and 1750 °C in a standard air atmosphere muffle furnace. Pellets were heated and cooled with a ramp rate of 5 °C min^{-1} and held at the sintering temperature for 4 h.

The sintered density of the pellets was measured using geometric and water immersion (Archimedes) methods. All density measurements were performed in triplicate.

For surface analysis only (i.e. not dissolution experiments) ThO_2 pellet samples were polished to a 1 µm finish using SiC paper and diamond paste. A final mechanico-chemical etch was performed using a 0.06 µm colloidal silica solution. In order to develop a grain boundary texture at the surface of the pellets, annealing was performed at 90% of the sintering temperature, at a ramp rate of 5 °C min^{-1} and held at the annealing temperature for 1 h. Pellets were imaged using an optical microscope. Analysis of the crystallographic orientation and grain size distribution of pellets was performed using Electron Backscatter Diffraction Analysis (EBSD) (Oxford Instruments) in conjunction with a Sirion Field Emission SEM. EBSD maps of 100 µm^2 were obtained at an accelerating voltage of 20 kV and a 0.5 µm step size. Grain orientation analysis was performed on > 10 000 grains, using HK Channel 5 software (Oxford Instruments).

2.2 Fragmentation of the pellets

ThO_2 pellets were crushed using a percussion mortar. Particles between 2 and 4 mm were selected with tweezers and washed in isopropanol and ethanol, followed by gravitational settling to remove adhering fine fragments.

For the smaller particle size (80–160 µm), intact pellets of ThO_2 (~ 20 g) were fragmented using the electrodynamic fragmentation method [22, 23]. The principles of the method can be briefly described, as follows: electrical energy in the form of repeated high voltage pulses is applied to the samples immersed in a dielectric process liquid. Dielectric liquids, like water, have a high dielectric strength, when the voltage rise time is kept below 500 ns. As such, the discharges are forced to occur through the immersed material. Plasma channels and explosions were generated inside the pellets and the resulting shockwaves produced fracturing and physical breakdown.

Fragmentation was conducted using a batch scale selFrag instrument available at the Research Laboratory of the Geological Survey of Finland. Approximately 20 g of ThO_2 pellets were subjected to a two stage treatment. The process liquid used was regular tap water. After the first fragmentation the sample was classified using 0.2 mm net sieve, and the remaining oversized fraction (ca. 14 g) was re-fragmented. The process parameters used for both the first and second fragmentation procedure were: number of pulses 400, e-gap 10 mm, freq. 3 and voltage 120–140 kV.

The fragmented material was washed using tap water and any iron contamination from the electrode was removed using hand magnets. The final product for use in dissolution experiments was sieved to a particle size fraction of 80 to 160 µm.

2.3 Dissolution experiments

The first experiment series of solubility and dissolution rate studies were conducted with 2 to 4 mm particles in 0.1 M NaCl and 0.01 M NaCl with 2 mM $NaHCO_3$ solutions under atmospheric conditions (solutions were prepared from suprapure (99.99%, Merck) NaCl and $NaHCO_3$ (ACS, Reag.Ph Eur, Merck KGaA) in MilliQ-water). Experiments were conducted in triplicate at room temperature ($23 \pm 1\,^\circ C$) for up to 115 d. Approximately 300 mg of crushed ThO_2 particles were placed in a 60 ml high density polypropylene vessel with 50 ml of leaching solution. The second experiment series was conducted with two particle sizes (60 to 180 µm and 2 to 4 mm), both in 0.1 M NaCl and 0.01 M HNO_3 (prepared from concentrated HNO_3, ULTREX II by J.T Baker) within an Ar glove box at $25 \pm 1\,^\circ C$. The duration of these experiments, conducted in duplicate, was 93 d. Approximately 150 mg of particles were placed in a 60 ml vessel with 50 ml of leaching solution. Polypropylene vessels were used for experiments with 0.01 M HNO_3, and high density perfluoroalkoxy Teflon vessels were used for 0.01 M NaCl solutions, in order to decrease the potential sorption of Th to the reaction vessel under near neutral conditions.

In the first experiment series, conducted under atmospheric conditions, sampling was performed at 0, 1, 3, 6, 15, 24, 31 41, 48, 79, 100 and 115 d by withdrawing a 2.5 ml sample. Each sample was ultrafiltered with a Pall Mall filtration device with 10 kD (~ 1 nm) molecular cut off, using centrifugation (6000 rpm, 1 h). In addition, some samples were taken and not filtered. The pH was measured directly from the test solution with ROSS combination electrode at the beginning of the experiment and after 35 days of reaction time.

Sampling of the experiment series under an Ar atmosphere was conducted at 0, 1, 2, 5, 7, 9, 14, 21, 30, 43, 57, 70 and 89 d. Both non-filtered and ultrafiltered samples (as above) of 2.5 ml were taken. The pH was measured in solutions under Ar glovebox conditions as above directly from the reaction vessel within every second sampling.

The concentration of ^{232}Th in non-filtered and ultrafiltered samples was analysed with a High Resolution sector Field Inductively Coupled Plasma-Mass Spectrometer (HR-ICP-MS, Element2 by ThermoScientific). Standard solutions with known concentrations were diluted from AccuTrace^{TM} Reference Standard SQS-01. A control sample for analysis was prepared from standard CLMS-1 solution by SPEX. All the blank, standard and control samples contained a known amount of an internal standard, indium. Analyses of ^{232}Th were performed with HR-ICP-MS in low resolution mode ($R \approx 300$). The detection limit for thorium was calculated as six times the standard deviation of the ion counts obtained for the sample blanks (ten replicates), divided by the sensitivity of the 1 µg/L standard solution of Th. The detection limit for thorium was therefore found to be between 1×10^{-12} mol/L and 4×10^{-12} mol/L depending on the solution matrix and daily efficiency of the instrument. The uncertainty of the Th analyses increased up to 10% when the measured concentration was close to the detection limit. With higher concentration the uncertainty of the analysis was a few percent.

The dissolution rate ($r_{^{232}\mathrm{Th}}$ [mol g^{-1} s^{-1}]) for ThO_2 was calculated by using Equation (1)

$$r_{^{232}\mathrm{Th}} = \frac{V}{m}\frac{\mathrm{d}c_{^{232}\mathrm{Th}}}{\mathrm{d}t} \tag{1}$$

where V is the volume of the solution [L], m is the mass [g] of ThO_2 and $\mathrm{d}c/\mathrm{d}t$ is the slope (linear fit) determined from the evolution of ^{232}Th release as function of time [mol L^{-1} s^{1}]. This analysis is similar to that applied to consideration of mineral dissolution elsewhere e.g. in Rozalen et al, 2008, Malmström M., 1996, Brady and Walther 1990 [24–26].

The surface area was calculated by assuming that the ThO_2 particles are cubes (which is not true as is commonly known see e.g. [27]) and using the measured density of ThO_2 pellets approximately 9 g/cm^3 (~ 93% of the theoretical 9.86 g/cm^3) [28].

$$\begin{aligned}
\rho_{\mathrm{ThO_2}} &= \frac{m_{\mathrm{ThO_2}}}{V_{\mathrm{tot,ThO_2}}}\\
V_{\mathrm{grain}} &= d^3\\
N_{\mathrm{grain,ThO_2}} &= \frac{V_{\mathrm{tot,ThO_2}}}{V_{\mathrm{grain}}}\\
A_{\mathrm{grain,ThO_2}} &= 6d^2_{\mathrm{grain,ThO_2}}\\
SA_{\mathrm{tot,ThO_2}} &= N_{\mathrm{grain,ThO_2}} A_{\mathrm{grain,ThO_2}} = 6\frac{m_{\mathrm{ThO_2}}}{\rho_{\mathrm{ThO_2}}}\frac{1}{d_{\mathrm{ThO_2}}} \qquad (2)
\end{aligned}$$

2.4 Characterization of leached ThO_2 surfaces with SEM

The ThO_2 particles were subjected to leaching experiments in acidic conditions and at elevated temperatures in order to monitor the evolution of surface morphology during dissolution. For detailed characterisation of the pellet morphology during dissolution, see Corkhill et al. [29]. Surface characterisation was performed on particles in the 80 to 160 μm size fraction after immersion in a 1 M HNO_3 (~ pH 1) solution at 80 °C for 2 and 4 weeks under Ar atmosphere. Prior to heating, the reaction vessels were placed in a sealed steel container under Ar atmosphere of the glove box to maintain argon atmosphere. Surfaces of ThO_2 subject to this treatment were studied with SEM (JEOL JSM-900LV with Oxford Instruments) using an accelerating voltage of 20 kV and beam size of 10 μm.

3 Results and discussion

3.1 The properties of sintered ThO_2 pellets

Figure 1 shows the X-ray diffraction analysis of ThO_2 power, confirming the purity of the starting material. The characteristics for a suitable UO_2 fuel analogue include a grain size on the order of 8–15 μm, a sintered density of > 95.5% theoretical density, and randomly orientated grains. The sintering temperature was varied in order to determine the optimal sintering conditions to create such characteristics. Figure 2 shows the densities of the sintered pellets (defined as the % of the theoretical density, 10 g/cm^3) as a function of sintering temperature.

The density of the pellets increased with increasing sintering temperature up to 1750 °C (Figure 2); this temperature gave a density of 93% of the theoretical density, which is slightly below optimal for a UO_2 analogue. Heating at higher temperatures caused a loss of pellet integrity, therefore 1750 °C was the highest sintering temperature evaluated. The increase in density with increasing sintering temperature is consistent with decreasing porosity and increasing grain size, as shown by optical microscope images in Figure 3. The grain size was found to increase from 2–10 μm at 1650 °C to 10–30 μm at 1750 °C (Table 1). Sintering at 1750 °C was, therefore, found to give the optimum grain size and density achievable. EBSD analysis was performed to determine grain size and crystallographic orientation. The average grain size was found to be 13 μm (based upon analysis of > 10 000 grains). Figure 4 shows that synthesis at 1750 °C produced grains that were randomly orientated in the ⟨111⟩, ⟨100⟩ and ⟨101⟩ crystal planes.

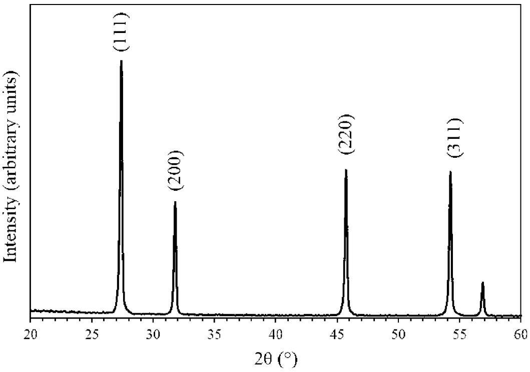

Fig. 1: XRD pattern for thorium dioxide powder used to synthesise UO_2-fuel analogue pellets for dissolution experiments.

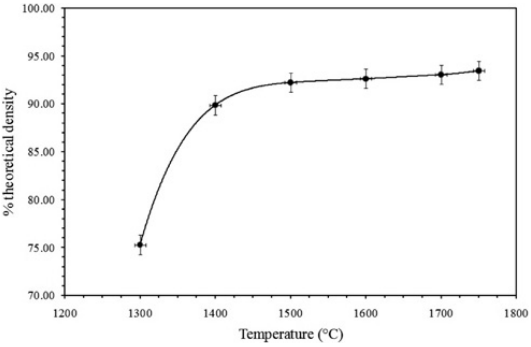

Fig. 2: Density of the sintered ThO_2 as function of sintering temperature.

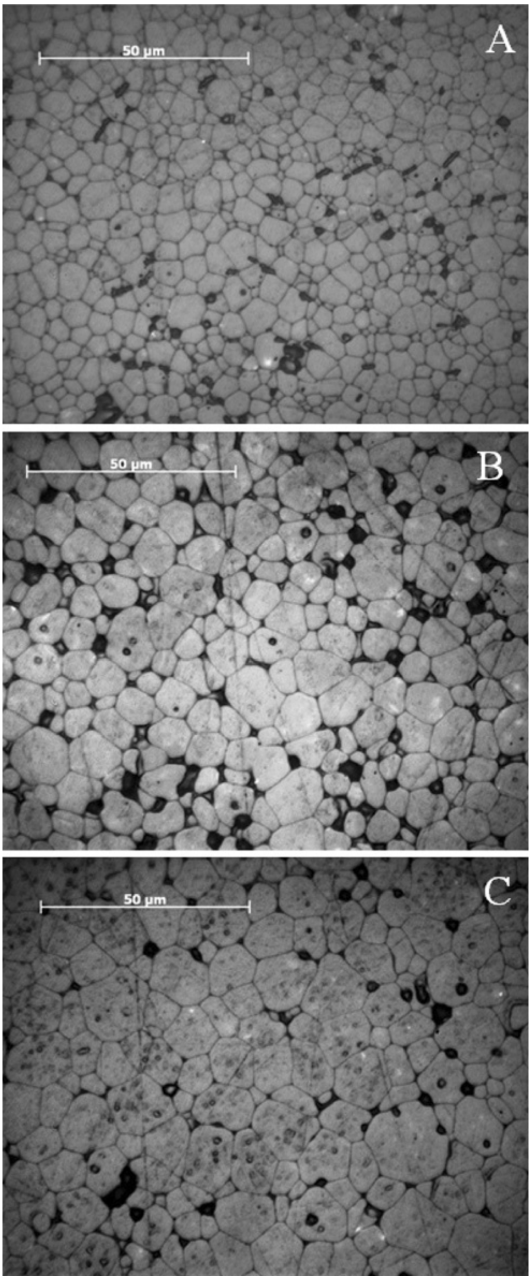

Fig. 3: Optical microscopy images of the ThO_2 pellet surface sintered at 1600 (A), 1700 (B), and 1750 °C (C).

Table 1: The grain size of ThO_2 pellets as a function of sintering temperature.

Sintering temperature (°C)	Grain size (µm)
1600	2–10
1700	5–20
1750	10–30

3.2 Particle characteristics after selFrag HV pulsing

Fragmentation of the ThO_2 pellets produced randomly shaped ThO_2 particles, as confirmed by optical and electron microscopy (Figures 5 and 6). Similar randomly broken grains typically result from applying conventional comminution techniques e.g. grinding. However, adhered fines, normally seen in SEM images showing products from conventional comminution, were not observed, due to the pulse fragmentation procedure. Adhered-particle free surfaces can be regarded as ideal samples for the dissolution experiments undertaken in this study.

The particles exhibited two main textures: those with a grain boundary texture and those without, as shown in Figure 6. Grain boundaries were formed in these particles through two processes. Firstly, prior to fragmentation, surfaces of the original pellets developed a grain boundary texture through high temperature annealing. It may also be possible that such surfaces originate from the pulse fragmentation process, which forces liquid through grain boundaries to break the particles apart, leaving behind several surfaces with a grain boundary texture.

3.3 Dissolution experiments

3.3.1 ThO_2 dissolution under atmospheric conditions

Figure 7 shows the dissolution data for ThO_2 particles (2–4 mm) leached in air in 0.1 M NaCl or in 0.01 M NaCl with 2 mM $NaHCO_3$. In the solution containing carbonate (Fig. 7a), a maximum concentration of Th of $\sim 10^{-10}$ mol/L was measured in non-filtered samples after 6 days of dissolution. After 40 days the concentration plateaued at approximately 10^{-12} mol/L. The ultrafiltered samples reached a concentration of between 10^{-11} and 10^{-12} mol/L at 40 d, preceded by a steady increase in concentration from 10^{-13} mol/L. The initial pH value of 8.4 decreased slightly to pH 8.2 during the first 35 days of the experiment. In the 0.1 M NaCl solution, shown in Figure 7b,

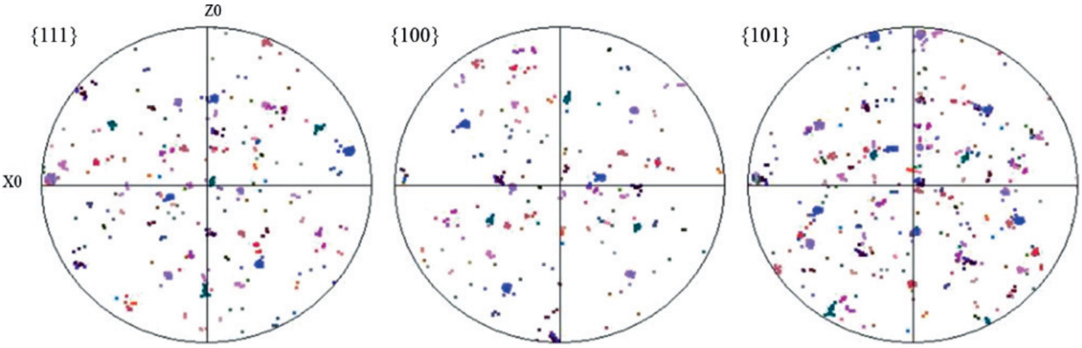

Fig. 4: Representative crystal orientations of a pressed pellet of ThO_2 sintered at 1750 °C and annealed at 1500 °C to develop grain structure. Pole figures show the random orientation of the grains in the ⟨111⟩, ⟨100⟩ and ⟨101⟩ crystal planes.

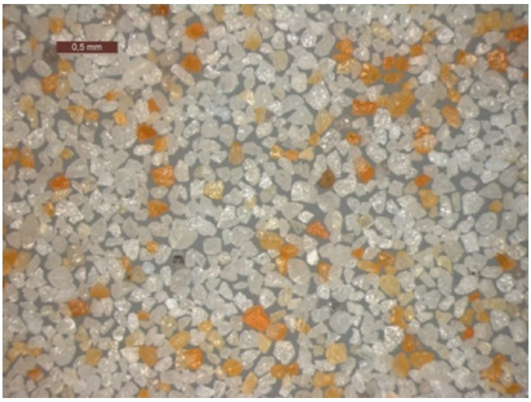

Fig. 5: An image of 80 to 160 μm ThO_2 particles taken with a biocular stereomicroscope.

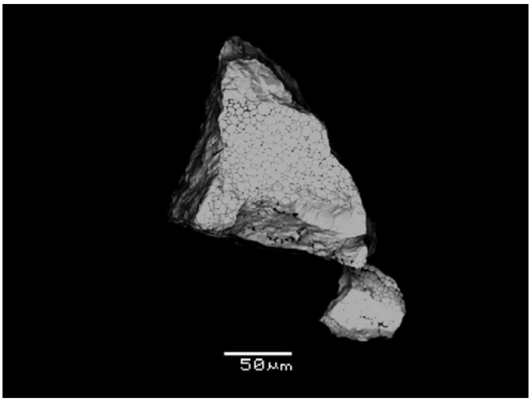

Fig. 6: SEM image of 80 to 160 μm ThO_2 particle crushed using the SelFag pulse fragmentation technique (330× magnification).

the increase of the measured concentration was not obvious; the concentrations in both non-filtered and ultrafiltered samples are scattered (Figure 7b) most probably due to the concentrations occurring close to the analytical detection limit (1×10^{-13} mol/L). The concentration of Th in the ultrafiltered samples decreased below this detection limit of after 48 days sampling. The initial pH of the 0.1 M NaCl increased from 5.4 to pH 5.8 during the first 35 days of the experiment.

When comparing the results of the two experiments, the solubility and the dissolution rates were greater in the solution containing carbonate (1×10^{-13} mol dm^{-3} d^{-1}), likely due to the formation of Th-containing carbonate/hydroxide complexes. In the absence of carbonate (0.1 M NaCl solution) there was no clear trend, however, if the dissolution rate is estimated from ultrafiltrated samples, the obtained value was found to be 2×10^{-14} mol dm^{-3} d^{-1}, an order of magnitude less than that in the carbonate-containing solution. In the oxic conditions utilised in these experiments (which were conducted in air), dissolved carbon dioxide from the atmosphere may have had a slight solubility increasing effect in the bi-carbonate-free solution. The increasing effect of carbonate complexation on the solubility of thorium in each of the applied experimental conditions was previously evaluated by geochemical modelling (PHREEQC) [30]. A second set of experiments was therefore conducted under inert Ar atmosphere, to exclude such effects.

3.3.2 ThO_2 dissolution in anaerobic conditions

The dissolution data resulting from the leaching of 80 to 160 μm and 2–4 mm particles of ThO_2 in 0.1 M NaCl

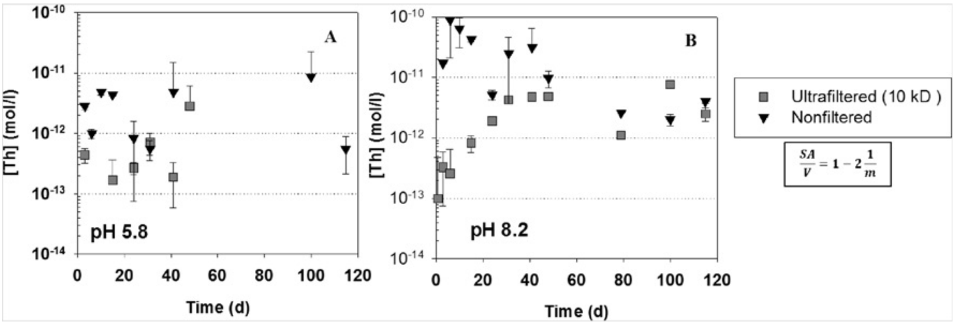

Fig. 7: Evolution of Th concentrations in ultrafiltered and non-filtered experiments of 2–4 mm ThO_2 particle dissolution in (A) 0.01 M NaCl with 2 mM $NaHCO_3$ and (B) in 0.1 M NaCl, both under atmospheric conditions, at a temperature of 23 °C.

under an Ar atmosphere are shown in Figure 8. Unfiltered samples arising from the smaller size fraction (80 to 160 μm) demonstrated a relatively rapid initial increase in Th concentration to ~ 8×10^{-10} mol/L after 2 days of dissolution, followed by a progressive decrease to 4×10^{-11} mol/L by 89 days (Figure 8a). Under the same conditions, ultrafiltered samples (Figure 8b) gave a maximum Th concentration of ~ 4×10^{-10} mol/L after 7 days of leaching. After 9 days of dissolution, the concentration of Th decreased below 1×10^{-11} mol/L and remained at ~ 2×10^{-12} mol/L after 57 days.

In the experiments with size fraction 2 to 4 mm, the maximum concentrations of Th were reached after 23 days of dissolution (3×10^{-9} mol/L and 7.4×10^{-10} mol/L for non-filtered and ultrafiltered samples, respectively) (Figure 8c and 8d). This suggests that dissolution and precipitation/sorption kinetics are also slower in these samples, which is likely related to the lower surface area resulting from the larger particle size; the saturation limit is reached more slowly because there is less surface area available for sorption and precipitation of secondary Th compounds.

The initial pH of the 2–4 mm ThO_2 dissolution experiments was found to decrease rapidly from pH 8 to between pH 5 and pH 6, where it remained for the duration of the experiment. This unexpected result is likely due to the leaching of H^+ from incompletely rinsed reaction vessels.

Parallel, ultrafiltered experiments conducted for the 2–4 mm particle size (designated A and B, Figure 8d) showed considerable variation in concentration, by almost one order of magnitude. This may be due to the influence of pH in the test solutions; experiment A had a pH value of 4.8, while experiment B gave a pH value of 5.3. At the conclusion of the experiment, the Th concentrations were 7×10^{-12} mol/L (experiment A, pH 4.8) and 3×10^{-10} mol/L (experiment B, pH 5.3). While the difference in pH was only small, these observations confirm the fact that the solubility of ThO_2 is highly dependent on the H^+ activity in the solution [9–11].

3.3.3 ThO_2 dissolution as a function of particle size

To investigate further the influence of particle size on the dissolution of ThO_2, experiments were conducted in 0.01 M HNO_3, where dissolved Th concentrations far exceeded the analytical detection limit of Th, allowing for an accurate determination of the effects of particle size on dissolution rate. For 80 to 160 μm particles of ThO_2 (Figure 8e and f), the concentration in the non-filtered samples increased rapidly to 5×10^{-8} mol/L after 5 days of dissolution. Similarly, in the ultrafiltered samples, the Th concentration increased to 4×10^{-8} mol/L over the same time period. After this initial rapid dissolution, the concentration of Th decreased to levels between 3×10^{-8} and 4×10^{-8} mol/L for the duration of the 90 days experiment, in both non-filtered and ultrafiltered samples.

For the 2 to 4 mm ThO_2 particles, the initial dissolution rate was slower than that of the smaller particle size. The maximum concentration of Th was reached after 30 days of dissolution, giving values of 6.5×10^{-8} mol/L and 8.5×10^{-8} mol/L for duplicate samples (Figure 8g,h). The final concentration of Th was ~ 5×10^{-8} mol/L after 90 days, which was slightly higher than the final concentration arising from the smaller particle size (~ 3×10^{-8} mol/L) (Figure 8e–f). This suggests that particles with a greater surface area (e.g. 80–160 μm size fraction) reach lower maximum concentrations than particles with lower surface area (e.g. 2–4 mm particles) a result of more surface sites available for sorption of secondary precipitates. Such precipitates attenuate further dissolution of the surface. A similar effect was observed for particles subject

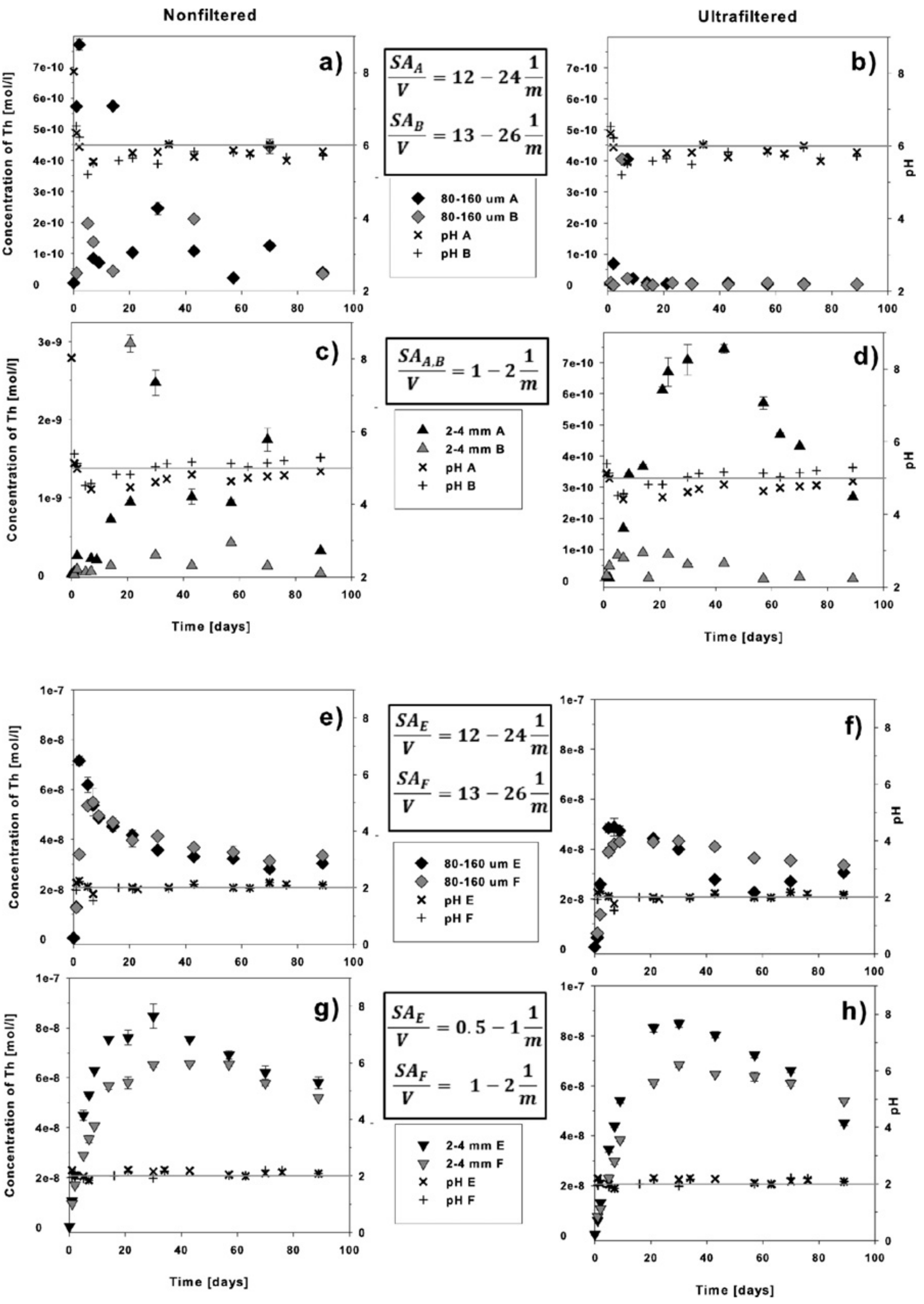

Fig. 8: The evolution of Th concentration and pH in 0.1 M NaCl (a, b, c, d) and in 0.01 M HNO_3 (e, f, g, h) with particle sizes 80 to 160 µm (a, b, e, f) and 2 to 4 mm (c, d, g, h) at 25 °C. The results of the Non-filtered samples are given on the left and the ULTRAfiltered ones on the right. The solid lines were sketched to guide the eye to follow the pH values. Filtrations, solutions and particle sizes presented here are also shown with references to this Fig. in Table 2. (Symbols A and B (E and F) in legend boxes refer to the parallel experiments).

Table 2: The initial dissolution rates [$mol/g^{-1}\,s^{-1}$] calculated for samples A and E and their parallel samples B and F, according to Equation (1).

Atmosphere and filtration	Solution	pH	Particle size	Test A (E) slope, dc/dt [$mol\,L^{-1}\,day^{-1}$]	Test A (E) rate [$mol\,g^{-1}\,s^{-1}$]	Test B (F) slope, dc/dt [$mol\,L^{-1}\,day^{-1}$]	Test B (F) rate [$mol\,g^{-1}\,s^{-1}$]	Data in Figure
Air (filtered)	0.01 M NaCl (2 mM $NaHCO_3$)	8	2–4 mm	1.0×10^{-13}	**2.0×10^{-19}**			Figure 7B
Air (filtered)	0.1 M NaCl	6	2–4 mm	2.0×10^{-14}	**4.1×10^{-20}**			Figure 7A
Air	0.01 M NaCl (2 mM $NaHCO_3$)	8	2–4 mm	5.0×10^{-12}	1.1×10^{-17}			Figure 7B
Air	0.1 M NaCl	6	2–4 mm	3.0×10^{-13}	6.1×10^{-19}			Figure 7A
Argon (filtered)	0.1 M NaCl	6	80–160 μm	5.4×10^{-11}	**2.1×10^{-16}**	2.9×10^{-11}	**1.1×10^{-16}**	Figure 8b
Argon (filtered)	0.1 M NaCl	5	2–4 mm	2.9×10^{-11}	**1.0×10^{-16}**	8.4×10^{-12}	**2.1×10^{-17}**	Figure 8d
Argon (filtered)	0.01 M HNO_3	2	80–160 μm	6.7×10^{-09}	**2.7×10^{-14}**	5.8×10^{-09}	**2.2×10^{-14}**	Figure 8f
Argon (filtered)	0.01 M HNO_3	2	2–4 mm	6.3×10^{-09}	**2.3×10^{-14}**	4.4×10^{-09}	**1.7×10^{-14}**	Figure 8h
Argon	0.1 M NaCl	5	80–160 μm	4.2×10^{-10}	1.7×10^{-15}	1.5×10^{-10}	5.6×10^{-16}	Figure 8a
Argon	0.1 M NaCl	4	2–4 mm	4.4×10^{-11}	1.5×10^{-16}	9.2×10^{-12}	2.3×10^{-17}	Figure 8c
Argon	0.01 M HNO_3	2	80–160 μm	3.1×10^{-08}	1.3×10^{-13}	9.3×10^{-09}	3.5×10^{-14}	Figure 8e
Argon	0.01 M HNO_3	2	2–4 mm	6.5×10^{-09}	2.4×10^{-14}	4.4×10^{-09}	1.7×10^{-14}	Figure 8g

If reader is interested in calculating the dissolution rate to units [$mol\,m^{-2}\,s^{-2}$], one can e.g. divide the values by 3.3 cm^2/g in cases of 2 mm particle size and 80 cm^2/g in cases of 80 μm.

to dissolution in 0.1 M NaCl (described above). However, unlike the dissolution experiments conducted in 0.1 M NaCl, where dissolution rates were clearly affected by filtration and hence, the presence of colloidal species, the evolution of Th concentration in 0.01 M HNO_3 was independent of the sampling method; the concentrations of the ultrafiltered samples were very similar to the non-filtered ones. This indicates that secondary phases or colloids did not play a significant role in these experiments. One possible explanation may be effects arising from high energy sites on the surface, for example grain boundaries (shown in Figure 6). The larger particles comprise surfaces with more grains than the smaller particles, therefore they have a greater number of grain boundaries. In a recent study [29] it was found that grain boundaries of ThO_2 and CeO_2 analogues for UO_2 fuel dissolved very rapidly in 0.01 M HNO_3. Therefore, the higher maximum concentrations found for the large particles may be due to dissolution of grain boundaries

3.3.4 Dissolution rates of ThO_2

The initial dissolution rates of ThO_2 under the experimental conditions investigated were calculated from the evolution of Th concentration during the period of release of Th into solution, which took between 5 to 30 days, depending on the liquid phase in question.

Calculated rates were obtained from linear regression of these data, and are given in Table 2. The results clearly show the pH dependence of the dissolution rate and the increasing effects of carbonate concentration and particle size. The dissolution rates were found to be greatest at low pH and in the presence of carbonate. Small differences were also observed between parallel experiments and in the comparison between results calculated from non-filtered and ultrafiltered samplings.

The presence of carbonates is known to increase the solubility of ThO_2, which can have a significant effect on the behaviour of Th(IV) in natural groundwaters. One order of magnitude increase in [CO_3^{2-}] has been shown to increase the solubility of hydrous ThO_2(am) by up to five orders of magnitude [31]. Two mononuclear carbonate complexes of Th(IV), $Th(OH)_3CO_3^-$ and $Th(CO_3)_5^{6-}$, have been reported [31, 32]. Considerably higher Th(IV) solubility in the Th(IV)-H_2O-CO_3^{2-} system, indicated the presence of highly charged pentacarbonate species [31]. Using thermodynamic modelling, Kim et al. [8] reported ternary complexes such as $Th(OH)_3CO_3^-$, $Th(OH)_2(CO_3)_3^{4-}$, $Th(OH)(CO_3)_5^{5-}$, $Th(OH)_2CO_3(aq)$, $Th(OH)_2(CO_3)_2^{2-}$, $Th(OH)_4(CO_3)^{2-}$, which are the most probable predominant aqueous Th(IV) species under many natural conditions [8].

At high pH close to pH 11.2, the higher concentration of OH^- ions has been found to enhance the formation of $Th(OH)_4$, and thus decrease the proportion of carbonate complexes in solution. Therefore, the measured solubility of Th(IV) in alkaline solutions is very close to the solubility in carbonate-free solutions [8].

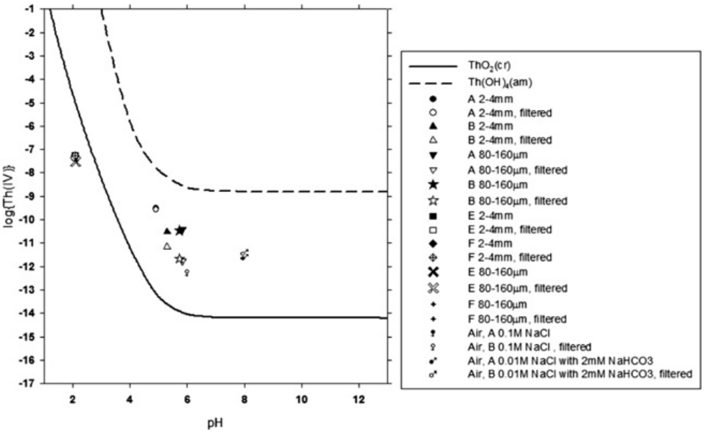

Fig. 9: The solubility levels of Th after ~ 100 d of dissolution in a suite of media investigated in the current work, compared to the Thermochimie equilibrium data for ThO_2 and $Th(OH)_4$ [NEA/TDB].

3.3.5 Solubility of ThO_2

The solubility levels at the end of the experiments were compared with the equilibrium data of ThO_2 and $Th(OH)_4$, which were taken from the Thermochimie database [NEA/TDB] (Figure 9). It should be noted that, for example, in the experiment with 2 to 4 mm particles in 0.1 M NaCl under Ar, there was still some decrease in Th concentration at the end of the 90 days experiment. Thus, the solubility level had probably not been stabilized to a steady state during the experiments. The solubilities measured at pH 2 were at a lower level than would be expected from the thermodynamics. Similar observations have been made by Neck et al. [11]. In their undersaturation dissolution experiments, conducted also with crystalline ThO_2 in acidic conditions, the solubilities stayed below the theoretical solubility of ThO_2. In their experiments they also showed that the value of the solubility product was dependent on the crystallite size. In this study, the solubility values at a pH range of 4 to 8 can be plotted between the theoretical solubilities of crystalline ThO_2 and amorphous $Th(OH)_4$ (Figure 9). Compared to the studies discussed by Neck et al. 2003 and Vandenborre et al. 2010 [6, 11], the values presented here are at an even lower level. This could be an effect of the crystallinity and relatively high sintering temperature of the ThO_2 utilized in these studies, however the usage of a sector field ICP-MS enabled an extremely accurate analyses of dissolved Th concentrations (down to a concentration of 10^{-12} mol/L), which is lower than achievable with conventional quadrupole ICP-MS MS, used in most other studies of Th solubility.

3.4 SEM imaging of leached ThO_2 surfaces

The SEM images of the HNO_3 leached ThO_2 particles revealed that the nature of the dissolution/precipitation phenomenon varied among the particles present in same solution. Some particles did not appear different from the fresh and unreacted particles (see Figures 10a and 6, respectively). However, in a single particle, some surfaces showed textures indicative of grain boundary dissolution (Figure 10b–d), while others appeared to host a "blanket" of secondary phases precipitated from solution. In the former, grain rounding and widening of the grain boundaries was observed (Figure 10b).

These results are in agreement with Corkhill et al. [29] who found that during dissolution in 0.01 M HNO_3, grain boundaries of ThO_2 and CeO_2 analogues for UO_2 fuel dissolved rapidly, giving rise to enhanced initial dissolution rates. Furthermore, they found that surfaces with a grain boundary texture (like those shown in Figure 10a) dissolved at much less rapid rate than surfaces with no grain boundaries, such as those that would be found on the surface of a sintered pellet. This may be the cause of the different particle morphologies described in the current investigation.

4 Conclusions

ThO_2 pellets were synthesised to resemble the microstructure of the UO_2 matrix of nuclear fuel pellets. The pellets sintered at 1750 °C had randomly oriented crystals and a grain size ranging from 10 to 30 µm.

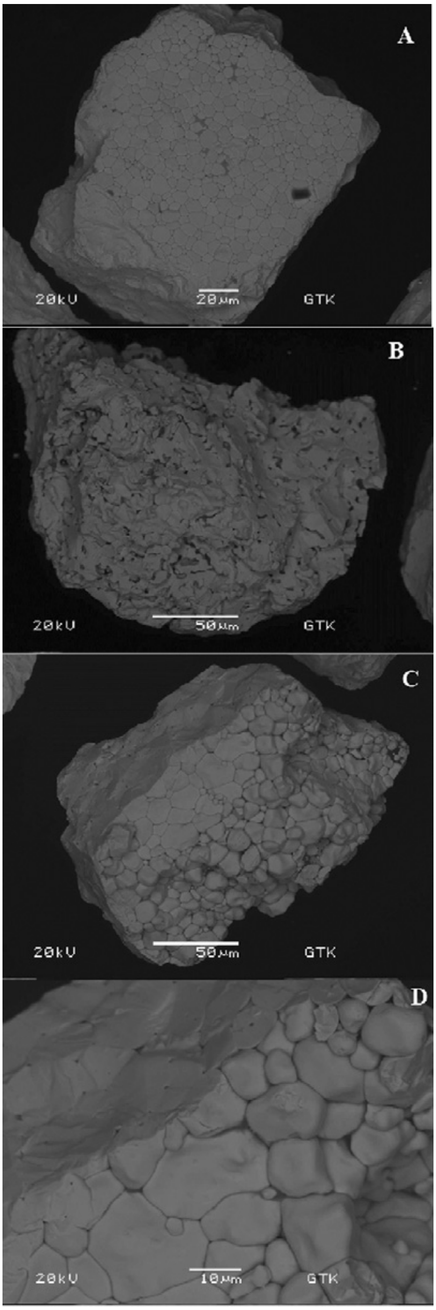

Fig. 10: BSE images of 80 to 160 µm ThO_2 particle after 4 weeks of leaching with 1 M HNO_3 at 80 °C. (A) a leached particle resembling a fresh one, (B) a particle showing deeper dissolution, which has deformed the grain boundaries and formed some cavities into the ThO_2 particle. C and D are taken from this particle, which showed both areas of dissolution and no reaction.

Dissolution experiments were performed to study the effect of carbonate complexation on these ThO_2 samples. It was observed that the solubility and dissolution of ThO_2 increased in the presence of carbonate. The solubilities and dissolution rates of ThO_2 were also dependent on the H^+ activity of the solution. The acidic conditions were found to increase the solubility compared to near-neutral and basic conditions, in which sparingly soluble hydrolysed species of Th were the dissolution-controlling factor. In these experiments the concentration of Th ($\geq 10^{-9}$ mol/L) at pH ≤ 4 was slighly lower than the theoretical solubility of crystalline ThO_2. HR-ICP-MS, with magnetic sector field capability, allowed the analyses of dissolved Th concentrations of sparingly soluble ThO_2 phases down to 10^{-12} mol/L. At higher pH values, from pH 4 to pH 8, the measured concentrations (10^{-10} to 10^{-12} mol/L) were between the theoretical solubility of ThO_2 and $Th(OH)_4$.

Particle size was also found to have an effect on the solubility. The smaller particles with greater surface area seem to have enhancing effect on initial dissolution, and sorption/precipitation reactions. In agreement with recent results [29], it is hypothesized that high energy surface sites may play a role in the relatively rapid initial release of Th observed here. The results of the surface analyses indicated that the initial surface condition may also have some effect on the dissolution processes, with grain boundaries likely playing an important role.

Acknowledgement: This study has been a part of REDUPP project. The research leading to these results has received funding from the European Atomic Energy Community's Seventh Framework Programme (FP7) under grant agreement No. 269903. The high voltage pulse power fragmentation method, Selfrag fragmentation, of the ThO_2 pellets and SEM imaging of the leached particles were carried out at the Finnish Geological Survey (GTK). We thank Jukka Marmo and Marja Lehtonen from GTK for their work and expertise. We thank also Jaana Rantanen and Merja Tanhua-Tyrkkö from VTT. They took part to the Th analyses and data treatment, respectively. We are grateful to Dr. Virginia Oversby and Dr. Lena Z. Evins for invaluable discussion and support throughout the project. We thank Posiva, SKB, VTT for their financial support. CLC acknowledges The University of Sheffield for the award of a Vice Chancellor's fellowship NCH is grateful to the Royal Academy of Engineering and Nuclear Decommissioning Authority for financial support.

References

1. Morss, L. R., Edelstein, N. M., Fuger, J., Katz, J. J.: *The Chemistry of the Actinide and Transactinide Elements*. Springer (2006).
2. Dekoussar, V., Dyck, G. R., Galperin, A., Ganguly, C., Todosow, M., Yamawaki, M.: Thorium fuel cycle – Potential benefits and challenges. IAEA, IAEA-TECDOC-1450, Vienna (2005).
3. Alexander, W. R., McKinley, L. E. (ed.): *Deep Geological Disposal of Radioactive Waste*, Elsevier Series Radioactivity in the Environment, Vol. 9 (2008).
4. Combie, C., Pescatore, C., Smith, P., van Luik, A.: Geological Disposal of Radioactive Waste, Review of Developments in the Last Decade, *OECD Publications*, 2, rue André-Pascal, 75775 PARIS CEDEX 16, France (66 1999 17 1 P) ISBN 92-64-17194-0 – No. 51101 (1999).
5. Vandenborre, J., Abdelouas, A., Grambow, B.: Discrepancies in Thorium Oxide Solubility Values: a new experimental approach to improve understanding of oxide surface solid/solution. Radiochim. Acta **96**, 515–520 (2008).
6. Vandenborre, J., Grambow, B., Abdelouas, A.: Discrepancies in Thorium Oxide Solubility Values: Study of Attachment/Detachment Processes at the Solid/Solution Interface. Inorganic Chem. **49**, No. 19, 8736–8748 (2010).
7. Neck, V., Kim, J.: Solubility and hydrolysis of tetravalent actinides. Radiochim. Acta **89**, No. 1/2001, 1 (2001).
8. Kim, S., Baik, M., Choi, J., Shin, H., Yun, J.: The dissolution of ThO_2(cr) in carbonate solutions and a granitic groundwater. Journal of Radioanalytical and Nuclear Chemistry **286**, No. 1, pp. 91–97 (2010).
9. Fuger, J., Rand, M., Grenthe, I., Neck, V., Rai, D.: *Chemical Thermodynamics of Thorium*, OECD Nuclear Energy Agency (2007).
10. Neck, V., Müller, R., Bouby, M., Altmaier, M., Rothe, J., Denecke, M. A., Kim, J. I.: Solubility of amorphous Th(IV) hydroxide – application of LIBD to determine the solubility product and EXAFS for aqueous speciation. Radiochim. Acta **90**, p. 485 (2002).
11. Neck, V., Altmaier, M., Müller, R., Bauer, A., Fanghänel, Th., Kim, J. I.: Solubility if crystalline thorium dioxide. Radiochim. Acta **91**, 253–262 (2003).
12. Schindler, P. W.: Heterogenous equilibria involving oxides, hydroxides, carbonates and hydroxide carbonates. Adv. Chem. Ser. **67**, 196 (1967).
13. Bundschuh, T., Knopp, R., Müller, R., Kim, J., Neck, V., Fanghänel, T.: Application of LIBD to the determination of the solubility product of thorium(IV)-colloids. Radiochim. Acta **88**, No. 9-11/2000, p. 625 (2000).
14. Rothe, J., Denecke, M., Neck, V., Müller, R., Kim, J.: XAFS investigation of the structure of aqueous thorium(IV) species, colloids, and solid thorium(IV) oxide/hydroxide. Inorganic Chemistry **41**, No. 2, pp. 249–258 (2002).
15. Bitea, C., Müller, R., Neck, V., Walther, C., Kim, J.: Study of the generation and stability of thorium(IV) colloids by LIBD combined with ultrafiltration. Colloids and Surfaces A: Physicochemical and Engineering Aspects **217**, No. 1, pp. 63–70 (2003).
16. Altmaier, M., Neck, V., Fanghänel, T.: Solubility and colloid formation of Th(IV) in concentrated NaCl and $MgCl_2$ solution. Radiochimica Acta **92**, 537–543 (2004).
17. Walther, C., Fuss, M., Buchner, S.: Formation and hydrolysis of polynuclear Th(IV) complexes- a nano-electrospray mass-spectrometry study. Radiochim. Acta **96**, 411–426 (2008).
18. Hubert, S., Barthelet, K., Fourest, B., Lagarde, G., Dacheux, N., Baglan, N.: Influence of the precursor and the calcination temperature on the dissolution of thorium dioxide. Journal of Nuclear Materials **297**, No. 2, pp. 206–213 (2001).
19. Forsyth, R.: Fuel rod D07/B15 from Ringhals 2 PWR: Source material for corrosion/leach tests in groundwater. Fuel rod/pellet characterisation program part 1. SKB technical report 87-02 (1987).
20. Forsyth, R.: Spent nuclear fuel. A review of properties of possible relevance to corrosion processes. SKB technical report 95-23 (1995).
21. Stennett, M. C., Corkhill, C. L., Marshall, L. A., Hyatt, N. C.: J. Nucl. Mater. **432**, 182 (2013).
22. Andres, U., Timoshkin, I., Jirestig, J.: Liberation of minerals by high-voltage electrical pulses. Powder Technology **104**, 37–49 (1999).
23. Bluhm, H., Frey, W., Giese, H., Hoppe, P., Schultheiß, C., Straßner, R.: Application of Pulsed HV Discharges to Material Fragmentation and Recycling. IEEE Trans. On Dielectrics and Electrical Insulation **7**, No. 5 (2000).
24. Rozalén, M. L., Huertas, F. J., Brady, P. V., Cama, J., García-Palma, S., Linares, J.: Experimental study of the effect of pH on the kinetics of montmorillonite dissolution at $25\,^{\circ}\mathrm{C}$. Geochim. Cosmochim. Acta **72**(17), 4224–4253 (2008).
25. Malmström, M., Banwart, S., Lewenhagen, J., Duro, L., Bruno, J.: The dissolution of biotite and chlorite at $25\,^{\circ}\mathrm{C}$ in the near-neutral pH region. Journal of Contaminant Hydrology **21**(1–4), 201–213 (1996).
26. Brady, P., Walther, J. V.: Kinetics of quartz dissolution at low temperatures. Chemical Geology **82**, 253–264 (1990).
27. Brantley, S. L.: *Kinetics of Mineral Dissolution*. Brantley, S. L., Kubicki, J. D., White, A. F. (Eds.), Kinetics of Water–Rock Interaction, Springer-Kluwer, New York (2008).
28. Weast, R. C. (ed): *CRC Handbook of Chemistry and Physics*, 53rd Edition, The Chemical Rubber Co. Cleveland, Ohio, USA (1972).
29. Corkhill, C., Myllykylä, E., Bailey, D., Thornber, S., Qi, J., Maldonado, P., Stennett, M., Hamilton, A., Hyatt, N.: The contribution of energetically reactive surface features to the dissolution of $\mathrm{CeO_2}$ and $\mathrm{ThO_2}$ analogues for spent nuclear fuel, submitted to ACS Applied Materials and Interfaces. Manuscript ID: am-2014-018978.
30. Zetterström Evins, L., Vähänen, M. (eds.): REDUPP First Annual Report, Posiva Oy, Olkiluoto, Finland, Posiva Working Report 2012-28, 44 p. (2012).
31. Rai, D., Felmy, A. R., Moore, D. A., Mason, M. J.: The solubility of Th(IV) and U(IV) hydrous oxides in concentrated $\mathrm{NaHCO_3}$ and Na_2CO_3 solutions. In: Scientific Basis for Nuclear Waste Management XVIII, Part 2, T. Murakami and, R. C. Ewing (eds.), pp. 1143–1150, Materials Research Society Symposium Proceedings, Volume 353, Materials Research Society, Pittsburgh, Pennsylvania (1995).
32. Ötshols, E., Bruno, J., Grenthe, I.: The solubility of microcrystalline $\mathrm{ThO_2}$ in CO-H_2O media. Geochim. Cosmochim. Acta. **58**, No. 2, pp. 613–623 (1994).

PUBLICATION II

Contribution of Energetically Reactive Surface Features to the Dissolution of CeO_2 and ThO_2 Analogues for Spent Nuclear Fuel Microstructures

In: ACS Appl. Mater. Interfaces 2014; 6, 12279-12289

dx.doi.org/10.1021/am5018978

ACS APPLIED MATERIALS & INTERFACES
Research Article
www.acsami.org

Contribution of Energetically Reactive Surface Features to the Dissolution of CeO_2 and ThO_2 Analogues for Spent Nuclear Fuel Microstructures

Claire L. Corkhill,*[†] Emmi Myllykylä,[‡] Daniel J. Bailey,[†] Stephanie M. Thornber,[†] Jiahui Qi,[§] Pablo Maldonado,[∥] Martin C. Stennett,[†] Andrea Hamilton,[⊥] and Neil C. Hyatt*[†]

[†] Immobilisation Science Laboratory, Department of Materials Science and Engineering, The University of Sheffield, Sheffield S1 3JD, United Kingdom

[‡] VTT Technical Research Centre of Finland, Espoo FI-02044, Finland

[§] Royal School of Mines, Imperial College London, London SW7 2AZ, United Kingdom

[∥] Department of Physics and Astronomy, Uppsala Universitet, 751 05 Uppsala, Sweden

[⊥] Department of Civil and Environmental Engineering, The University of Strathclyde, Glasgow G1 1XQ, United Kingdom

ABSTRACT: In the safety case for the geological disposal of nuclear waste, the release of radioactivity from the repository is controlled by the dissolution of the spent fuel in groundwater. There remain several uncertainties associated with understanding spent fuel dissolution, including the contribution of energetically reactive surface sites to the dissolution rate. In this study, we investigate how surface features influence the dissolution rate of synthetic CeO_2 and ThO_2, spent nuclear fuel analogues that approximate as closely as possible the microstructure characteristics of fuel-grade UO_2 but are not sensitive to changes in oxidation state of the cation. The morphology of grain boundaries (natural features) and surface facets (specimen preparation-induced features) was investigated during dissolution. The effects of surface polishing on dissolution rate were also investigated. We show that preferential dissolution occurs at grain boundaries, resulting in grain boundary decohesion and enhanced dissolution rates. A strong crystallographic control was exerted, with high misorientation angle grain boundaries retreating more rapidly than those with low misorientation angles, which may be due to the accommodation of defects in the grain boundary structure. The data from these simplified analogue systems support the hypothesis that grain boundaries play a role in the so-called "instant release fraction" of spent fuel, and should be carefully considered, in conjunction with other chemical effects, in safety performance assessements for the geological disposal of spent fuel. Surface facets formed during the sample annealing process also exhibited a strong crystallographic control and were found to dissolve rapidly on initial contact with dissolution medium. Defects and strain induced during sample polishing caused an overestimation of the dissolution rate, by up to 3 orders of magnitude.

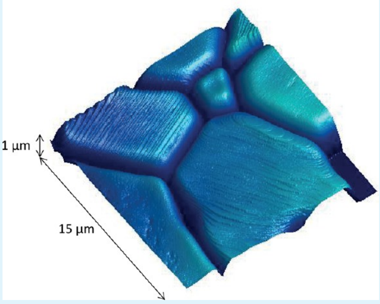

KEYWORDS: *nuclear fuel, dissolution, grain boundaries, faceting, surface, atomic force microscopy*

1. INTRODUCTION

Spent nuclear fuel is a heterogeneous material composed primarily of UO_2, with a minor component of actinides (e.g., Np and Pu) and fission products (e.g., Sr, Cs, and I). The preferred route for disposal of this material is within a geological disposal facility, several hundreds of meters below the ground. In such an environment, the release of radionuclides to the geo- and biospheres is controlled by the dissolution of the spent fuel in groundwater; thus it is important to understand the mechanisms and kinetics of dissolution. The dissolution behavior of spent fuel is dominated by the behavior of the UO_2 matrix, and, as such, a simplified system comprising UO_2 only is often used in experiments to determine SNF dissolution. On the basis of a wide range of dissolution investigations of SNF and UO_2 (see reviews[1,2]), it has been estimated that the fractional dissolution rate of spent nuclear fuel is in the range of 10^{-6} to 10^{-8} per year, indicating that complete dissolution is likely to occur within ~10 million years.[3] However, natural uraninite (UO_2) ores are known to be stable in the earth under reducing conditions for periods of billions of years,[4,5] suggesting that laboratory experiments may overestimate the dissolution rate of UO_2 by more than 2 orders of magnitude.

It has been demonstrated that experimentally derived dissolution rates of other minerals, such as quartz and feldspar, are also often found to be higher than the corresponding weathering rate of the rocks they comprise.[6−9] One of the causes of this observed behavior is specimen preparation within

Received: March 28, 2014
Accepted: July 7, 2014
Published: July 7, 2014

the laboratory; the act of crushing generates sharp edges and other surface defects, and the atoms on the surface associated with these features have high surface energy and contain fewer chemical bonds than the atoms on defect-free surfaces, which, in turn, contain fewer chemical bonds than atoms within the bulk. Defect surfaces are removed during dissolution, leaving a lower energy surface that dissolves at a slower rate.[10,11] Knauss and Wolery[6] observed that the dissolution rate of crushed albite decreased during the first 20 days by over an order of magnitude in all experimental conditions. Similarly, during sequential leaching from 52 to 114 days, crushed UO_2 samples showed progressively decreasing dissolution rates.[12,13] Natural defects present at the surface have also been shown to affect dissolution rates; for example, Claparede et al.[14] found that crystal defects and initial crystallite size of mixed cerium−neodymium oxides influenced the dissolution rate.

To evidence the influence of high energy surface features on the dissolution rate of UO_2, CeO_2 and ThO_2 analogues are investigated. These materials were chosen because they are isostructural to UO_2 but are not sensitive to changes in oxidation state of the cation. Previously, we have synthesized CeO_2 and ThO_2 to closely resemble the microstructure of SNF;[15,16] therefore, we also make an assessment of how these physical and structural features are likely to influence the dissolution of SNF. Using an integrated approach, applying atomic force microscopy, vertical scanning interferometry, electron backscatter diffraction, and aqueous geochemical analysis, we determine how natural and specimen-induced high-energy surface sites (grain boundaries and surface defects, respectively) contribute to measured laboratory dissolution rates. Through this methodology, we aim to reduce the uncertainties associated with UO_2 dissolution, and thus improve our understanding of the relationship between laboratory studies and the dissolution rates to be expected under geological disposal conditions.

2. EXPERIMENTAL SECTION

2.1. CeO_2 and ThO_2 Preparation. Cerium dioxide monoliths were prepared according to Stennett et al.[15] Monoliths were ground and polished to a 0.05 μm finish using SiC paper and diamond paste. To develop a grain boundary structure at the surface of some of the monoliths, thermal annealing was conducted. Monoliths were heated to 1500 °C at a ramp rate of 5 °C min^{-1} and held for 1 min to develop a grain boundary texture. The final microstructure (equiaxed grains ranging in size from 10 to 30 μm and randomly orientated) was in good agreement with those published for UO_2 and SIMFUEL.[17,18] An area was masked with an inert glue to act as a nonreactive reference surface of constant height during the dissolution experiments.

ThO_2 powder (British Drug Houses Ltd., lot number G83757/541012) was used to prepare sintered ThO_2 monoliths. Briefly, 1 g of powder was uniaxially pressed in a 10 mm diameter hardened stainless steel die with a load of 100 MPa. Monoliths were sintered for 4 h at 1750 °C in a standard air atmosphere muffle furnace, at a ramp rate of 5 °C min^{-1}, which gave a final density of >94% of the theoretical density of ThO_2 (10.00 g m^{-3}), determined using the Archimedes method. Monoliths were ground and polished to a 0.25 μm finish using SiC paper and diamond paste. It was found that a final polishing step using a 0.06 μm silica colloid solution was required to obtain surfaces flat enough for analysis by electron back scatter diffraction (EBSD)[19] and by atomic force microscopy (AFM) (for ThO_2, only data, not images, are given in the text due to complexities associated with surface polishing). Grain boundaries were defined by heating to 1500 °C at a ramp rate of 5 °C min^{-1}. The resulting grains ranged in size from 5−30 μm, and grains were found to be randomly orientated, consistent with UO_2 and SIMFUEL microstructure.

2.2. Dissolution Experiments. CeO_2 and ThO_2 are insoluble materials; hence, they are difficult to dissolve without the application of aggressive conditions. As such, dissolution was performed at high temperature (90 and 150 °C) and in acidic media. All solutions were prepared using ultrahigh quality (UHQ) water (18 MΩ). The following dissolution experiments were conducted: (1) annealed CeO_2 and ThO_2 dissolution at 90 °C in 0.01 M HNO_3; (2) annealed CeO_2 dissolution at 150 °C in 0.01 M HNO_3; (3) annealed CeO_2 dissolution at room temperature in 0.01, 0.1, 1.5, 3, and 15 M HNO_3; (4) annealed CeO_2 dissolution at room temperature in a series of etching solutions (72 h in UHQ water, 15 h in 0.001 M HCl, 4 h in 0.01 M HCl); and (5) polished (i.e., not annealed to define grain texture) CeO_2 dissolution at 90 and 150 °C in 0.01 M HNO_3.

Dissolution experiments performed at 90 °C were conducted within 50 mL PTFE vessels, cleaned according to the ASTM PCT standard.[20] A single monolith of CeO_2 or ThO_2 was placed into a PTFE basket within the vessel, to allow contact of the whole monolith with the dissolution medium, and 40 mL of 0.01 M HNO_3 was added. Triplicate samples and duplicate blanks (containing no monolith) were placed in a Carbolite oven at 90 (±0.5) °C and sampled at 0, 1, 3, 7, 14, 21, 28, and 35 days. An aliquot (1.2 mL) of each sample was removed for aqueous elemental analysis. One monolith from each triplicate experiment was removed for surface characterization at each sampling point, and returned to the dissolution medium after analysis. Dissolution experiments performed at 150 °C were conducted in customized reactors, consisting of 3 mL PTFE inserts with a PTFE lid (cleaned as above), within a sealed steel pressure vessel. These were placed within a heating block, where the temperature was maintained at 150 (±1) °C. Monoliths were placed on PTFE inserts to ensure contact of the whole monolith with the dissolution medium, and 2 mL of 0.01 M HNO_3 was added. Experiments were destructively sampled at 1, 3, 7, 21, and 35 days, at which times the monoliths were subject to surface analysis and aqueous solutions were collected for elemental analysis. Dissolution experiments conducted at room temperature were performed within an atomic force microscopy (AFM) fluid cell containing a fragment of a CeO_2 monolith cut using a diamond slow saw, immersed within 3 mL of reaction medium.

2.3. Surface and Aqueous Analysis. Monolith surfaces and cross sections were imaged using a JEOL JSM6400 scanning electron microscope (SEM) operating with an accelerating voltage of 15 kV and a working distance of 18 mm. Analysis of crystallographic orientation was performed using electron backscatter diffraction (EBSD) (Oxford Instruments, Abingdon, Oxfordshire, UK) in conjunction with an FEI Sirion field emission SEM. EBSD maps of 100 μm^2 were obtained at an accelerating voltage of 20 kV and with a 0.25 μm step size, and analyzed using HKL Channel 5 software (Oxford Instruments). Surface topography was measured using vertical scanning interferometry (VSI) (Sensofar PLu2300 profilometer) using a confocal lens with 50× and 150× magnification, a numerical aperture of 0.95, and lateral and vertical resolutions of 111 and 1 nm, respectively. Changes in surface morphology during dissolution were also measured using atomic force microscopy (AFM); ex situ measurements were performed using a Veeco Dimension 3100 microscope, operating in tapping mode and using high aspect ratio AFM tips, and in situ measurements were conducted using a Digital Instruments Multimode/Nanoscope IIIa in contact mode. Aqueous elemental analysis of Ce was undertaken by inductively coupled plasma-mass spectroscopy (ICP-MS) using an Aglient 4500 spectrometer, and analysis of Th was performed using high-resolution ICP-MS (Element 2, ThermoScientific). Prior to analyses, all samples were acidified with 20 μL of concentrated HNO_3 to keep all elements dissolved in solution. Solution data are expressed as the normalized elemental leaching N_L(Ce, Th) (g m^{-2}) according to

$$N_L(\mathrm{Ce,\ Th}) = \frac{m_{\mathrm{Ce,Th}}}{S/V} \qquad (1)$$

where $m_{\mathrm{Ce,\ Th}}$ is the total amount of Ce or Th released into solution and S/V is the surface area to volume ratio. The normalized element leaching rate R_L(Ce, Th) (g m^{-2} d^{-1}) is determined by

$$R_L(\mathrm{Ce,\ Th}) = \frac{m_{\mathrm{Ce,Th}}}{\frac{S}{V} \times \Delta t} \qquad (2)$$

where Δt is the leaching time in days.

3. RESULTS

Table 1. Dissolution Rates for CeO_2 and ThO_2 Samples Dissolved in 0.01 M HNO_3 as a Function of Specimen Preparation and Temperature[a]

specimen preparation	temp (°C)	rate (g m^{-2} d^{-1})
annealed CeO_2	90	$(7.26 \pm 0.2) \times 10^{-5}$
	150	$(6.34 \pm 0.1) \times 10^{-3}$
annealed ThO_2	90	$(5.23 \pm 0.1) \times 10^{-7}$
polished CeO_2	90	$(7.40 \pm 0.2) \times 10^{-2}$
	150	$(7.01 \pm 0.2) \times 10^{-2}$

[a] Errors given are the standard deviation of triplicate experiments.

3.1. CeO_2 and ThO_2 Dissolution Rate. The aqueous dissolution rate data derived from all experiments are given in Table 1. The dissolution rate for CeO_2 dissolved at 150 °C was $(6.34 \pm 0.1) \times 10^{-3}$ g m^{-2} d^{-1}; data are shown in Figure 1a. The initial dissolution rates, between 0 and 7 days, appeared to be more rapid than those between 7 and 35 days (Figure 1a), which may be due to solution saturation effects. Under the same dissolution conditions, but at 90 °C, the dissolution rate was significantly lower, at $(7.26 \pm 0.2) \times 10^{-5}$ g m^{-2} d^{-1}, but the same trend was found, with an initial, rapid dissolution followed by a slower dissolution from 7 to 35 days (Figure 1b, Table 1). Dissolution of ThO_2 exhibited behavior different from that of CeO_2, as shown in Figure 1c. At 90 °C, the dissolution was initially rapid (between 0 and 7 days, Figure 1c) at a rate of $(6.71 \pm 0.5) \times 10^{-5}$ g m^{-2} d^{-1}, but subsequently the dissolution rate significantly decreased, giving an overall rate between 0 and 28 days of $(5.23 \pm 0.1) \times 10^{-7}$ g m^{-2} d^{-1} (Table 1). Rapid dissolution could result from the release of material from high energy surface sites at the ThO_2 surface, leading to saturation of the solution with respect to Th, to a point at which amorphous $ThO_x(OH)_y \cdot H_2O$ or even polynuclear $Th_x(OH)_y$ species form. These amorphous phases are known to be capable of recrystallizing; for example, Rai et al.[21] showed that $ThO_{2(am)}$ converted to crystalline $ThO_{2(cr)}$ upon heating at 90 °C in acidic solution. Therefore, recrystallized ThO_2 may be able to form a protective layer on the surface of ThO_2, providing a barrier to further dissolution and giving rise to the dissolution behavior observed in Figure 1c.

3.2. Grain Boundaries. Grain boundaries are a well-known feature of SNF; they typically contain volatile fission products (e.g., Cs and I) and alloy particles of Mo, Tc, Ru, Rh, and Pd.[22] The presence of these highly radioactive elements necessitates a careful understanding of how grain boundaries behave during dissolution, and an evaluation of their contribution to the dissolution rate of spent fuel. Figure 2 shows the typical microstructure obtained for CeO_2; annealing conditions were optimized to give grain boundary depths of <1 μm.

The contribution of grain boundary dissolution to the overall dissolution rate of CeO_2 and ThO_2 was investigated in 0.01 M HNO_3 at 90 °C, and also at 150 °C for CeO_2. Figure 3 shows VSI images of CeO_2 before dissolution (Figure 3a) and after 3 and 7 days of dissolution at 150 °C (Figure 3b and c, respectively). It was found that after 3 days, dissolution was focused at grain boundaries and the pores between grains (Figure 3b). After 7 days, grain boundaries were preferentially dissolved, up to a depth of at least 0.70 μm, and the surface of the grains became rough and pitted (Figure 3c). Some of the grains dissolved at different rates, as evidenced by the height contrast in different grains (Figure 3b,c). In their analysis of CaF_2 dissolution (isostructural to CeO_2, ThO_2, and UO_2), Godinho et al.[23] showed that the measured retreat rates of CaF_2 grains depended upon the crystallographic orientation of the exposed planes. They concluded that the {111} plane is the most stable and dissolved most slowly, while the {112} plane was the least stable, dissolving up to 33 times faster than {111}. First-principles calculations have shown that the surface stability of CeO_2 from the most to the least stable plane is in the order of {111} > {110} > {100},[24,25] although it should be noted that the {100} plane in such calculations is modeled and not real, due to the difficulties associated with modeling the dipolar {100} plane. The results presented here are in

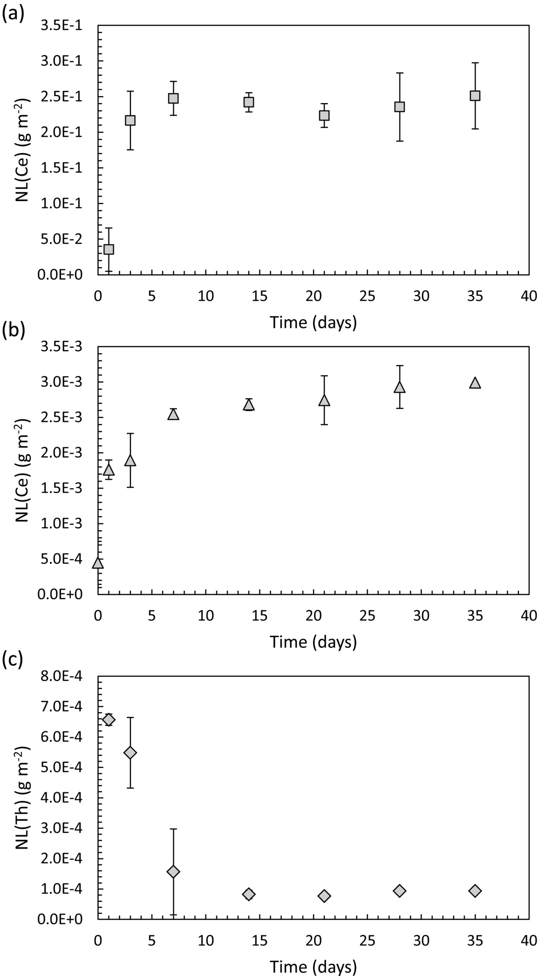

Figure 1. Normalized mass loss data for CeO_2 and ThO_2 dissolved in 0.01 M HNO_3: (a) annealed CeO_2 at 150 °C; (b) annealed CeO_2 at 90 °C; and (c) annealed ThO_2 at 90 °C. Errors given are the standard deviation of triplicate experiments. Corresponding dissolution rates are shown in Table 1.

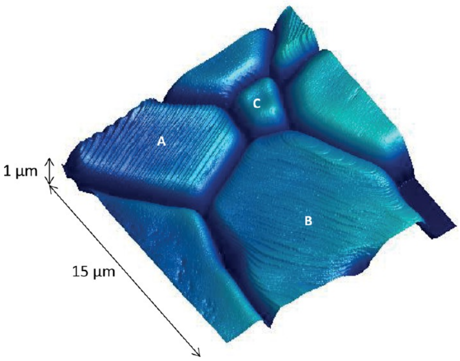

Figure 2. AFM image of CeO_2 surface, showing grains, grain boundaries, pores, and facets. The labels A, B, and C correspond to detailed analysis of grain facets, where A shows facets generated through the intersection of $\{665\}/\{\bar{1}11\}$ planes, B shows facets generated through the intersection of $\{111\}/\{\bar{1}11\}$ planes, and C shows no facets.

agreement with these findings; EBSD analysis of the grains in Figure 3c showed that the most stable grain had a (111) surface.

Figure 3d shows an SEM image of CeO_2 after 21 days of dissolution. The grains became entirely detached from the surface and were considerably smaller than their original size prior to dissolution (∼5 µm, as compared to an initial size of 10−30 µm). The images in Figure 3 indicate that dissolution occurs preferentially along the grain boundaries, such that intergranular bonding becomes weakened with ongoing dissolution, eventually resulting in grain boundary decohesion. It is notable that the detached grains in Figure 3d exhibit triangular facets, indicative of {111} plane terminations, suggesting that surfaces that dissolve more slowly are the most stable, and persist during dissolution. Evidence for grain boundary decohesion in CeO_2 under these dissolution conditions was confirmed by SEM analysis of monoliths in cross section, with the surface of the grain just above the field of view. Figure 4a shows the cross section of a pristine, annealed sample of CeO_2. Grain boundaries were not observed in the top ∼60 µm of the cross section. Monoliths of CeO_2 that experienced dissolution for several durations are shown in Figure 4b−d. After 7 days, grains and grain boundaries were clearly visible (Figure 4b), and after 14 days entire grains appeared to become separated from one another (Figure 4c). After 21 days of dissolution, the grains appeared to decrease considerably in size to ∼5 µm, in agreement with the surface topography shown in Figure 3d; close inspection revealed that the grains were, in fact, fractured between pores, giving rise to apparently smaller grains. These data confirm that grain boundary dissolution in CeO_2 is extensive, and that grain boundaries may act as conduits for solution ingress, leading to dissolution and fracturing between pores. This process is expected to contribute substantially to the overall dissolution rate.

Analysis of the CeO_2 sample used to provide solution data at 90 °C, shown in Figure 1b, was performed using AFM and EBSD. Figure 5 shows the boundaries between several grains of different crystallographic orientation, including grain boundary “A” between surfaces of (025) and (001), and grain boundary “B” between surfaces of (001) and (356). EBSD analysis of these boundaries gave mean misorientation angles of 36.01° and 59.84°, respectively (Table 2). The dissolution of these boundaries was monitored over a period of 7 days (after which the surface became too rough to accurately measure) with reference to an inert surface mask of constant height. The mean surface retreat rates were measured as 0.001, 0.032, and 5.954 nm d^{-1} for the (025), (001), and (365) surfaces, respectively, indicating surface stability in the order: (025) < (001) < (365).

The retreat rates of CeO_2 grain boundaries were greater than the surface retreat rates between 0 and 1 days, and the retreat rate was different in different grain boundaries. Between 0 and 1 days of dissolution, the measured retreat of grain boundary A was 0.13 µm on the (025) aspect and 0.04 µm on the (001) aspect (Figure 5). Grain boundary B retreated more rapidly, increasing in depth by 0.21 µm on the (001) aspect, and 0.07

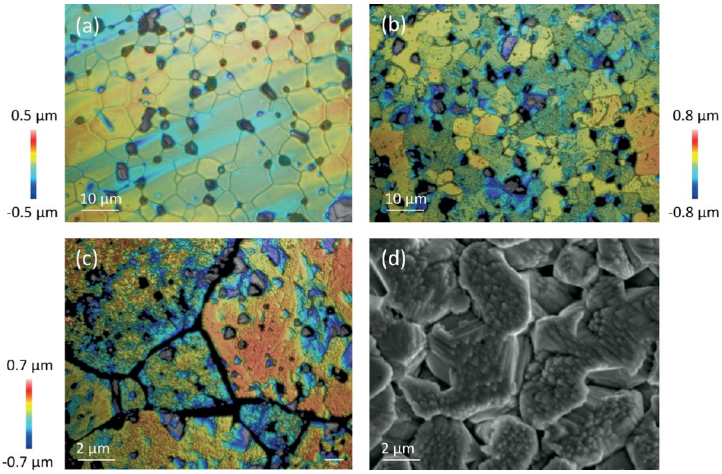

Figure 3. Vertical scanning interferometer and SEM images of CeO_2 surfaces (a) prior to dissolution and following dissolution for (b) 3 days, (c) 7 days, and (d) 21 days in 0.01 M HNO_3 at 150 °C.

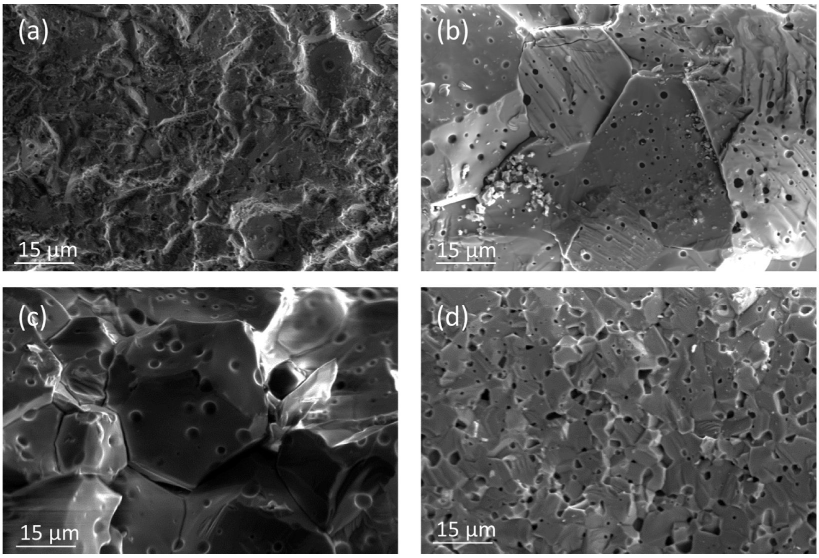

Figure 4. SEM images of cross sections through CeO_2, with the surface of the sample just above the top of each image: (a) nondissolved, annealed CeO_2; and CeO_2 dissolved in 0.01 M HNO_3 at 150 °C for (b) 7 days, (c) 14 days, and (d) 21 days.

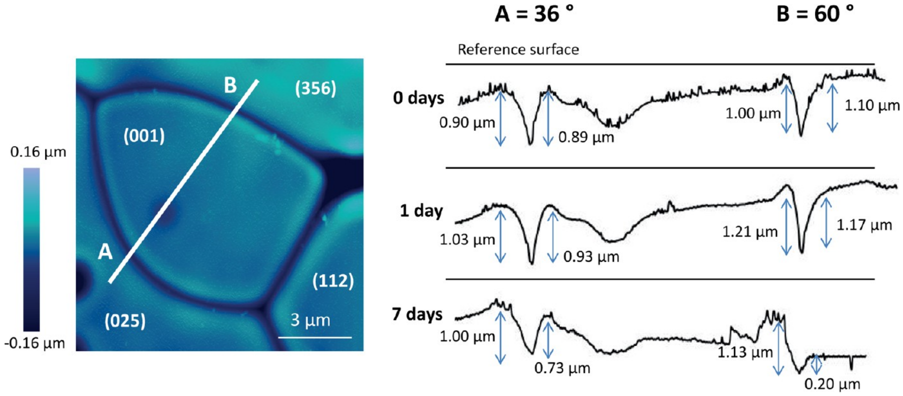

Figure 5. Atomic force microscopy image and cross sections of CeO_2 grains, with grain boundaries of low (A) and high (B) misorientation angles. Grain surfaces are measured against an inert reference surface of constant height. Cross sections show change in depth of the grain boundaries and grain surfaces with time, during dissolution at 90 °C in 0.01 M HNO_3.

Table 2. Grain Boundary Depths of CeO_2 (Corresponding to Figure 5) and ThO_2 Grains with Different Grain Orientations and Grain Boundary Misorientation Angles, as a Function of Time during Dissolution in 0.01 M HNO_3 at 90 °C

			grain boundary depth (μm)			
analogue composition	grain orientations	grain boundary misorientation angle (deg) (±0.01)	0 days (±0.01)	1 day (±0.01)	7 days (±0.01)	grain boundary retreat rate (μm d^{-1}) (±0.001)
CeO_2	(025)/(001)	36.01	0.90	1.03	1.00	0.014
	(001)/(356)	59.84	1.01	1.21	1.13	0.017
ThO_2	(103)/(506)	23.91	0.04	0.05	0.09	0.007
	(103)/(014)	39.33	0.06	0.14	0.15	0.012
	(416)/(506)	56.05	0.07	0.12	0.17	0.357

μm on the (356) aspect (Figure 5). Grain boundaries became deeper during dissolution, suggesting the removal of material from within. Furthermore, the dissolution was greatest for the high misorientation angle boundary, as compared to the low misorientation angle grain boundary, giving grain boundary retreat rates of 0.017 and 0.014 μm d^{-1}, respectively (Table 2). After 7 days of dissolution, grain boundaries appeared to become shallower as a result of enhanced grain surface retreat at this time, especially for grain boundary B where the (356) surface dissolved very rapidly (Figure 5). In summary, when

CeO_2 samples were contacted with the dissolution medium, a rapid loss of material from grain boundaries occurred, which is in agreement with the enhanced release of Ce into solution during this time (Figure 1a). Subsequently, surface retreat rates increased, and the surface, or matrix, dissolution became the dominant dissolution mechanism. Comparison to the aqueous Ce concentrations in Figure 1a shows that the dissolution was less rapid after 7 days, confirming that grain boundary dissolution contributes significantly to the initial dissolution rate, while surface controlled dissolution leads to slower dissolution rates.

Similar experiments were conducted to monitor the dissolution of ThO_2 grain boundaries as a function of crystallographic orientation and grain boundary misorientation using AFM and EBSD (Table 2). The dissolution behavior of ThO_2 grain boundaries at 90 °C in 0.01 M HNO_3 was comparable to that of CeO_2, whereby grain boundaries preferentially dissolved and boundaries with high misorientation angles retreated more rapidly than those with low misorientation angles. For example, a grain boundary between two grains with (103) and (506) surfaces had a misorientation angle of 23.91° and a retreat rate of 0.007 μm d^{-1}, while another grain boundary formed between grains with (416) and (506) surfaces with a mean misorientation angle of 56.05° gave a retreat rate of 0.357 μm d^{-1}, more than twice that of the lower misorientation angle grain boundary (Table 2). It should be noted that after 7 days of dissolution it was no longer possible to measure grain boundaries in ThO_2 due to the presence of a surface layer, giving further evidence to the hypothesis discussed above, that a dissolution rate drop after 7 days (Figure 1c) is due to the formation of a protective layer that results from the transformation of amorphous $ThO_x(OH)_y\cdot H_2O$ to $ThO_{2(cr)}$ precipitates.

3.3. Surface Facets. Surface facets comprising flat terraces separated by inclined steps were found on annealed grains of CeO_2 (Figure 2). These features were not observed on ThO_2 because of its increased surface roughness, produced by difficulties encountered in polishing the sample. EBSD analysis of these grains was not possible due to multiple orientations arising from the faceted surfaces; however, alternative geometric measurements were used to determine the orientation of the facet features. By measuring the angle, θ, between the facet and the surface, the best combination of planes can be found according to Maldonado et al.:[25]

$$\theta = \arccos\left(\frac{\vec{u}\cdot\vec{v}}{|\vec{u}||\vec{v}|}\right) \tag{3}$$

where $\vec{u}$ and $\vec{v}$ are the normal vectors that define the planes. Godinho et al.[23] showed that a dissolution surface is only made of the most stable planes, as the less stable ones are more prone to dissolution. Therefore, if we assume only the most stable planes are present at the surface, this method allows the unambiguous definition of the intersection of two distinct planes. Figure 6 illustrates this concept, showing the lateral view of a hypothetical surface comprised of two planes. These planes are the {111} and {100} planes, which intersect forming a facet with an angle θ = 70.52°/109.48°.

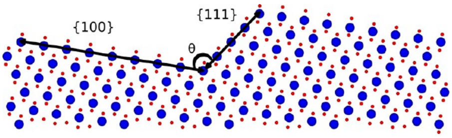

Figure 6. Lateral view of a hypothetical CeO_2 surface (large blue dots are O, small red dots are Ce), composed of the {100} and {111} surfaces, intersecting at an angle, θ, of 70.52°/109.48° (rendered by VESTA).

Several different planar orientations of surface facets were observed. Grain "A" in Figure 2 exhibited regularly stepped facets across the surface of the grain, while grain "B" developed facets that increased in height from the center of the grain to the edge. According to den Brok and Morel,[26] these ridge and valley features result from elastic strain released during annealing, lowering the surface energy. Some grains, for example, grain "C" (Figure 2), showed no facets. The facets on grain "A" enclosed an angle of 106.83 ± 2.1°, indicative of a $\{665\}/\{\bar{1}11\}$ plane intersection, which is known to have an angle of 107.04°. The height of these facets ranged from 4.66 to 16.71 nm, and the flat terraces between facets were consistently separated by distances of 5.74 nm. The facets on grain "B" (Figure 2) had planar orientations that met at an angle of 110.33 ± 1.6°, indicative of a $\{111\}/\{\bar{1}11\}$ facet orientation, which has a known angle of 109.47°. These facets ranged in height from 1.50 to 6.61 nm and had flat terraces of 24.06 nm (or multiples thereof). These $\{111\}/\{\bar{1}11\}$ facets were themselves faceted, giving rise to a "zigzag" edge, as shown in Figure 7a. These "mini-facets" were found to be perpendicular to the $\{\bar{1}11\}$ plane, suggestive of the plane {511}. The facet structures were also observed to extend into the grain boundaries (Figure 7b). Figure 7b−e shows detailed AFM images of another grain, which exhibited a ridge and valley-like morphology, with stacked concentric facets, building ridges at the grain edges (giving rise to the "tooth-shaped" grains shown in AFM profiles in Figure 5) and flat valleys in the center of the grain. The difference in height between the ridges and valleys for this grain was up to 150.36 nm. The facet heights ranged from 2.50 to 58.04 nm, were unevenly spaced at distances <20.02 nm, and enclosed an angle 125.43 ± 0.7°. This is indicative of a {111}/{100} planar orientation, which has a known angle of 125.26°. It can be noted that all of the facets found at the surface of CeO_2 involve the most stable plane, {111}.

To understand the dissolution of the CeO_2 surface facets, samples were subjected to high acidity (pH <2) dissolution experiments. The surface shown in Figure 7b−e was subject to dissolution at room temperature in increasing concentrations of nitric acid, representing increasingly aggressive dissolution conditions. The resulting facet height measurements, corresponding to the facets between point 1 and point 8, shown in Figure 7e, are given in Table 3. It is clear that the addition of just 0.01 M HNO_3 resulted in a significant increase in height for most facets, as compared to the height prior to dissolution. Facet height increases ranged between 1.30 and 3.91 nm. Two facets were observed to become shallower (facets 2 and 5, Table 3). With increasing acidity between 0.1 and 3 M HNO_3, facet height change was variable, with some facets showing little change (Table 3), while others decreased in height and others increased (suggesting addition of material to facets). This variability suggests that these surface sites are highly dynamic, changing in response to the reaction medium, but with little observable trend. However, it is clear that upon initial immersion in the reaction medium, instantaneous dissolution of the facets occurred.

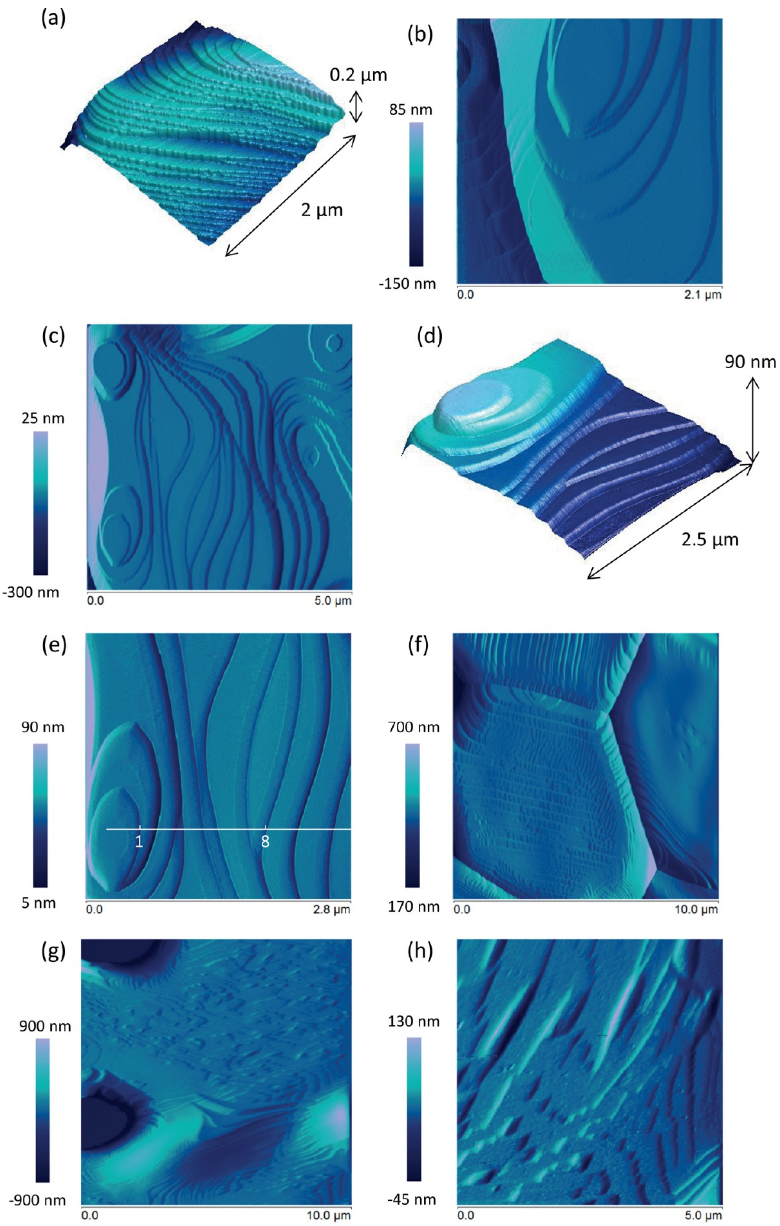

Figure 7. Atomic force microscopy images depicting surface features of CeO_2 spent nuclear fuel analogue surfaces: (a) showing $\{\bar{2}11\}$ microfacets perpendicular to the plane $\{\bar{1}11\}$; (b) facet structures extending into grain boundaries; (c) ridge and valley structure formed by intersecting {111}/{100} planes; (d and e) intersecting {111}/{100} planes showing cross section for step height measurements in Table 3; (f) $\{\bar{2}11\}/\{\bar{1}11\}$ surface facets following dissolution in 15 M nitric acid at room temperature; and (g and h) etch pattern formed on previously smooth grains following etching in a series of media (UHQ water for 72 h, 0.001 M for 15 h, and 0.01 M HCl for 4 h) at room temperature. Images (a), (g), and (h) were taken in air, and all remaining images were taken in solution.

To investigate the effect of dissolution on the {511} microfacets perpendicular to the $\{\bar{1}11\}$ plane (grain "B", Figure 2 and Figure 7a), a grain with these features was subject to dissolution in a 15 M HNO_3 solution at room temperature. The resulting surface is shown in Figure 7f. The effect of dissolution was increased microfacetting in the {511} plane. Even under these aggressive conditions, it was not possible to see any change in the smooth grains; therefore, the samples were etched in a series of media for a prolonged period (72 h in UHQ water, 15 h in 0.001 M HCl, and 4 h in 0.01 M HCl) at room temperature. The resulting AFM images show that the smooth grain became highly etched, forming "zigzag" features

Table 3. Facet Heights Measured from Figure 7e as a Function of HNO_3 Molarity

nitric acid concn (M)	facet height (nm) (±0.01)							
	facet 1	facet 2	facet 3	facet 4	facet 5	facet 6	facet 7	facet 8
none	5.83	1.81	2.55	0.94	2.85	2.75	1.12	0.25
0.01	8.53	1.20	4.70	1.43	1.69	6.94	2.95	3.92
0.1	8.50	1.56	2.07	3.80	0.04	5.68	2.68	3.14
1.5	7.92	1.01	3.00	2.00	0.06	7.23	1.87	2.64
3	9.68	1.14	2.91	2.76	0.03	6.97	1.05	1.37

and triangular points (Figure 7g,h). Each etched layer was separated by steps, which were 30.01 nm in height (or multiples thereof). Triangular facets have been observed previously in etched CaF_2,[27] forming lightening-shaped arrangements of intersecting (101) and (110) facets.

3.4. Surface Treatment. High energy surface sites may also be induced through specimen preparation, leading to over-estimated laboratory dissolution rates. Surfaces of CeO_2 were polished to a 0.05 μm finish and subject to dissolution at 150 °C in 0.01 M HNO_3. Dissolution data were compared to those for annealed surfaces. Figure 8 shows VSI images of the surface of a polished monolith after 3 and 14 days of dissolution (Figure 8a,b, respectively). During initial dissolution, the surfaces were rough and pitted, and after 14 days exhibited areas of high and low topography, indicating further dissolution had occurred. It was found that the dissolution rate was an order of magnitude greater for the polished surface than for an annealed CeO_2 surface under the same conditions (Table 2). At 90 °C, the effect was similar; however, the dissolution rate of the polished surface was found to be 3 orders of magnitude greater than that of an annealed surface, with rates of $(7.40 \pm 0.2) \times 10^{-2}$ and $(7.26 \pm 0.2) \times 10^{-5}$ g m^{-2} d^{-1} for polished and annealed surfaces, respectively (Table 1).

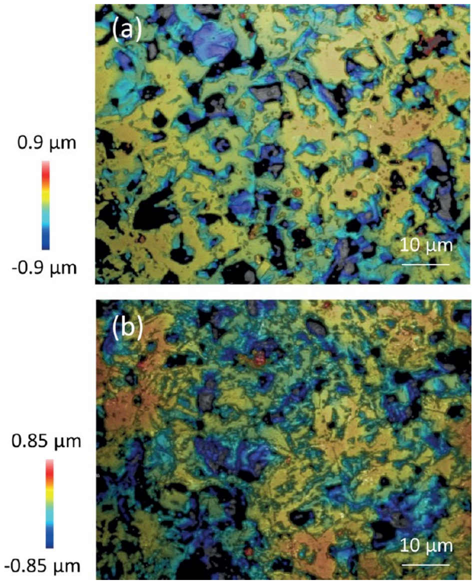

Figure 8. Polished CeO_2 surfaces after dissolution in 0.01 M HNO_3 at 150 °C for (a) 3 days and (b) 14 days.

4. DISCUSSION

In the results presented above, we have observed that surface features act as energetically reactive surface sites that transform during dissolution. These features can be classified into two categories: (i) natural surface features, that is, grain boundaries; and (ii) specimen preparation-induced features, that is, surface facets and polishing defects. The dissolution of these features in CeO_2 and ThO_2 is discussed below, with comparison to the dissolution behavior of UO_2. It should be noted that while the chemical and redox characteristics of the analogue materials investigated here are simple when compared to those of spent fuel, it is possible to draw comparisons between CeO_2, ThO_2, and spent fuel that focus only on the physical and structural properties that give rise to the dissolution behavior observed. As such, in the discussion that follows, only microstructural surface features that affect dissolution are described, with a cautious interpretation for the overall behavior of spent fuel during dissolution.

4.1. Grain Boundary Dissolution. The results presented in this investigation give evidence that UO_2 and spent nuclear fuel analogue grain boundaries undergo extensive transformation during dissolution; material is rapidly removed from grain boundaries in both CeO_2 and ThO_2, corresponding to rapid initial dissolution rates. It is hypothesized that grain boundaries are effective sinks for atomic defect high energy sites;[28] the greater the number of defects, the greater the proportion of high energy surface sites for dissolution. In CeO_2, it has been shown that increasing the density of oxygen vacancy defects results in an increase in the dissolution rate. For example, Horlait et al.[29,30] showed that for every 10% of Ln^{3+} cations added to CeO_2, for which charge compensation through the formation of Ce^{3+} occurred, the dissolution rate increased by 1 order of magnitude.[28] Hojo et al.[31] demonstrated an enrichment of Ce^{3+} in grain boundaries as compared to the grain surfaces, indicative of a higher density of oxygen vacancy defects within the grain boundaries as compared to the surface. In UO_2, evidence for defects within grain boundaries is found in the form of nonstoichiometric UO_{2+x}. For example, Une and Kashibe[32] identified the presence of $UO_{2.25}$ within grain boundaries following dissolution of UO_2, while O'Neil et al.[17] made the observation that grain boundaries in UO_2 were highly conductive, which was attributed to a high concentration of oxygen interstitial ions arising from hypo-stoichiometric UO_{2+x}. This suggests that defects, and especially those that are concentrated within grain boundaries, may play a key role in the dissolution of UO_2 and its analogues. In spent fuel, grain boundaries are expected to contain more defects than laboratory-prepared UO_2 or UO_2 analogues, primarily due to the accumulation of fission gas bubbles and metallic precipitates;[33] therefore, the effects of such high energy surface sites might be expected to be greater.

We have observed that crystallographic orientation of the grains plays an important role in the dissolution of the grain boundaries of spent nuclear fuel analogues; grain boundaries with a high misorientation angle were found to dissolve more rapidly than those with a low misorientation angle in the current study. We hypothesize that high misorientation grain boundaries have a higher concentration of defects (or defect clusters) than grain boundaries with low misorientation angles. Indeed, simulations of UO_2 grain boundaries have shown that different types of defect structure were present in grain boundaries, depending on the misorientation angle;[34] in grain boundaries with lower misorientation angles, edge dislocations were the most common defect, while in higher misorientation angle boundaries, oxygen point defects dominated the grain boundary structure.

Assessment of the safety of geological disposal of spent nuclear fuel requires detailed information on the rates and mechanism of release of radionuclides. This is hypothesized to occur in two main stages: (ii) the so-called "instant release fraction" (IRF), which represents a rapid release of long-lived and geochemically mobile radionuclides (e.g., ^{129}I, ^{36}Cl, ^{135}Cs, ^{99}Tc); and (ii) the slow, long-term release of radionuclides from the UO_2 matrix.[35,36] The IRF is considered to come from two regions of the spent fuel: the gap between the cladding and the fuel, and the grain boundaries. However, the IRF rates are still largely unknown, and the contribution of grain boundary dissolution is not fully understood; in fact, there is some controversy in the literature as to whether grain boundaries make any significant contribution to the IRF.[36,37] The results presented in the current work, which demonstrate an "instant release fraction" of Ce and Th from the spent fuel analogues, which is directly linked to grain boundary dissolution, support the hypothesis that grain boundaries contribute to the IRF in spent fuel, and suggest that crystallographic direction of the grains and the density of defects within the grain boundary may play a role. However, it should be noted that the IRF of spent fuel is largely governed by the complicated chemical composition of the grain boundaries; therefore, the extent to which structural defects and grain boundary misorientation between adjacent grains contribute to the IRF is unknown in comparison to the chemical effects. Our results are also in agreement with the hypothesis that a second, slower stage of spent fuel dissolution occurs; in both CeO_2 and ThO_2, dissolution rates were lower after the initial release. In ThO_2 it was apparent that this second stage of dissolution was impeded by the formation of a protective layer. A similar effect was found in laboratory UO_2 dissolution experiments, where secondary U-bearing alteration products formed a protective layer, preventing further dissolution.[38] On the basis of the data and arguments presented here, it is evident that grain boundary dissolution in spent fuel and spent fuel analogues requires further detailed chemical and physical analysis and that geological disposal safety performance assessment should carefully consider the contribution of grain boundaries to the dissolution rate.

4.2. Dissolution of Specimen Preparation-Induced Features. We show that dissolution occurs at facet edges, especially during initial contact with dissolution medium. With increasingly aggressive dissolution media, the dissolution of these features does not show a particular trend, but instead appears to experience a dynamic process, whereby facet heights constantly change in response to the dissolution medium. We have also shown that each facet contains some aspect of the {111} plane, which is the most stable plane in fluorite-type structures, suggesting that crystallographic orientation also plays an important role in facet formation.

It is thought that facets form by a dislocation growth mechanism during annealing, where spiral-like structures form around threading dislocations likely induced through surface preparation (e.g., polishing). Each dislocation produces a step as it emerges at the surface.[39,40] O'Neil et al.[17] and He and Shoesmith[40] described surface morphologies similar to those identified in the current study in UO_2. Current-sensing AFM analysis showed that UO_2 grains with facets were highly conducting, while smooth grains were not. Raman and EDX investigation of these features revealed a high degree of nonstoichiometry in the UO_2 of faceted grains, attributed to the incorporation of interstitial oxygen atoms to locations in the {110} direction, accompanied by shifts in vacant sites in the {111} direction. It was concluded that these nonstoichiometric, defect-containing features would be more vulnerable to dissolution than defect-free surfaces. Further investigations are currently underway to understand the relative stability of different facet orientations, their degree of nonstoichiometry, and defect structures. It is clear that these high energy surface sites play a role in dissolution, but the evidence presented here suggests that the influence on dissolution rate is not as significant as that of grain boundaries. It is important to note that these features are present as a result of specimen preparation and annealing, and thus are likely to contribute to the potential overestimation of dissolution rates in the laboratory. These features are not expected to be present in spent nuclear fuel.

We found that polished surfaces of spent nuclear fuel analogues gave dissolution rates of up to 3 orders of magnitude greater than for annealed surfaces. Polishing has been shown to introduce strain and defects into oxide material surfaces, giving rise to high surface energy. For example, diamond paste polishing has been shown to result in the formation of dislocation loops, other lattice defects, and also high surface strain.[41,42] Thermally annealing the surface of CeO_2 allowed the strain and defects to be relaxed due to recovery processes during heating, lowering the surface energy, and thus lowering the dissolution rate. It is possible that defects induced during polishing may act as nucleation sites for the observed facet structures formed during annealing. These results show that the introduction of defects to the surface through polishing can lead to a significant increase in the observed dissolution rate, demonstrating the importance of careful specimen preparation for dissolution rate determination.

5. CONCLUSIONS

Dissolution experiments were conducted on non-redox sensitive, isostructural UO_2 and SNF analogues, CeO_2 and ThO_2, to investigate the contribution of energetically reactive surface sites to dissolution, and to determine whether their presence may lead to an overestimation of dissolution rates. Grain boundaries, which are part of the natural texture of SNF, were shown to significantly enhance the dissolution rate, dissolving preferentially in the initial stages of dissolution, supporting hypotheses that grain boundaries contribute to the instant release fraction of spent fuel. A strong crystallographic control was exerted, with high misorientation grain boundaries dissolving more rapidly than those with low misorientation angles in both CeO_2 and ThO_2. It was hypothesized that different crystallographic directions can accommodate different densities of defects, explaining the observations found. Further investigation is required to ascertain the extent to which structural defects and grain boundary misorientation between adjacent grains contribute to the instant release fraction of SNF, in comparison to the chemical effects.

In addition to the natural high energy surface sites found in grain boundaries, energetically reactive sites were also found to be formed through sample preparation. Facet structures formed during annealing, likely nucleated on defects sites on polished surfaces, also exhibited a strong crystallographic control (all combined some aspect of the {111} plane), and upon introduction to dissolution media, they experienced instantaneous dissolution. Finally, the effect of surface polishing on the dissolution rate was found to increase dissolution rates by up to 3 orders of magnitude. This results from induction of strain and defects in the surface during the polishing process. We have shown that defects induced through sample preparation contribute to the dissolution rate. The dissolution from facets is low, and therefore not likely to significantly overestimate long-term dissolution rates; however, sample polishing without any further treatment is likely to cause overestimation of dissolution rates.

AUTHOR INFORMATION

Corresponding Authors

*Tel.: +44 (0)1142226036. E-mail: c.corkhill@sheffield.ac.uk.
*Tel.: +44 (0)1142224570. E-mail: n.c.hyatt@sheffield.ac.uk.

Notes

The authors declare no competing financial interest.

ACKNOWLEDGMENTS

The research leading to these results has received funding from the European Atomic Energy Community's Seventh Framework Programme (FP7) under grant agreement no. 269903, The REDUPP (REDucing Uncertainty in Performance Prediction) project. Special thanks goes to J. Godinho for assistance with vertical scanning interferometry. We are grateful to Dr. Virginia Oversby and Dr. Lena Z. Evins for invaluable discussion and support throughout the project. C.L.C. is grateful to The University of Sheffield for the award of a Vice Chancellor's Fellowship, N.C.H. acknowledges support from the Royal Academy of Engineering and the Nuclear Decommissioning Authority for funding, and D.J.B. and S.M.T. acknowledge financial support from the EPSRC Nuclear FiRST Doctoral Training Centre (EP/G037140/1). We are grateful to the anonymous reviewers of this contribution, for their insightful comments and suggestions, which have greatly improved the manuscript.

REFERENCES

(1) Oversby, V. M. Uranium Dioxide, SIMFUEL and Spent Fuel Dissolution Rates – A Review Of Published Data. *SKB Tech. Rep.*, 1999, TR-99-22.

(2) Shoesmith, D. W. Used Fuel and Uranium Dioxide Dissolution Studies – A Review. *Nucl. Waste Manage. Org. Rep.* **2007**, NMWO TR-2007-03.

(3) Fuel and Canister Process Report for the Safety Assessment SR-Site. *SKB Tech. Rep.*, 2010, TR-10-46.

(4) Smellie, J.; Karlson, F. A Reappraisal of some Cigar Lake Issues of Importance to Performance Assessment. *SKB Tech. Rep.*, 1996, TR 96-08.

(5) Gauthier-Lafaye, F.; Holliger, P.; Blanc, P. L. Natural Fission Reactors in the Franceville Basin, Gabon: A Review of the Conditions and Results of a "Critical Event" in a Geologic System. *Geochim. Cosmochim. Acta* **1996**, *60*, 4831–4852.

(6) Knauss, P.; Wolery, T. J. Dependence of Albite Dissolution Kinetics on pH and Time at 25 °C and 70 °C. *Geochim. Cosmochim. Acta* **1986**, *50*, 2481–2497.

(7) White, A. F.; Bullen, T. D.; Schulz, M. S.; Blum, A. E.; Huntington, T. G.; Peters, N. E. Differential Rates of Feldspar Weathering in Granitic Regoliths. *Geochim. Cosmochim. Acta* **2001**, *65*, 847–867.

(8) White, A. F.; Brantley, S. L. The Effect of Time on the Weathering of Silicate Minerals: Why do Weathering Rates Differ in the Laboratory and Field? *Chem. Geol.* **2003**, *202*, 479–506.

(9) Zhu, C.; Veblen, D. R.; Blum, A. E.; Chipera, S. J. Naturally Weathered Feldspar Surfaces in the Navajo Sandstone Aquifer, Black Mesa, Arizona: Electron Microscopic Characterisation. *Geochim. Cosmochim. Acta* **2006**, *70*, 4600–4616.

(10) Brantley, S. L.; Crane, S. R.; Creear, D.; Hellmann, R.; Stallard, R. Dissolution at Dislocation Edge Pits in Quartz. *Geochim. Cosmochim. Acta* **1986**, *50*, 2349–2361.

(11) Blum, A. E.; Lasaga, A. C. Monte Carlo Simulations of Surface Reaction Rate Laws. In *Chemical Weathering Rates of Silicate Minerals*; Stumm, W., Ed.; Mineralogical Society of America: 1987; Vol. *31*, pp 291–351.

(12) Ollila, K.; Oversby, V. M. Dissolution of Unirradiated UO_2 and UO_2 Doped with ^{233}U Under Reducing Conditions. *SKB Tech. Rep.*, 2005, TR-05-07.

(13) Ollila, K. Dissolution of Unirradiated UO_2 and UO_2 Doped with ^{233}U in 0.01M NaCl Under Anoxic and Reducing Conditions. *Posiva Oy Rep.* **2006**, 2006–08.

(14) Claparede, L.; Clavier, N.; Dacheux, N.; Moisy, N.; Podor, R.; Ravaux, J. Influence of Crystallisation State and Microstructure on the Chemical Durability of Cerium-Neodymium Mixed Oxides. *Inorg. Chem.* **2011**, *50*, 9059–9072.

(15) Stennett, M. C.; Corkhill, C. L.; Marshall, L. A.; Hyatt, N. C. Preparation, Characterisation and Dissolution of a CeO_2 Analogue for UO_2 Nuclear Fuel. *J. Nucl. Mater.* **2013**, *432*, 182–188.

(16) Evins, L. Z.; Juhola, P.; Vahanen, M. REDUPP Final Report. *Posiva Oy Rep.* **2014**, 2014–12.

(17) O'Neil, K. D.; He, H.; Keech, P.; Shoesmith, D. W.; Semenikhin, O. A. Anisotropy of Local Conductivity of Hyper-Stoichiometric Uranium Dioxide Revealed by Current-Sensing Atomic Force Microscopy (CS-AFM). *Electrochem. Commun.* **2008**, *10*, 1805–1808.

(18) Lucuta, P. G.; Verall, V. R.; Maztke, Hj.; Palmer, B. J. Microstructural Features of SIMFUEL – Simulated High-Burnup UO_2-Based Nuclear Fuel. *J. Nucl. Mater.* **1991**, *178*, 48–60.

(19) Papin, P.; Chen, C.-F.; Forsyth, R.; Luther, E.; Necker, C. Surface Preparation for Characterising Microstructure on Transuranic Oxides by Electron Backscatter Spectroscopy and Ion Beam Imaging. *Microsc. Microanal.* **2012**, *18*, 708.

(20) ASTM. *Standard Test Methods for Determining Chemical Durability of Nuclear, Hazardous and Mixed Waste Glasses and Multiphase Ceramics: The Product Consistency Test (PCT)*; ASTM C 1285-02; American Society for Testing and Materials: Philadelphia, PA, 2008.

(21) Rai, D.; Moore, D. A.; Oakes, C. S.; Yui, M. Thermodynamic Model for the Solubility of Thorium Dioxide in the Na-Cl-OH-H_2O System at 23 °C and 90 °C. *Radiochim. Acta* **2000**, *88*, 297–306.

(22) Cui, D.; Low, J.; Spahiu, K. Environmental Behaviours of Spent Nuclear Fuel and Canister Materials. *Energy Environ. Sci.* **2011**, *4*, 2537–2545.

(23) Godinho, J.; Piazolo, S.; Evins, L. Z. Effect of Surface Orientation on Dissolution Rates and Topography of CaF_2. *Geochim. Cosmochim. Acta* **2012**, *86*, 392–403.

(24) Yang, Z.; Woo, T. K.; Baudin, M.; Hermannsson, K. Atomic and Electronic Structure of Unreduced and Reduced CeO_2 Surfaces: A First-Principles Study. *J. Chem. Phys.* **2004**, *120*, 7741–7749.

(25) Maldonado, P.; Godinho, J.; Evins, L. Z.; Oppeneer, P. M. Ab initio Prediction of Surface Stability of Fluorite Materials and Experimental Verification. *J. Phys. Chem. C* **2013**, *117*, 6639–6650.

(26) den Brok, S. W. J.; Morel, J. The Effect of Elastic Strain on the Microstructure of Free Surfaces of Stressed Minerals in Contact with an Aqueous Solution. *Geophys. Res. Lett.* **2001**, *28*, 603−606.

(27) Englehardt, J. B.; Dabringhaus, H.; Wandelt, K. Atomic Force Microscopy Study of the CaF_2 (111) Surface: From Cleavage via Island to Evaporation topographies. *Surf. Sci.* **2000**, *448*, 187−200.

(28) Horlait, D.; Claparede, L.; Tocino, F.; Clavier, N.; Ravaux, J.; Szenknect, S.; Podor, R.; Dacheux, N. Environmental SEM Monitoring of $Ce_{1-x}Ln_xO_{2-x/2}$ Mixed-Oxide Microstructural Evolution During Dissolution. *J. Mater. Chem. A* **2014**, DOI: 101039/c3ta14623e.

(29) Horlait, D.; Clavier, N.; Szenknect, S.; Dacheux, N.; Dubois, V. Dissolution of Cerium(IV)- Lanthanide(III) Oxides: Comparative Effect of Chemical Composition, Temperature, and Acidity. *Inorg. Chem.* **2012**, *51*, 3868−3878.

(30) Horlait, D.; Tocino, F.; Clavier, N.; Dacheux, N.; Szenknect, S. Multiparametric Study of $Th(_{1-x})Ln(_x)O(_{2-x/2})$ Mixed Oxides Dissolution in Nitric Acid Media. *J. Nucl. Mater.* **2012**, *429*, 237−244.

(31) Hojo, H.; Mizoguchi, T.; Ohta, H.; Findlay, S. D.; Shibata, N.; Yamamoto, T.; Ikuhara, Y. Atomic Structure of a CeO_2 Grain Boundary: The Role of Oxygen Vacancies. *Nano Lett.* **2010**, *10*, 4668−4672.

(32) Une, K.; Kashibe, S. Corrosion Behaviour of Irradiated Oxide Fuel Pellets in High Temperature Water. *J. Nucl. Mater.* **1996**, *232*, 240−247.

(33) Marchetti, I.; Carbol, P.; Himbert, J.; Belloni, F.; Fanghanel, T. Room-Temperature Diffusion Coefficients for Oxygen and Water in UO_2 Matrices: A SIMS Study. *Surf. Interface Anal.* **2013**, *45*, 360−363.

(34) Van Brutzel, L.; Vincent-Aublant, E. Grain Boundary Influence on Displacement Cascades in UO_2: A Molecular Dynamics Study. *J. Nucl. Mater.* **2008**, *377*, 522−527.

(35) Johnson, L. H.; Tait, J. C. Release of Segregated Radionuclides from Spent Fuel. *SKB Tech. Rep.*, 1997, TR-97-18.

(36) Johnson, L.; Gunther-Leopold, I.; Kobler Waldis, J.; Linder, H. P.; Low, J.; Cui, D.; Ekeroth, E.; Spahiu, K.; Evins, L. Z. Rapid Aqueous Release of Fission Products from High Burn-Up LWR Fuel: Experimental Results and Correlations with Fission Gas Release. *J. Nucl. Mater.* **2012**, *420*, 54−62.

(37) Serrano-Purroy, D.; Clarens, F.; Gonzalez-Robles, E.; Glatz, J. P.; Wegen, D. H.; de Pablo, J.; Casas, I.; Gimenez, J.; Martinez-Esparza, A. Instant Release Fraction and Matrix Release of High Burn-Up UO_2 Spent Nuclear Fuel: Effect of High Burn-Up Structure and Leaching Solution Composition. *J. Nucl. Mater.* **2012**, *427*, 249−258.

(38) Wronkiewicz, D. J.; Buck, E. C.; Bates, J. K. Grain Boundary Corrosion and Alteration Phase Formation During the Oxidative Dissolution of UO_2 Pellets. *Mater. Res. Soc. Symp. Proc.* **1997**, *465*, 519.

(39) Schick, M.; Dabringhaus, H.; Wandelt, K. Macrosteps on CaF_2 (111). *J. Phys.: Condens. Matter* **2004**, *16*, L33−L37.

(40) He, H.; Shoesmith, D. W. Raman Spectroscopic Studies of Defect Structures and Phase Transition in Hyper-Stoichiometric UO_{2+x}. *Phys. Chem. Chem. Phys.* **2010**, *12*, 8108−8117.

(41) Johansson, S.; Schweitz, J.; Lagerlof, K. P. D. Surface Defects in Polished Silicon Studies by Cross-Sectional Transmission Electron Microscopy. *J. Am. Ceram. Soc.* **1989**, *72*, 1136−1139.

(42) Saito, T.; Hirayama, T.; Yamamoto, T.; Ikuhara, Y. Lattice Strain and Dislocations in Polished Surfaces on Sapphire. *J. Am. Ceram. Soc.* **2005**, *88*, 2277−2285.

PUBLICATION III

Dissolution of ThO_2: study of dissolution process with initial ^{229}Th spike

In: J. Radioanalytical Nucl Chem (2017) 311:225-235

J Radioanal Nucl Chem (2017) 311:225–235
DOI 10.1007/s10967-016-4991-2

Dissolution of ThO_2: study of dissolution process with initial ^{229}Th spike

E. Myllykylä[1] · T. Lavonen[1] · L. Koivula[2] · K. Ollila[1] · M. Siitari-Kauppi[2]

Received: 28 April 2016 / Published online: 18 August 2016

Abstract The sparingly soluble ThO_2 dissolution behaviour was studied under conditions that are expected to prevail in bedrock after the closure of the spent nuclear fuel disposal facility. The objective was to investigate the characteristics of initial dissolution of crystalline $^{232}ThO_2$ by adding ^{229}Th tracer to the aqueous phase in the beginning of the 534 days experiment.The evolution of ^{232}Th concentration and $^{229}Th/^{232}Th$ ratio were followed by sector field ICP-MS (inductively coupled plasma mass spectrometer). Selected samples were measured also by alpha spectrometry to compare the results from the used analysis techniques and they gave comparable results. In the early stage of dissolution there was no significant control by chemical equilibrium and the dissolution process seemed to be controlled by the stability of surfaces.

Keywords ThO_2 · ^{232}Th · ^{229}Th · Dissolution · ICP-MS · Alpha spectrometry

Introduction

In Finland and Sweden the spent nuclear fuel is planned to be disposed into a repository at a depth of more than 400 m in the granitic bedrock. The repository system consists of multiple release barriers: the nuclear fuel matrix, copper canister with a cast iron insert, bentonite buffer around the canister, backfilling of the tunnels and the bedrock itself [1–3]. In this environment, the release of matrix bound radionuclides to the geo- and biospheres will be controlled by the dissolution of the fuel matrix, UO_2. The understanding of the dissolution behavior of the fuel and the solubility of radionuclides in groundwater is essential.

As an oxide material, thorium dioxide (ThO_2) is isostructural to UO_2, sharing the same fluorite-type structure (space group Fm3m), making it a useful structural analogue for spent nuclear fuel matrix, which is predominantly composed of UO_2 (>95 %). However, unlike $U^{(IV)}O_2$, $Th^{(IV)}O_2$ is not redox sensitive since Th has only one prevailing oxidation state, +4 [4]. Because both uranium and thorium form solubility increasing complexes with CO_3^{2-} [4, 5] in aerobic conditions, the dissolution experiments of ThO_2 should be conducted under anaerobic atmosphere.

Most of the ThO_2 solubility studies have been conducted with amorphous phases of ThO_2 [6–10], but there are also some studies conducted with crystalline ThO_2 phases [11]. Hubert et al. concluded that the precursor and calcination temperature of ThO_2 had effects on the surface properties and the apparent leaching rate of dioxide. Oxalate precursor led to the less leachable ThO_2 with better crystallized smooth surface with small specific area compared to ThO_2 fabricated from hydroxide precursor. However, when the leaching rate was normalized to surface area, it seemed to be independent of the precursor and surface characteristics.

Well crystallized ThO_2 is very insoluble in aqueous media [12]. Depending on the crystallinity and crystal size of the Th(IV) oxide and hydroxide or oxyhydroxide phase, the solubility product values vary between $Th(OH)_4$ (am) ($\log K°sp = -46.7 \pm 0.9$ and ThO_2 (microcryst.) ($\log K°sp = -53 \pm 0.5$). [13–15]. According to the equation of Schindler [16] and experimental data, the

---

✉ E. Myllykylä
emmi.myllykyla@vtt.fi

[1] VTT Technical Research Centre of Finland Ltd,
P. O. Box 1000, 02044 Espoo, Finland

[2] Department of Chemistry, Laboratory of Radiochemistry,
University of Helsinki, A.I. Virtasen Aukio 1, P. O.Box 55,
00014 Helsinki, Finland

predicted value for ThO_2 (cr) is log $K°sp = -54.2 \pm 1.1$ [13].

The next generation applications of nuclear energy have also shown interest towards ThO_2 or mixed oxides [17]. As a nuclear fuel, ThO_2 has many beneficial properties, such as high fusion temperature, good sintering capability, resistance against radiation damage, greater abundance in the Earth's crust compared to uranium, and the possibility for transmutation [17]. In addition thorium fuel cycle would have intrinsic proliferation resistance and lesser amount of long lived minor actinides.

In the solubility studies of sparingly soluble crystalline ThO_2 very sensitive analysis methods are needed. Alpha active thorium is traditionally measured by radiometric techniques like alpha spectrometry. As ICP-OES and ICP-MS techniques have become more common analytical tools in laboratories, their usability in thorium analysis has also increased [5, 18]. Alpha spectrometry requires chemical separation of thorium from sample matrix and interfering alpha nuclides as well as the production of a thin source for counting [19]. ICP-OES is suitable for total thorium measurement. Whereas, the mass spectrometry enables the analysis of long-lived thorium isotopes (half-life $>10^4$ years) [18]. Compared to alpha spectrometry the time required for sample preparation and measurement of ICP samples are substantially shorter and less tedious.

The next step of the conventional quadrupole ICP-MS has been the high resolution double focusing sector field mass spectrometer (SF-ICP-MS or HR-ICP-MS) [20], which has been used in this study. The advance is seen in the enhanced sensitivity and better resolution. Compared to the conventional quadrupole technique, the double focusing sector field mass spectrometry has the discrimination of measured m/z values lower than the 0.5–1 mass unit given by the quadrupole ICP-MS [18]. Better mass resolution makes possible to distinguish most of the isobaric and polyatomic interferences that occur nominally at the same mass. For example ^{75}As peaks can be resolved from molecular interference of $^{40}Ar^{35}Cl$ [21], which has been impossible with conventional quadrupole ICP-MS. Even though the molecular and isobaric interference are not a problem at the high mass range, the sensitivity for heavy elements, like ^{232}Th, is also improved. The measurement precision of sector field ICP-MS for non-interfered and heavy elements is higher than that of the quadrupole ICP-MS, because the magnetic sector entrance and exit slits design result in flat top peaks [22].

In this work the dissolution studies were conducted with crystalline ThO_2, which has microstructure similar to UO_2 matrix in fuel pellets [23–26]. The aim was to study behaviour of sparingly soluble ThO_2 conditions that is expected to prevail in spent nuclear fuel disposal site. Initial release and dissolution behaviour/process were studied with leaching studies in which the ^{229}Th tracer was used to evaluate the amounts of dissolved and precipitated thorium. The dissolution of ThO_2 and precipitation of ThO_2 (am, hyd) or $Th(OH)_4$ were followed by analyzing change in ^{232}Th concentration and in $^{229}Th/^{232}Th$ isotopic ratio to inspect the solid/solution interface and sorption onto the reaction vessel walls. An another aim was to compare ICP-MS and alpha spectrometry as a measurement techniques for ^{232}Th and ^{229}Th isotopes, and gain more reliability for results by using two separate analysis techniques for last samples.

Materials and methods

The sintered ThO_2 pellets were made to meet an ideal composition and microstructure similar to the fluorite structure of UO_2 fuel. Making of the pellets is described in detail elsewhere [23]. The pellet surfaces were analysed prior to the solubility experiments with optical microscope and Electron Backscatter Diffraction Analysis in conjunction with a SEM. Grain orientation analysis was performed and the density of the sintered pellets was also measured. The used methods and results are reported in more detail elsewhere [23]. The results showed a microstructure similar to UO_2 fuel pellets; randomly oriented crystals with grain size from 10 to 30 µm.

The dissolution experiments were conducted with 2–4 mm fragments or a single pellet (3.8 mm × 8.7 ∅ mm) in 0.01 M NaCl in an Argon purged glove-box (MB 150 B-G by MBraun). Parallel experimental series were conducted in the same solution by adding ^{229}Th spike (10^{-9} mol/l) at the beginning of the experiment to study the reversibility of surface reactions.

To prevail the anaerobic conditions the dissolution experiments were carried out within Ar glove box (O_2 in water <0.15 ppb, $T = 25 \pm 1$ °C). The 0.01 M NaCl solution was diluted from stock solution (s.p. 99.99 % NaCl by Merck) with Argon purged MilliQ water under the glove box conditions. This was done 3 weeks before the start of the experiments to provide time for equilibration of the solution with the Ar atmosphere. The pH of the solution was adjusted to 6.5 with small aliquot of 0.1 M NaOH. Prior to the experiments, 50 ml of 0.01 M NaCl solution was added with a volumetric flask to PFA Teflon vessel (60 ml). To achieve the initial tracer concentration of 10^{-9} mol/l, 100 µl of ^{229}Th solution (5×10^{-7} mol/l) was added. The excess of ^{229}Th (10 times over the solubility limit) compared to the solubility limit of ThO_2 was needed to study the dissolution/precipitation when the equilibrium was approached from Th-oversaturation. The amount of nitric acid in tracer solution was neutralized with 31 µl of 0.1 M NaOH. The added aliquots were allowed to mix and equilibrate for 1 h before the solid phase was added.

The solid $^{232}ThO_2$ was either in a form of a pellet (3.8 mm × 8.67 mm ; ~2 g) or $^{232}ThO_2$ fragments (2–4 mm; ~0.5 g) originating from the pellet [23]. The pellet was placed on a support screen inside PFA Teflon vessel (60 ml) and the particles were allowed lay in the bottom of the vessel. 1.2 ml samples for the ^{232}Th concentration and for the isotopic ratio (^{229}Th/^{232}Th) analyses were taken from the solution 0 and 1 h, 1, 2, 6, 9, 19, 29, 40, 63, 78, 104 days after addition of the solid phase. After the sampling, the total solution volume was kept unchanged by adding 1.2 ml of 0.01 M NaCl. The samples were acidified with 18 µl of concentrated nitric acid (ULTREX II by Baker). The concentration of ^{232}Th and the isotopic ratio of ^{229}Th/^{232}Th in solution were analyzed with SF-ICP-MS (Element 2).

The liquid samples were not filtered to gain/detect the whole share of ^{232}Th leached out from the solid material including also the colloidal phases. This is essential when calculating the dissolved amounts of ^{232}Th based on the change of isotopic ratio (calculation shown in the next section). Table 1 presents the experimental details for each dissolution experiment.

The leaching was continued altogether for 534 days after which reaction solutions were analyzed. After final sampling, the leaching solution and solid phase were removed from the PFA vessel. Both non-filtered and ultra-filtered samples were taken. The ultrafiltration of sample solution was done to evaluate the amount of colloidal thorium phase in solution samples in the end of the experiments. The sampling was performed with a Pall Mall filtration devices with 10kD (~1 nm) molecular cut off by using centrifugation (6000 rpm; 1 h). To estimate the amount of sorbed thorium on the vessel walls, the vessels were leached with 10 ml of 1 M HNO_3 for 2 days, after which the 2.5 ml samples were taken from leaching solutions. The ^{232}Th concentration and ^{229}Th/^{232}Th isotopic ratio of the leaching solutions were measured with SF-ICP-MS.

Prior to the alpha measurements a 7 ml aliquot of the post-experimental non-filtered samples was taken for the radiochemical separation procedure. Thorium isotopes were separated from other radionuclides present (uranium and daughter nuclides of ^{232}Th; ^{228,224}Ra, ^{220}Rn, ^{216}Po) co-precipitated and filtrated prior to alpha measurement. These radiochemical procedures are commonly used in environmental studies [5, 27, 28]. Uranium separation was needed in the beginning because standard solution for alpha measurements contained both uranium and thorium. First the uranium (and Po) was retained into anion exchange resin (Dowex 1 × 4 by Sigma Aldrich) as $UO_2Cl_4^{2-}$ complex in 9 M HCl, while thorium was flushed through the column with other nuclides. The solution containing thorium was dried out at heat plate and concentrated nitric acid was added to the residue to remove impurities from the sample. The evaporation residue was diluted to 5 ml of 8 M HNO_3 and poured to exchange column (Dowex 1×4) pretreated with 20 ml of 8 M HNO_3. Thorium was retained into column as $Th(NO_3)_6^{2-}$ complex. The other nuclides were rinsed out with 60 ml of 8 M HNO_3, before the elution of Th with 25 ml of 1 M HCl. The purification procedure is illustrated in Fig. 1. The eluted solution of thorium was evaporated to dryness and the residue was diluted to 5 ml of 1 M HCl. This solution was poured to test tube which contained 200 µl of Ce carrier (100 µg/ml). Thorium was co-precipitated as ThF_4 with CeF_4 by adding 0.5 ml of concentrated HF. After HF addition test tube was kept overnight in refrigerator prior to filtration onto 0.1 µm Millipore filter (Type VC). Dry filter papers were clued to sample holder prior to alpha measurements.

Analytical procedure

SF-ICP-MS (Element 2 by ThermoScientific) was used to analyse the concentration of ^{232}Th and the isotopic ratio of ^{229}Th/^{232}Th in solution. The analysis of ^{232}Th was

Table 1 The set-up for experimental series of this study

Experiment	Solid $^{232}ThO_2$	Mass of solid (g)	Solution	[^{229}Th] of spike
A	Pellet	1.97	0.01 M NaCl	1×10^{-9} M
B	Pellet	1.94	0.01 M NaCl	1×10^{-9} M
C	Pellet	2.02	0.01 M NaCl	
D	Pellet	2.00	0.01 M NaCl	
E	Fragments	0.54	0.01 M NaCl	1×10^{-9} M
F	Fragments	0.54	0.01 M NaCl	1×10^{-9} M
G	Fragments	0.53	0.01 M NaCl	
H	Fragments	0.53	0.01 M NaCl	
BLANK (BL)	–	–	0.01 M NaCl	
BL + ^{229}Th	–	–	0.01 M NaCl	1×10^{-9} M

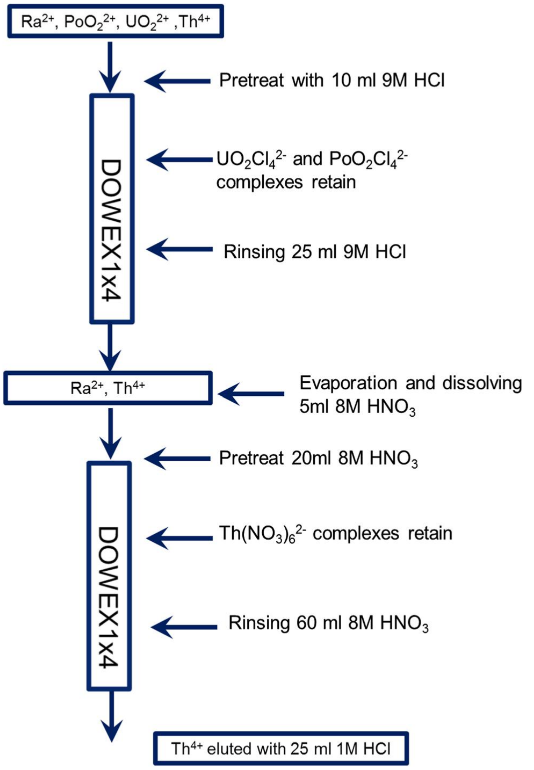

Fig. 1 Separation procedure for thorium prior to precipitation of Th as ThF_4 and alpha measurements

performed with low resolution ($R \approx 300$) using a speed scanning mode. ^{232}Th standards, 0.01, 0.05, 0.5, 1 and 5 ppb, were diluted from the Reference Standard solution SQS-01 (AccuTraceTM). A control sample was prepared from CLMS-1 standard solution (by SPEX). All measured solutions contained an internal standard; 10 ppb of Indium, to control the changes in signal. The samples were injected through SeaSpray nebulizer (0.4 ml/min) and double pass spray chamber equipped with Peltier cooling unit. Washing time between the samples was 3 min with pump speed of 10 rpm. The measuring parameters for the concentration analysis of ^{232}Th and the isotopic ratio analysis of ^{229}Th/^{232}Th are compared in Tables 2 and 3. The isotopic ratio measurement was performed using counting mode only. For the ^{232}Th concentration analysis both modes (counting/analog) were selected. This means that the instrument will automatically switch from counting to analogue mode as the amount of the pulses arise above threshold (5×10^6). The other differences of the measuring parameters are the wideness of the mass and integration windows shown in Tables 2 and 3. In the case of the isotope ratio measurements the amount of samples per peak was arisen from 10 to 25 to acquire more counts with narrower peaks. For the isotopic ratio measurement settling time and segment duration time were shorter than for the ^{232}Th analysis. In the isotopic measurement the detected mass ranges are so close to each other that one and same magnetic mass can be used to measure both isotopes.

The total release of thorium can be calculated from the Eq. (1) when the tracer ^{229}Th was added into the initial solution by using isotope dilution method [29]. The amount of thorium being released to solution from the solid phase can be calculated from measured ^{229}Th/^{232}Th ratio and concentration of ^{232}Th in solution.

$$\frac{^{229}\mathrm{Th}}{^{232}\mathrm{Th}}\mathrm{measured} = \frac{\left([^{229}\mathrm{Th}]\mathrm{initial} + {}^{229}\mathrm{Th\ dissolved}\right)}{([^{232}\mathrm{Th}]\mathrm{initial} + {}^{232}\mathrm{Th\ dissolved})} \quad (1)$$

Even if the precipitation or sorption onto the vessel walls occurs the change in isotopic ratio will give the amount of material transferred from the solid phases (pellet surface or precipitates at vessel surface) through solution. The calculation of each measurement is based on the change of isotopic ratio ^{229}Th/^{232}Th between two measument points and the initial shares and concentrations of ^{229}Th and ^{232}Th in solid and in aqueous phase. Furthermore the increase or decrease of both isotopes and the following amount of ^{229}Th and ^{232}Th in solution can be calculated. The first ^{229}Th concentration was 10^{-9} mol/l after. ^{229}Th tracer contained 3.1×10^{-2}wt% of ^{232}Th isotope according to the sertificate given by the provider (Oak Ridge National Laboratory). The initial concentration of ^{232}Th in experimental solution was calculated to be 3.1×10^{-13} mol/l. The ^{229}Th content of solid $^{232}ThO_2$ pellet was unkown and following assumption was used in calculations; 99.9999 at.% of ^{232}Th and 0.0001 at.% of ^{229}Th.

The alpha spectra of the samples after the separation procedure were analysed under vacuum with Canberra 450 PIPS detector using analysis program MAESTRO for Windows Model A65-332. Energy calibration was conducted with reference sample containing ^{237}Np ($E_{\alpha 1} = 4788$ keV, $I = 47$ %), ^{241}Am ($E_{\alpha 1} = 5486$ keV, $I = 84.5$ %), ^{244}Cm ($E_{\alpha 1} = 5805$ keV, $I = 76.4$ %). Energy resolution for the four detectors used in the measurements was between 23 and 48 keV. The background spectra were subtracted from the samples' alpha spectra. Before the subtraction, the background, with measuring time 19 h, was scaled to the same level with measuring times of the samples (29 h for A and B, 48 h for E and F). The peaks of the thorium and daughter nuclides were identified from the spectra and the pulses were integrated from thorium peaks (^{228}Th and ^{229}Th) to calculate the activity using geometry efficiency correction of each alpha detector. These correction factors were calculated with

Table 2 The parameters used in ICP-MS methods for measuring ^{232}Th

Isotope	Accurate mass	Mass window	Mass range	Magnet mass	Settling time	Samples per peak	Segment duration	Search window	Integration window	Detection mode
^{115}In	114.9033	150	114.616–115.191	114.903	0.300	10	0.150	150	80	Both[a]
^{232}Th	232.0375	150	231.547–232.618	232.038	0.062	10	0.150	150	80	Both[a]

[a] Counting/analogue depending on the amount of pulses

Table 3 The parameters used in ICP-MS methods for measuring isotope ratio ^{229}Th/^{232}Th

Isotope	Accurate mass	Mass window	Mass range	Magnet mass	Settling time	Samples per peak	Segment duration	Search window	Integration window	Detection mode
^{229}Th	229.0350	20	228.595–229.111	229.035	0.001	25	0.050	0	20	Counting
^{232}Th	232.0375	20	231.960–232.115	229.035	0.001	25	0.050	0	20	Counting

AASI simulation [30] (0.05 % accuracy) which acquires the detector and sample diameters, sample distance from the detector and energy resolution of the detector. The activities of ^{299}Th in 7 ml sample aliquots were transformed to amount of moles with Eq. 2 to compare them to the concentrations analysed with ICP-MS.

$$A = \lambda N = \frac{\ln 2}{t_{1/2}} n N_A \qquad (2)$$

In which the A is activity, $t_{1/2}$ is half-life of the nuclide, n is the amount of nuclide in moles, and N_A is Avogadro's constant.

Results and discussion

The initial pH of 0.01 M NaCl was 6.5, and it increased to 8 after the contact of phases in the very beginning of the experiment. During the 104 days experimental period, the pH continued to increase slightly into ~9 due to the dissolution of oxide, which decreases acidity (H^+) in the solution ($ThO_2(s) + 4H^+ \leftrightarrow Th^{4+} + 2\ H_2O(l)$ [13]). Figure 2 shows the evolution of thorium concentration in dissolution experiments measured by ICP-MS. During the first day relatively fast increase of dissolved ^{232}Th from solid phase was observed. After this the ThO_2 fragment samples E–H showed slight increase of ^{232}Th concentration and decrease of ^{229}Th concentration, both settling between 10^{-11} and 10^{-10} mol/l within 60 days. In pellet experiments A–D, [^{232}Th] decreased after the initial release. This was seen in the previous experiments [23, 31] as well. The pellet samples A and B approached the equilibrium form oversaturation and the pellet samples C and D from undersaturation. Any of those did not achieve the constant level in 104 days. The thorium concentrations (samples A–D) showed rather slight decrease than levelling down to constant thorium level. The pellet samples A and B behaved differently to each other which might be due to non-identical pellet surfaces e.g. surface energies. The concentrations of both isotopes ^{232}Th and ^{229}Th showed almost one order of magnitude difference in the parallel experiments conducted with pellet A and B. In the experiment A the thorium concentrations were close to 10^{-10} mol/l where as in experiment B the concentrations of both isotopes dropped below 10^{-11} mol/l after 40 days reaction time. The lower pH of sample B might also have had some effect on the observed difference, as the pH difference varied from 0.8 pH units at the early stage to 0.5 pH units at the end of the experiment. On the other hand, the release calculations of ^{232}Th with the isotopic dilution method showed, that pellet A dissolved up to 40 days, whereas in experiment B reaction turns to precipitation after 20 days (see Fig. 5).

In the experiments A, B, E and F the solution was labeled with ^{229}Th tracer. The initial tracer concentration was 10^{-9} mol/l of ^{229}Th, and it decreased towards 10^{-10} mol/l or little bit below it, during 104 days experiment. However, the release of ^{232}Th from the solid ThO_2 phase into the aqueous phase was not hindered by the excess of ^{229}Th. In all experiments, the ^{232}Th concentration was above 10^{-11} mol/l within the first 2 days. In the experiments conducted with pellets in tracer solution (A and B) the ^{232}Th concentration increased around 10^{-10} mol/l within 2 days. The fast release most probably occurs due to "high energy surface sites", like grain boundaries and crystallographic defects, which play a significant role in early stage dissolution. The dissolution process seems not to be controlled only by chemical equilibrium but also by surface stability of the dissolving sample surfaces. Similar observations have been made in studies by Corkhill et al. [31].

When comparing the oversaturation experiments with ^{229}Th tracer (A, B, E and F) and under saturation experiments without ^{229}Th tracer (C, D, G and H), the ^{232}Th

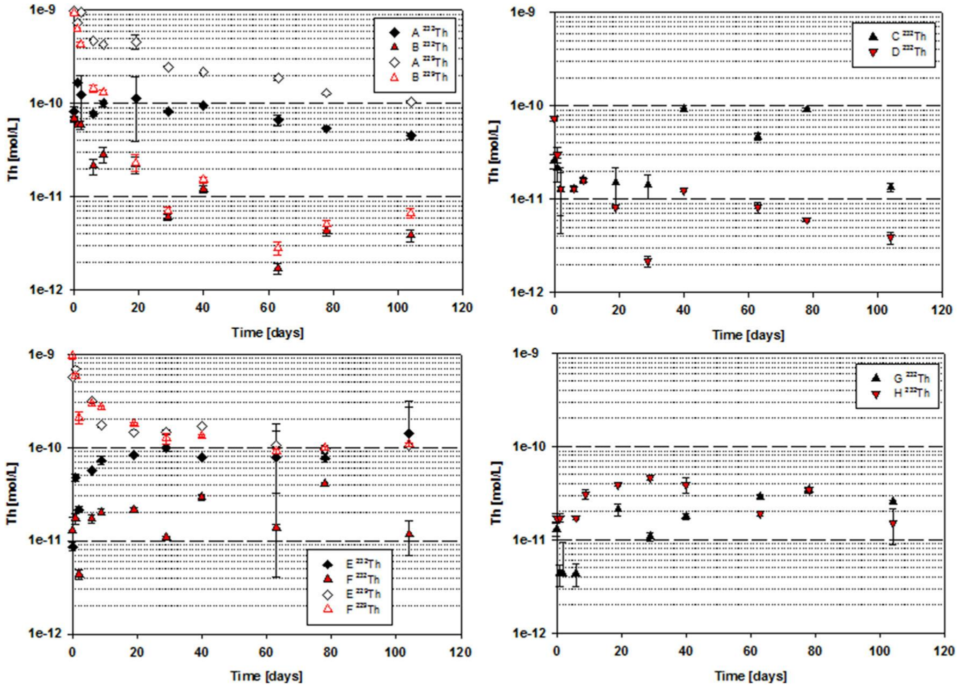

Fig. 2 Evolution of thorium concentrations (by SF-ICP-MS) in dissolution experiments conducted with pellet (*A–D*) and fragment (*E–H*) samples

concentration was found to be slightly higher level in the experiments conducted with tracer. This can be expected from the saturation point of view if the experiments haven't achieved the equilibrium in 104 days. On the other hand thorium hydroxides/oxyhydroxides, forming in slightly basic solution, have a high tendency for sorption. In the case of oversaturation, most sorption and precipitation occurs among ^{229}Th in early stage of the experiment, because there is an excess of ^{229}Th. Whereas, in the undersaturation experiments lacking ^{229}Th, the sorption takes place from the fraction of ^{232}Th, which is first dissolved from the solid phase. This might generate higher observed concentration level of ^{232}Th in oversaturation experiments (A, B, E and F).

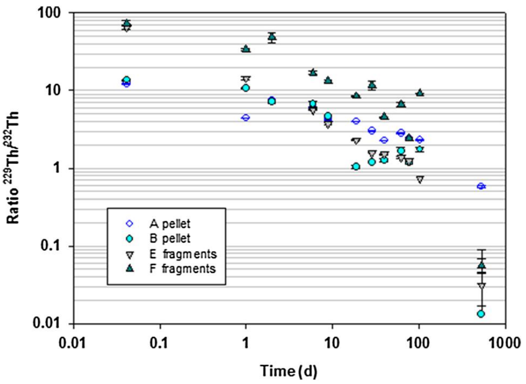

Fig. 3 Evolution of ^{229}Th/^{232}Th ratios (by SF-ICP-MS) in dissolution experiments conducted with tracer (*A*, *B*, *E*, and *F*) during 534 days

When considering the isotopic ratios, one should pay attention that there is a huge excess of ^{232}Th isotope (in moles), in a reaction vessel. The calculated molar ratios between aqueous ^{229}Th and solid ^{232}Th in the beginning of the experiment are 6.6×10^{-9} and 1.9×10^{-8} for pellet and fragment ThO_2 experiments. On the other hand the initial calculated ^{229}Th/^{232}Th ratio in 0.01 M NaCl solution with ^{229}Th tracer was 3226. Figure 3 presents the decrease of the ^{229}Th/^{232}Th ratios in tracer experiments (A, B, E, F). Clear decrease was found in all experiments. The ratio dropped significantly in all experiments during the first day, which is in agreement with the initial fast release of ^{232}Th from solid phase (see Fig. 2, experiments A, B, E, F). The isotopic ratio approached 1 within 104 days and the concentration values reached almost constant level after 50 days (see Figs. 2, 3). The continuous decrease in isotopic ratio show that the dissolution/precipitation reactions continue in equilibrium state as expected. When the

Table 4 ^{229}Th/^{232}Th ratios (by SF-ICP-MS) in dissolution experiments conducted with tracer (A, B, E, and F) in solution and vessel walls (in vessel leachates) after 534 days

Sample type	A	B	E	F
SOLUTION 534 d	0.580	0.013	0.031	0.056
Vessel leachate	0.336	0.515	1.095	0.983

leaching was continued over 500 days the ^{229}Th/^{232}Th ratios dropped clearly under 1. The ratios in fragment experiments (E and F) decreased even below 0.1.

Table 4 shows the ^{229}Th/^{232}Th isotopic ratios measured in leaching solution and in vessel leachates taken form the vessel walls. The measured ratios show that in most cases the amount of ^{229}Th is higher at the vessel walls than in solution. However the ratios are remarkable lower than the ratios measured in the beginning of the experiment. This suggests that the dissolved ^{232}Th is also sopbed and precipitated on the vessel walls and there is dissolution competition not only at the solid surface of ThO_2 but also at the vessel walls, which might also cause differences in thorium concentrations bewtween parallel samples, like in the case of samples A and B (see Fig. 2).

Figure 4 shows the ^{232}Th results of reaction vessel out leachates after the dissolution experiment. In addition it presents the results of 104 and 534 days dissolution experiment. The ultra-filtrated samples after 534 days experiment are not presented, because the concentrations were all below 5×10^{-12} mol/l (close to detection limit or even below it), indicating that most of the thorium in aqueous phase was present in colloidal form. The concentrations of ^{232}Th were 2–3 orders of magnitude higher in the out leachates (1 M HNO_3) compared to the concentrations measured in 0.01 M NaCl solutions after 104 and 534 days dissolution experiments. This means that the amount of ^{232}Th sorption or precipitation on vessel walls was significant. Clearly elevated ^{232}Th concentrations were observed after 534 d dissolution. In comparison between the 104 and 534 days results the later sampling showed elevated thorium concentrations in non-filtered solution whereas ^{232}Th was not detected in ultra-filtered solutions. Thorium is known to form polynuclear species and colloids in slightly basic conditions [4, 5] and the increase of concentration here indicates the increase of colloidal phases in solution as the dissolution of the solid proceeds from 104 to 534 days. These polynuclear and colloidal species have high tendency for sorption on to the surfaces, what agrees with the observations.

Figure 5 shows the concentrations of released ^{232}Th from ThO_2 pellets (A, B) and ThO_2 fragments (E, F) experiments versus time analyzed with ICP-MS and calculated with isotopic dilution method. The linear fits are given to all calculated points from 0 to 10 days to evaluate the initial release/dissolution rates based on isotopic method. To evaluate the decrease of the rate after initial release 2nd rates were also fitted for those samples for

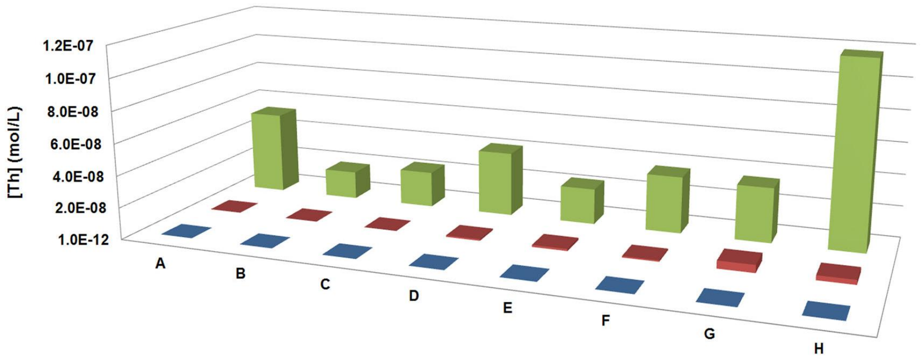

	A	A error	B	B error	C	C error	D	D error
🟦 Solution (104 d)	$4.57\cdot10^{-11}$	$0.34\cdot10^{-11}$	$0.39\cdot10^{-11}$	$0.06\cdot10^{-11}$	$1.34\cdot10^{-11}$	$0.13\cdot10^{-11}$	$0.39\cdot10^{-11}$	$0.01\cdot10^{-11}$
🟥 Solution (534d)	$2.21\cdot10^{-11}$	$0.02\cdot10^{-11}$	$6.91\cdot10^{-11}$	$0.05\cdot10^{-11}$	$3.51\cdot10^{-11}$	$0.03\cdot10^{-11}$	$93.85\cdot10^{-11}$	$4.44\cdot10^{-11}$
🟩 Vessel leachates	$5.25\cdot10^{-08}$	$0.07\cdot10^{-08}$	$1.78\cdot10^{-08}$	$0.02\cdot10^{-08}$	$2.29\cdot10^{-08}$	$0.04\cdot10^{-08}$	$4.08\cdot10^{-08}$	$0.10\cdot10^{-08}$

	E	E error	F	F error	G	G error	H	H error
🟦 Solution (104 d)	$14.22\cdot10^{-11}$	$16.68\cdot10^{-11}$	$1.16\cdot10^{-11}$	$0.47\cdot10^{-11}$	$2.59\cdot10^{-11}$	$0.06\cdot10^{-11}$	$1.51\cdot10^{-11}$	$0.04\cdot10^{-11}$
🟥 Solution (534d)	$128.55\cdot10^{-11}$	$1.45\cdot10^{-11}$	$85.45\cdot10^{-11}$	$1.26\cdot10^{-11}$	$488.25\cdot10^{-11}$	$471.26\cdot10^{-11}$	$295.48\cdot10^{-11}$	$2.98\cdot10^{-11}$
🟩 Vessel leachates	$2.27\cdot10^{-08}$	$0.02\cdot10^{-08}$	$3.59\cdot10^{-08}$	$0.03\cdot10^{-08}$	$3.46\cdot10^{-08}$	$0.03\cdot10^{-08}$	$11.73\cdot10^{-08}$	$0.24\cdot10^{-08}$

Fig. 4 ^{232}Th results of 104 and 534 days dissolution experiments and of reaction vessel out leachates measured by SF-ICP-MS

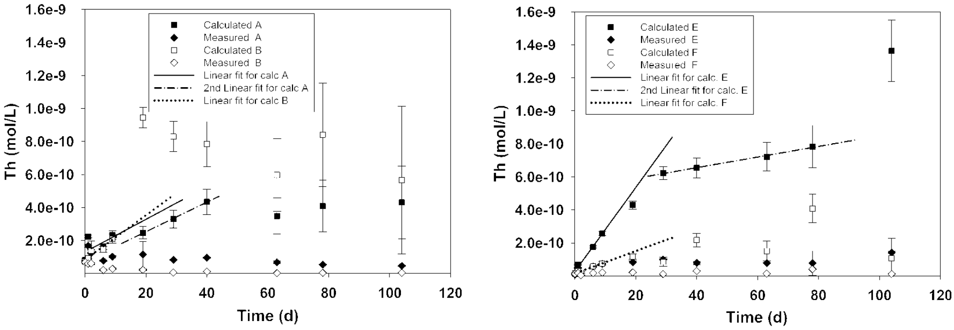

Fig. 5 Concentrations of released ^{232}Th from ThO_2 pellets (*A*, *B*) and ThO_2 fragments (*E*, *F*) versus time analysed with ICP-MS and calculated with isotopic dilution method. The linear fits were given for calculated values during the first 10 days and for experiments *A* and *E* also for 19–40 and 29–78 days respectively

Table 5 The initial dissolution rates (10 days) of ThO_2 with isotopic dilution method and the values used in calculations; d*c*/d*t*, masses of solid and volumes of solutions (2nd means secondary rate after 20 days)

Tracer experiment	d*c*/d*t* (mol l^{-1} day^{-1})	Mass of solid (g)	Volume of solution (L)	Rate (mol g^{-1} s^{-1})
A	1.55E−11	1.97	0.05	4.6E−18
A (2nd)	8.94E−12	1.97	0.05	2.6E−18
B	1.35E−11	1.94	0.05	4.0E−18
E	2.54E−11	0.54	0.05	2.7E−17
E (2nd)	3.22E−12	0.54	0.05	3.5E−18
F	6.78E−12	0.54	0.05	7.3E−18

which it was possible. For sample A the fit was given between 19 and 40 days (2nd rate), and for sample E between 29 and 78 days (2nd rate). As can be seen the amount of released ^{232}Th and the dissolution rates are higher by the isotopic method than by measuring only the concentration of ^{232}Th in the solution. This is a sign of continuous dissolution/precipitation reaction which was earlier seen from the continuous change of isotopic ratios even in the 534 days experiments. With isotopic dilution method it is possible to see the total flux of thorium. In reality the amount of released/dissolved thorium is much higher than the share of soluble one because the precipitation occurs simultaneously.

The dissolution rates for ThO_2 were calculated by using the Eq. (3) from the total release of ^{232}Th calculated with isotopic dilution method.

$$r_{^{232}\mathrm{Th}} = \frac{V}{m}\frac{\mathrm{d}c^{232}\mathrm{Th}}{\mathrm{d}t} \tag{3}$$

where *V* is the volume of the solution (L), *m* is the mass (g) of ThO_2 and d*c*/d*t* is the slope (linear fit) determined from the evolution of ^{232}Th release as function of time (mol l^{-1} s^{1}). The results are given in a Table 5.

The dissolution rates for pellet samples (A, B) did not show significant difference in the beginning of the experiment. However in 20 days sample B had achieved comparably high maximum concentration and started to form precipitates rather than dissolve. Whereas A continued dissolution with slightly slower rate (2nd rate) than in the beginning. The fragment sample E showed a bit higher rate than the other ones in the early state of the experiment. As in the case of sample A the rate sample E also decreased under 4 × 10^{-18} mol g^{-1} s^{-1} later on. These 2nd rates are probably closer to the realistic ones during the long time

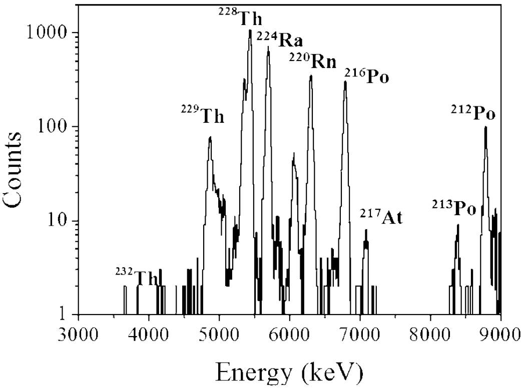

Fig. 6 Alpha spectrum of coprecipitate Ce/ThF_4 after the dissolution experiment B (534 days)

Table 6 Comparison of ^{229}Th concentrations measured with alpha spectroscopy and ICP-MS analysis (534 days experiments)

Experiment	Alpha spectroscopy			ICP-MS analysis		
	^{229}Th (n)	^{229}Th (mol)	[^{229}Th] (mol/l)	[^{232}Th] (mol/l)	Ratio ^{229}Th/^{232}Th	[^{229}Th] (mol/l)
A	5.14E+10	8.53E−14	1.22E−11	2.2E−11	0.58	1.28E−11
B	1.72E+10	2.86E−14	4.09E−12	6.9E−11	0.013	8.98E−13
E	1.11E+11	1.84E−13	2.63E−11	1.3E−09	0.031	3.99E−11
F	1.07E+11	1.78E−13	2.54E−11	8.5E−10	0.056	4.78E−11

dissolution as the fast initial release from high energy surface sites has mostly occurred at the initial stage of leaching.

One of the aims was to compare the ICP-MS analyses with the technique which uses chemical separation and alpha spectrometry. The detection limit for the analyses were calculated as six times the standard deviation of the ion counts obtained for the sample blanks (min. ten replicates), divided by the measured counts for ^{232}Th in 1 µg/l standard solution. The detection limit of ^{232}Th varied from 1×10^{-12}mol/l to 4×10^{-12}mol/l depending on the daily efficiency of the ICP-MS instrument. The detection limit of ^{229}Th by ICP-MS is of the same order of magnitude as of ^{232}Th.

Figure 6 presents the alpha spectrum of the dissolution experiment B (see Table 1) after 534 days leaching. The measurement was done after the chemical separation and co-precipitation as Ce/ThF_4. The peaks of tracer ^{229}Th and ^{228}Th, which is a daughter nuclide of ^{232}Th, were clearly detected, whereas ^{232}Th ($t_{1/2} = 1.4 \times 10^{10}$) appears as a very small peak. Also the peaks of the other daughters, for example ^{224}Ra, ^{220}Rn, ^{216}Po and ^{212}Po from the ^{232}Th and ^{229}Th decay series, were observed as well in the spectra. The appearance of daughter nuclides is due to the time difference of 7 days between separation and alpha measurement. The decay proceeds after separation and amount of daughter nuclides increase as the time between separation and measurement increases.

The detection limit of ^{232}Th in alpha spectrometry was 7.6×10^{-11} mol/l (0.0007 Bq/l) calculated by Currie method [32]. This is more than a decade higher than the detection limit achieved with ICP-MS preferring it as a sensitive technique for ^{232}Th. On the other hand the detection limit of ^{229}Th was 1.34×10^{-16} mol/l (0.00024 Bq/l) which is significantly better than with ICP-MS. The detection limit of ^{232}Th via the activity measurement is higher than that of ^{229}Th due to its longer half-life ($t_{1/2}(^{232}\text{Th}) = 14 \times 10^{9}$ years) compared to $t_{1/2}(^{229}\text{Th}) = 7340$ years) and thus lower specific activity. One point that has to be taken into account in the alpha spectroscopy is separation procedure that was time consuming and tedious and the benefit of the lower detection limit was not easy to achieve.

The two methods gave comparable results as can be seen in Table 6 except in the case of the pellet sample B in which the measured concentration of ^{229}Th by ICP-MS was four times lower than the concentration measured with alpha spectrometry. Sample B has lowest concentration, which causes more uncertainty in the results of the both measurements.

Conclusions

This solubility study of ThO_2(s, am) has increased the understanding of the behaviour of sparingly soluble ThO_2 under conditions that is expected to prevail in spent nuclear fuel disposal site. In these conditions ThO_2(s, am) is in contact with thorium hydroxide mono and polymeric complexes, which tend to control the solubility limit. In the dissolution experiments with actinide(IV) oxides the sole concentration analysis of the solution does not provide information about the dissolution rate, whereas the isotope dilution method enables to calculate the amount of released isotopes and give insight to the rate of the dissolution.

The fast initial release of ^{232}Th from $^{232}ThO_2$ was observed despite of ^{229}Th excess in 0.01 M NaCl solution. In the early stage of dissolution there was no significant control by chemical equilibrium and the dissolution process seemed to be controlled by the stability of surfaces. The fast release took most probably place on grain boundaries and crystallographic defects which can be defined as “high energy surface sites”. The solubility was observed to level down or slightly decrease during the 104 days experiment. Later on the chemical control, colloid formation (polynuclear species) and maybe also the crystallinity of the secondary phases, seemed to play more significant role in a dissolution process.

Even though the measured thorium concentrations showed levelling or decreasing trend over 104 days the isotope ratio ^{229}Th/^{232}Th decreased continuously over 534 days. This means that the constant concentration can be achieved, but results indicate that the dissolution/precipitation reactions are still ongoing at the solid solution interface. During the long term experiments the precipitation took place also to the vessel surfaces and the amount of colloidal phases was increased in the solution. Most of the released ^{232}Th was found from vessel out leachates, which showed that the dissolved ^{232}Th either sorbed or precipitated on the reaction vessel walls.

The detection limit for measured thorium isotopes by sector field ICP-MS was 1×10^{-12}–4×10^{-12} mol/l. Alpha spectrometry can provide better detection limit for isotopes with moderately long half-lives, like 1.34×10^{-16} mol/l for ^{229}Th ($t_{1/2} = 7340$ years), but the detection limit for really long lived isotopes, like ^{232}Th was better with ICP-MS. A drawback of the alfa spectroscopy is that the sample preparation needs tedious chemical separation procedures and takes time. On the other hand alpha spectrometry shows the presence of daughter nuclides, with relatively short half lives, even in really low levels, which are undetectable with ICP-MS.

Acknowledgments This study has been part of REDUPP project. The research leading to these results has received funding from the European Atomic Energy Community's Seventh Framework program (FP7) under grant agreement No. 269903. We thank also safir2018 and YTERA doctoral school for funding this study. Jaana Rantanen, Kerttuli Helariutta and Merja Tanhua-Tyrkkö are also thanked for their help and good advices.

References

1. Alexander WR, McKinley LE (ed) (2008) Deep geological disposal of radioactive waste. Elsevier series. Radioactivity in the environment. vol 9
2. Combie C, Pescatore C, Smith P, van Luik A (1999) Geological disposal of radioactive waste. Review of developments in the last decade. OECD Publications, Paris
3. SKB 91Final disposal of spent nuclear fuel. Importance of the bedrock for safety (1992) SKB Technical Report TR-92-20, Swedish Nucl Fuel Waste Manag Co (SKB). Stockholm, May 1992 pp 230
4. Morss LR, Edelstein NM, Fuger J, Katz JJ (2006) The chemistry of the actinide and transactinide elements. Springer, New York
5. Lehto J, Hou X (2011) Chemistry and analysis of radionuclides: laboratory techniques and methodology. Wiley-VCH, Hoboken pp 255–276
6. Bundschuh T, Knopp R, Müller R, Kim J, Neck V, Fanghänel T (2000) Application of LIBD to the determination of the solubility product of thorium (IV)-colloids. Radiochim Acta 88:625
7. Rothe J, Denecke M, Neck V, Müller R, Kim J (2002) XAFS investigation of the structure of aqueous thorium (IV) species, colloids, and solid thorium (IV) oxide/hydroxide. Inorgan chem 41(2):249–258
8. Bitea C, Müller R, Neck V, Walther C, Kim J (2003) Study of the generation and stability of thorium (IV) colloids by LIBD combined with ultrafiltration. Colloids Surf A 217(1):63–70
9. Altmaier M, Neck V, Fanghänel T (2004) Solubility and colloid formation of Th(IV) in concentrated NaCl and $MgCl_2$ solution. Radiochim Acta 92:537–543
10. Walther C, Fuss M, Buchner S (2008) Formation and hydrolysis of polynuclear Th(IV) complexes-a nano-electrospray mass-spectrometry study. Radiochim Acta 96(7):411–426
11. Hubert S, Barthelet K, Fourest B, Lagarde G, Dacheux N, Baglan N (2001) Influence of the precursor and the calcination temperature on the dissolution of thorium dioxide. J Nuclear Mater 297(2):206–213
12. Weast RC, Astle MJ (1981) CRC Handbook of chemistry and physics, 61st edn. CRC Press, Florida
13. Fuger J, Rand M, Grenthe I, Neck V, Rai D (2007) Chemical thermodynamics of thorium. OECD Nuclear Energy Agency, Paris
14. Neck V, Müller R, Bouby M, Altmaier M, Rothe J, Denecke MA, Kim JI (2002) Solubility of amorphous Th(IV) hydroxide—application of LIBD to determine the solubility product and EXAFS for aqueous speciation. Radiochim Acta 90:485
15. Neck V, Altmaier M, Müller R, Bauer A, Fanghänel T, Kim JI (2003) Solubility if crystalline thorium dioxide. Radiochim Acta 91:253–262
16. Schindler PW (1967) Heterogenous equilibria involving oxides, hydroxides, carbonates and hydroxide carbonates. Adv Chem Ser 67:196
17. Dekoussar V, Dyck GR, Galperin A, Ganguly C, Todosow M, Yamawaki M (2005) Thorium fuel cycle—potential benefits and challenges. IAEA, IAEA-TECDOC-1450, Vienna
18. Holmes L (2001) Determination of thorium by ICP-MS and ICP-IES 2001. Radiat Prot Dosim 97(2):117–122
19. Gingell T (2001) thorium isotopic analysis by alpha spectrometry. Radiat Prot Dosim 97(2):109–116
20. Becker JS, Dietze HJ (1997) Double focusing sector field inductively coupled plasma mass spectrometry for high sensitive multi-element and isotopic analysis. J Anal At Spectrom 12:881–889
21. Pröfrock D, Prange A (2012) Inductively coupled plasma-mass spectrometry (icp-ms) quantitative analysis in environmental and life sciences: a review of challenges, solutions, and trends. Appl Spectrosc 66(8):843–868
22. Shen C-C, Edwards LR, Cheng H, Dorale JA, Thomas RB, Moran SB, Weinstein SE, Edmonds HN (2002) Uranium and thorium isotopic and concentration measurements by magnetic sector field coupled plasma mass spectrometry. Chem Geol 185:165–178
23. Myllykylä E, Lavonen T, Stennett M, Corkhill C, Ollila K, Hyatt N (2015) Solution composition and particle size effects on the dissolution and solubility of a ThO_2 microstructural analogue for UO_2 matrix of nuclear fuel. Radiochim Acta 103(8):565–576
24. Stennett MC, Corkhill CL, Marshall LA, Hyatt NC (2013) Preparation, characterisation and dissolution of a ceo_2 analogue for uo_2 nuclear fuel. J Nucl Mater 432:182–188
25. Forsyth R (1987) Fuel rod D07/B15 from Ringhals 2 PWR: Source material for corrosion/leach tests in groundwater. Fuel rod/pellet characterisation program part 1. SKB technical report 87-02
26. Forsyth R (1995) Spent nuclear fuel. A review of properties of possible relevance to corrosion processes. SKB technical report 95–23
27. Rozmaric M, Ivsic AG, Grahek Z (2009) Determination of uranium and thorium in complex samples using chromatographic separation ICP-Ms and spectrophotometric detection. Talanta 80:352–362
28. Kiliari T, Pashalidis I (2011) Thorium determination in aqueous solutuons after separation by ion-exchange and liquid extraction. J Radionanal Nucl Chem 288:753–758
29. Ollila K, Albinson Y, Cowper M (2003) Dissolution rates of unirradiated UO_2, UO_2 doped with ^{233}U, and spent fuel under

normal atmospheric conditions and under reducing conditions using an isotope dilution method, SKB Technical Report TR-03-13
30. Siiskonen T, Pöllänen R (2005) Advanced simulation code for alpha spectrometry. Nucl Instrum Methods Phys Res Sect A 550(1–2):425–434
31. Corkhill C, Myllykylä E, Bailey D, Thornber S, Qi J, Maldonado P, Stennett M, Hamilton A, Hyatt N (2014) The contribution of energetically reactive surface features to the dissolution of CeO_2 and ThO_2 analogues for spent nuclear fuel. ACS Appl Mater Interfaces 6(15):12279–12289
32. Currie LA (1999) Detection and quantification limits:origins and historical overwiew. Anal Chim Acta 391:127–134

PUBLICATION IV

Direct alpha spectrometry for analysing the leached ThO_2 pellets

Submitted in: Journal of Nuclear Materials, December 2016
Revised March 2017

Direct alpha spectrometry for analysing the leached ThO_2 pellets

E.Myllykylä[1], L.Koivula[2], M.Tanhua-Tyrkkö[1], K.Helariutta[2], T.Lavonen[1], K.Ollila [1], M.Siitari-Kauppi[2]

[1]VTT Technical Research Centre of Finland, Espoo, Finland

[2] Department of Chemistry, Laboratory of Radiochemistry, University of Helsinki, A.I.Virtasen aukio 1, 00014 Helsingin yliopisto, Finland

Abstract

The next generation application of nuclear energy have shown the interest towards ThO_2 or mixed oxides. However, more knowledge is needed, for example, microstructural and matrix dissolution behaviour of ThO_2. The objective of this study was to examine the surfaces of ThO_2 pellets by alpha spectrometry before and after the leaching experiment. The non-destructive analysis method uses Monte Carlo simulations to demonstrate the properties of the surface of thick ThO_2 pellets. This study has been conducted to investigate the contents and thickness surface layer and bulk of crystalline $^{232}ThO_2$ leached in aqueous solution with excess of ^{229}Th tracer in the beginning of the experiment. The simulation results have suggested a maximum 0.1µm concentrated layer of ^{229}Th on the pellet surface. The presence of this layer suppress further dissolution of the pellet.

1. Introduction

The solubility values for ThO_2 have shown great discrepancies in literature [1-3]. Published values differ by orders magnitude depending the crystallinity of the solid phase and the original saturation state of the solution. A possible reason for discrepancies is also the complicated solution chemistry of thorium; strong absorption to surfaces, tendency for polynucleation and colloid formation including the low solubility of ThO_2, Th(IV) hydrous oxide and Th hydroxide phases.

As a fuel, ThO_2 (thoria) has many beneficial properties, such as high fusion temperature, good sintering capability, resistance against radiation damage, greater abundance in the Earth's crust compared with U, and the possibility for transmutation [4]. Thus ThO_2 based fuels are considered as a potential advanced fuel for Generation IV nuclear energy systems [5]. There are still a number of issues related to availability and accuracy of nuclear and material properties of thoria that would need to be resolved before its commercial use as a fuel can be foreseen [6].
In addition to previous facts, the main interests in ThO_2 as a nuclear fuel are its potential for burning weapon grade plutonium [7], high aqueous corrosion resistance, due to its very low solubility [8-9], its isomorphism with other tetravalent actinide dioxides and the production of lower amounts of minor actinides [10]. ThO_2 is generally mixed with other actinide oxides, because fissile isotope such as ^{233}U, ^{235}U or ^{239}Pu is needed to maintain the core critical until enough ^{233}U is generated. The sparingly soluble oxide can be disposed directly in the deep geological repository. However, as part of the safety assessment of the irradiated nuclear fuel, it is crucial to predict the behaviour of the ThO_2 and the release of radionuclides from the fuel.

Oxides like CeO_2 and ThO_2 carrying fluorite structure can be considered as structural analogues for the UO_2 matrix of spent nuclear fuel [11-15]. The radioactive and redox sensitive nature of UO_2 sets many limitations and challenges to handle such a material. ThO_2 can be considered as the structural analogue for UO_2 with natural alpha activity and it is also a non-redox sensitive oxide having only one prevailing redox state Th(IV) in nature. However, the ThO_2 is known to be even less soluble than the UO_2 [4].

ThO_2 surface dissolution evolution has been studied previously with XPS, SEM and AFM [2, 13, 19]. Results showed that the relatively fast initial dissolution took place at the "high energy surface sites" e.g. at the grain boundaries of the pellet matrix. After which the concentration of thorium in solution decreased noticeably and a layer formed on the surface of the pellet.

Vandenborre et al. [2] determined that 80% of the surface of the sintered ThO_2 was represented by less reactive crystalline thorium oxide grains. The remaining 20% was largely associated with grain boundaries and corresponded to the more reactive $ThO_{(x)}(OH)_{(y)}(H_2O)_{(z)}$. They suggested that the latter is involved in solid/solution exchange mechanisms. Corkhill et al. [13] have also shown that their data support "instant release" from the grain boundaries in dissolution studies with CeO_2 and ThO_2 analogues. The dissolution rate at grain boundaries of both oxides was correlating with the misorientation angle of the grain boundary, suggesting that the less stable grain boundaries dissolve faster.

In this study, the surface changes of ThO_2 pellets after dissolution experiments were analyzed by alpha spectrometry. In alpha spectrometry, radiochemical separations methods are normally used to produce less than 100 nm thin samples to optimize the energy resolution in measured alpha spectrum [20]. Thick samples make the analysis of radionuclides difficult or even hinder it, because alpha particles are events on the detector from varying depths of the sample producing considerable peak widening, resulting at the extreme in a rather step-like spectrum. AASI (Advanced Alpha Spectrometric Simulation) program has been developed by the Radiation and Nuclear Safety Authority of Finland for simulating the propagation of alpha particles in the earth's crust, air and the detector materials [21]. Using nondestructive direct alpha measurement together with the AASI simulation program, the factors influencing the shape of the detected alpha particle spectrum can be examined. This method has been used in a few studies related to either analysis of Thule particles [20] or analysis of air filters containing alpha emitting particles [22-23].

AASI is based on the Monte Carlo methods and derives the spectrum from large number of simulated initial decay events. Additionally, the program can be used for qualitative and quantitative analysis of alpha active sources containing comprehensive repertoire of isotopes. Geometry of the source medium and the distribution of the isotopes inside it can be varied, as well as the properties of the detector and distance between the source and detector. In addition, the alpha emissions from different depths in material layers can be calculated. During the simulation, the nuclide content and physical properties of the source are varied until parameters reproducing the measured source are found [20]. The prevalence of individual isotopes underneath the surface can be examined by studying the shape of the energy spectrum; the peaks and their tails, in detail and comparing measurements with the simulations [24].

In this work, the surfaces of ThO_2 pellets were studied by alpha spectrometry after the leaching experiment that was performed either in ^{229}Th tracer solution or reference solution without tracer. In addition, an intact ThO_2 pellet was analysed to compare the spectrum with the ones of leached pellets. The non-destructive analysis method uses Monte Carlo simulations to interpret the properties of the surface of the thick ThO_2 pellet. AASI program was used for qualitative analysis of the source giving information about proportions between ^{229}Th and ^{232}Th, and also their daughter nuclei. The aim of this study was to examine the probable formation of surface layer and layer thickness on the ThO_2 pellet with direct alpha spectroscopy and related simulations with AASI program. The layer most probably consist of hydrolysed thorium species, which are sparingly soluble and have high tendency to sorption onto surfaces [1, 3, 11].

2. Experimental

2.1 Dissolution experiments

The sintered ThO_2 pellets were made to meet an ideal composition and microstructure similar to the fluorite structure of UO_2 fuel. The fabrication procedure and characteristics of the pellets are described in detail in Myllykylä et al. 2015 [19]. The leaching experiments were conducted in 0.01 M NaCl solution using ^{229}Th spike (10^{-9}mol/L) with a single solid $^{232}ThO_2$ pellet (3.8 mm x 8.7 ø mm) in parallel with similar experiments without ^{229}Th spike for 534 days (see Table 1).

Table 1. The set-up for experimental $^{232}ThO_2$ pellet series of this study.

Experiment	Solid $^{232}ThO_2$	Mass of solid (g)	Solution	^{229}Th spike into solution
A	pellet	1.97	0.01 M NaCl	$1{\cdot}10^{-9}$ M
B	pellet	1.94	0.01 M NaCl	$1{\cdot}10^{-9}$ M
C	pellet	2.02	0.01 M NaCl	-
D	pellet	2.00	0.01 M NaCl	-
E	section of pellet	1.31	Not leached	-

The dissolution experiments were conducted within Ar glove box (O_2 in water < 0.15 ppb, $T = 25 \pm 1$ ºC) to allow the anaerobic conditions. The 0.01 M NaCl solution was diluted from stock solution (s.p. 99.99% NaCl by Merck) with argon purged MilliQ water under the glove box conditions. This was done three weeks before the start of the experiments to provide time for equilibration of the solution with the Ar atmosphere. The pH of the solution was adjusted to 6.5 with a small aliquot of 0.1 M NaOH. Prior to the experiments, 50 ml of 0.01 M NaCl solution was added with a volumetric flask to a PFA Teflon vessel (60 ml). To achieve the initial tracer concentration of 10^{-9} mol/L, 100 µl of ^{229}Th solution ($5{\cdot}10^{-7}$ mol/L) was added. The amount of nitric acid in tracer solution was neutralized with 31 µl of 0.1 M NaOH. The added aliquots were allowed to mix and equilibrate for 1 hour before the solid phase was added. 1.2 ml samples of leaching solution were taken after 0 and 1 hour, 1, 2, 6, 9, 19, 29, 40, 63, 78, 104 and 534 days. Sector field ICP-MS (Element2 by Thermo Scientific) was used to analyze the concentration of ^{232}Th and the isotopic ratio of ^{229}Th/^{232}Th in the solution. The ThO_2 pellet leaching experiments and solution phase analysis results are reported in detail in Myllykylä et al. 2016 [25]. The results showed relatively fast initial dissolution of $^{232}ThO_2$ was observed in the presence of excess of ^{229Th}, which was followed by significant decrease of ^{229}Th and ^{232}Th concentrations in 0.01 M NaCl solution. The results suggested that ^{229}Th precipitated or sorbed on the pellet and test vessel surfaces.

2.2 Direct alpha spectrometry

The ~3.8 mm thick $^{232}ThO_2$ pellets were analysed by direct alpha detection after the dissolution experiments (534 days). The pellets with ^{229}Th tracer solution are assigned as A and B, and those with reference solution without tracer as C and D (Table 1). In addition, an intact ThO_2 pellet (E) was analysed for comparison with the analyses of leached pellets. The measurements were conducted under vacuum with a Canberra 450 PIPS detector at a distance of ~9 mm. The data acquisition and analysis was done with the program MAESTRO for Windows Model A65-332. Energy calibration was performed with the reference sample containing ^{237}Np ($E_{\alpha1}$= 4788 keV, I= 47 %), ^{241}Am ($E_{\alpha1}$= 5486 keV, I= 84.5 %) and ^{244}Cm ($E_{\alpha1}$= 5805 keV, I= 76.4 %). Energy resolution for the calibration spectra was 25-35 keV depending the detector and vacuum chamber used for the measurements. In the measurements, the resolution varied between 23 and 48 keV (for samples A and B). Worse resolution was achieved for samples C, D and E, due to faulty signal amplifier. The measuring time varied between 6 – 117 hours. The geometrical efficiency of the measurement was about 0.19 ± 0.04. The background spectra, that were measured for 3-7 days were subtracted from the samples' alpha spectra. The measured background spectrum was scaled to the measuring time of sample spectrum.

The measured spectra were compared to the simulated spectra obtained with AASI-program. Table 2 presents the ^{232}Th and ^{229}Th series alpha daughters with their half-lives and alpha energies for the main peak. The energies were used to interpret the peaks and steps in the measured spectra (Figures 5, 6A and 6 B).

Table 2. Half lives and alpha energies of the main peaks of ^{232}Th and ^{229}Th and the following alpha dauhgter nuclides in their decay chains. [26]

Nuclide	Half-life	Main E_α (keV)	Nuclide	Half-life	Main E_α (keV)
^{232}Th	1.40x10^{10} y	4012	^{229}Th	7340 y	4845
^{228}Th	1.9125 y	5423	^{225}Ac	10.0 d	5830
^{224}Ra	3.66 d	5685	^{221}Fr	4.9 m	6341
^{212}Bi	60.55 m	6050	^{217}At	32.3 ms	7067
^{220}Rn	55.6 s	6288	^{213}Po	3.7 µs	8375
^{216}Po	0.145 s	6778			
^{212}Po	0.299 µs	8784			

2.3 Advanced Alpha-spectrometric Simulation (AASI) of the alpha step spectra

AASI program has been developed for simulating the propagation of alpha particles in the solid medium [24]. Most of the alpha particles coming from the ThO_2 pellets are absorbed inside the solid matrix and therefore a well-defined simulation is crucial for analysing the expected step type spectra coming from the thick pellets. Figure 1 describes the stopping power of thorium dioxide, which is needed in simulations to evaluate the path lengths and continuous energy loss of particles in matrix material. The stopping power is not linear, and the particles with higher energy penetrate much further as can be seen from the Figure 1.

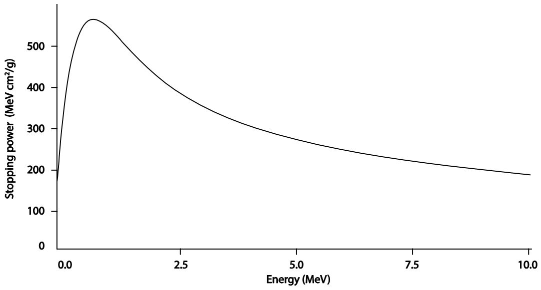

Figure 1. Stopping power information for ThO_2 created with AASI.

The highest and lowest main alpha peak energies in the thorium decay series are for ^{212}Po (E_α = 8.785 MeV) and for ^{232}Th (E_α = 4.012 MeV), respectively. According to calculations with the SRIM program [27] the ranges of these alphas in ThO_2 are about 28 µm and 9 µm, respectively. Figures 2A and B show the spectra of two alpha energies originating from different depths. The spectrum from an almost ideal, near massless alpha source (surface) is clearly peak shaped. The figure 2B shows also how the shape of measured alpha spectrum changes when alpha particles pass through the material layers of different thicknesses (1, 10, 25 µm). The spectra are produced using the AASI simulation program. When measuring a thick alpha sample, the observed spectrum is a composite of the spectra of alpha particles originating from all different depths in a sample; from the surface to a depth of maximum range of the particle. Therefore, the resulting spectrum consists of steps, instead of peaks, rising at the alpha energies of the nuclides in the sample.

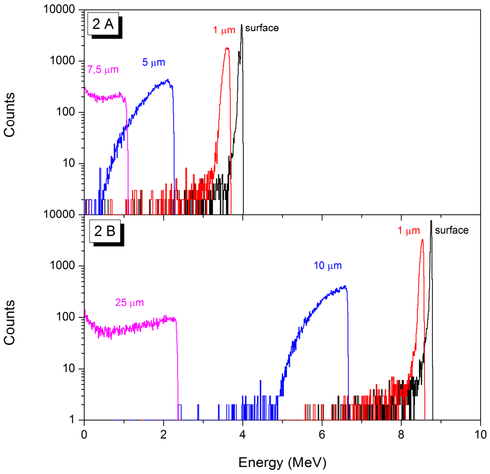

Figure 2. Simulated alpha spectra from ^{232}Th source on the surface of a ThO_2 sample and below a layer of 1, 5 and 7.5 µm of ThO_2 (2A). In comparison, the simulated alpha spectra of ^{212}Po source on the surface of a ThO_2 sample and below a layer of 1, 10 and 25 µm of ThO_2 (2B).

To demonstrate a step-like spectrum from a thick source, figure 3A shows simulated ^{229}Th spectra from different thicknesses of ThO_2 layer, assuming that ^{229}Th is evenly distributed in the layer. In figure 3B similar spectra are shown but originating from three different alpha-emitting nuclides and assuming three different thicknesses for ^{229}Th containing layer.

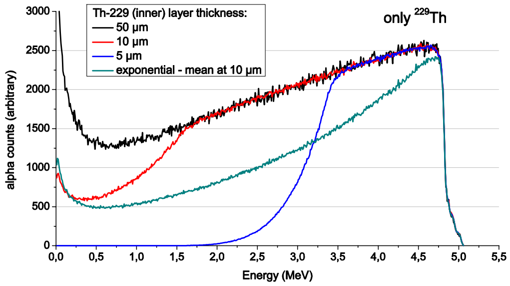

Figure 3A. Spectra of ^{229}Th isotope from ThO_2 samples with different thicknesses of ^{229}Th layers.

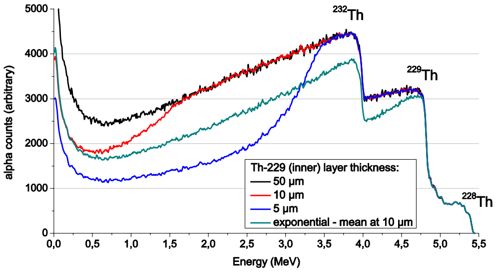

Figure 3B. Spectra of three thorium isotopes from $^{232}ThO_2$ samples with different thicknesses of ^{229}Th layers.

Figure 4 shows an AASI simulation where the concentrations of isotopes are varied within depth from homogenous in the black spectrum to the blue and red spectra where the ^{228}Th and ^{229}Th concentrations in the topmost 0.1 µm are 10 and 2 times, respectively, higher than in the ThO_2 matrix below. Narrow peaks at the top of the step spectrum indicate concentrated amounts of isotopes in a thin layer of the surface of the bulk ThO_2 matrix.

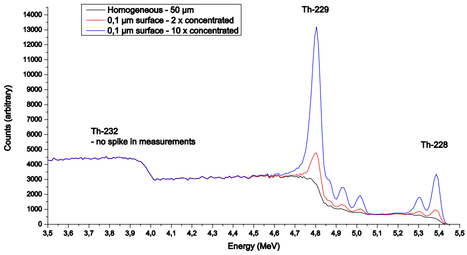

Figure 4. The effect of concentration of $^{228,229}Th$ nuclides on the surface of the ThO_2 sample on the observed alpha spectrum.

When analyzing the alpha spectra of the measured leached ThO_2 pellets, AASI simulation program was utilized to find the radionuclide content and the distribution of radionuclides in the sample. In simulations, the sample was divided into two parts: a thin layer assumed to have formed on the surface of the pellet and the ThO_2 matrix below it. First, the parameters for the detector were found by fitting the simulated spectrum to a measured calibration spectrum. After that a simulated spectrum was fit to a measured spectrum of a ThO_2 pellet by changing the thickness of the surface layer and the equilibrium state in the decay chain of ^{232}Th series isotopes, until the qualitative match was obtained.

3. Results and discussions

Figure 5 shows the measured background-subtracted spectra of intact ThO_2 pellet sample E and of pellet C, which was leached in 0.01 M NaCl solution for 534 days. The pellet E was measured for 1.0 hours and pellet C for 0.6 hours. The resolution of the measurements (E and C) had worse quality due to faulty amplifier. The spectrum of the intact pellet shows only the step like characteristics of mother nuclide ^{232}Th and its daughters ending to ^{212}Po.The spectrum of leached pellet shows detectable peaks diverging from step spectrum, which are not seen in the spectrum of the bulk intact thorium oxide sample. The peaks in the spectrum of the leached sample indicate the increased amounts of daughter nuclides (^{228}Th, ^{224}Ra, ^{220}Rn, ^{216}Po, ^{212}Po) at the surface of the pellet indicating chemical processes occurring on the surface during the leaching experiment.

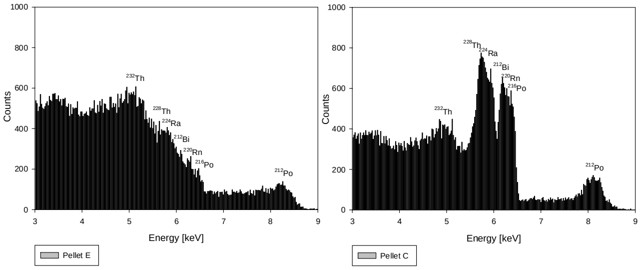

Figure 5. The measured spectra of intact ThO_2 pellet E and of ThO_2 pellet C leached in 0.01 M NaCl.

Figure 6A presents the analysed background-subtracted spectrum for ThO_2 pellet leached in the presence of ^{229}Th. The pellet A was measured for 116 hours. The amount of observed counts, frequency of decay events, in the spectrum is dependent of nuclides half-live; the shorter the half-live, the higher amount of counts received at the energy of alpha daughter when the amount of decaying atoms is same. In the measured spectrum there is a clear step-like structure for both decay chains of ^{232}Th and ^{229}Th as illustrated in Figure 6B. Alpha peaks of ^{229}Th and daughter nuclides of ^{232}Th and ^{229}Th are identified above the step spectra except for the ^{232}Th no peak is present. The sharp ^{232}Th peak is absent due to its homogenous distribution in layer and bulk, and very low activity (long $t_{1/2}$).

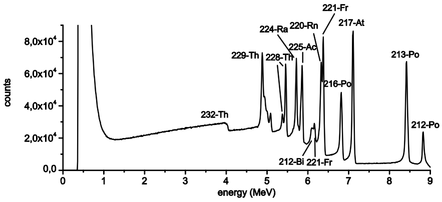

Figure 6A. The measured spectrum for ThO_2 pellet A showing the step for ^{232}Th and ^{229}Th including also the peaks and steps for daughter nuclides of both decay series (^{232}Th, ^{229}Th).

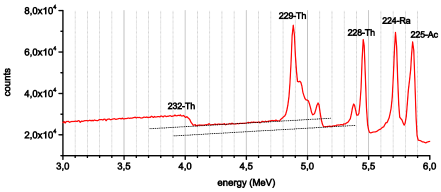

Figure 6B. The measured spectrum for ThO_2 pellet A, in which the black lines are illustrating the step like spectrum of thick sample underneath the peak spectrum of the surface layer.

From the spectra (Fig. 6A), it can be deduced that ^{232}Th isotope is spread homogeneously throughout the medium. The step like characteristics of ^{229}Th and its daughters indicates penetration into the $^{232}ThO_2$ bulk pellet beneath the surface layer. In the following, these findings are examined in more detail with simulations.

Figure 7 shows the simulated spectrum of intact and homogenous ThO_2 pellet including daughter nuclides. As can be seen the simulation appears as rough step- like spectrum without any clear peaks, continuing to the last unstable alpha-active isotope with extremely short half-life. The energy calibration of pellets E and C shifted slightly during the analysis due to faulty amplifier and the fitting of simulations to the actual measured spectra was challenging. This can be seen in difference in a step of ^{212}Po.

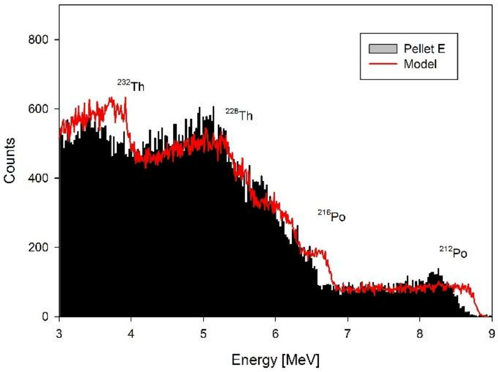

Figure 7. Simulated spectrum of intact $^{232}ThO_2$ sample, pellet E (red) accompanied with the histogram of measured spectrum (black).

Table 3 presents the parameters that were used for calculating geometric efficiency for simulations of pellet E and A.

Table 3. The parameters required to run the simulations and calculate the geometrical efficinecy of the measuments.

	Density [g/cm3]	Distance [mm] (source to detector)	Pellet diameter and thickness [mm]	Geometrical efficiency
Pellet A	9.3	8.8	8.67	0.20±0.03
Pellet E	8.81	8.99	8.74	0.19±0.03

Figure 8 shows the measured and simulated spectra of pellet A. Separate simulations were run for the bulk medium and the 0.1 µm thick surface layer. This allowed better scaling for the spectrum for comparing the simulations and measurements as the concentrations in the bulk medium nor surface layer were known. In simulation the surface layer contained ^{229}Th and all α daughter nuclides of ^{229}Th and ^{232}Th. The bulk of the pellet contained ^{232}Th and following daughters, as well as noticeable amount of ^{229}Th and its daughters. Furthermore, simulations were run with following equilibrium assumptions; ^{229}Th and daughter nuclei (^{225}Ac, ^{221}Fr, ^{217}At, ^{213}Bi, ^{213}Po) were simulated in equilibrium and taking into account the alpha branching of 2.1 percent for ^{213}Bi. The age or history of ThO_2 powder, the starting material for pellets, was unclear. The activity of ^{232}Th (100 %) was assumed to be twice as much compared to the alpha decaying daughter nuclei (^{228}Th, ^{224}Ra, ^{220}Rn, ^{216}Po, ^{212}Bi, ^{212}Po; 50%). The daughter nuclides were simulated in equilibrium among themselves, taking into account the alpha branching of ^{213}Bi to be 35.94 percent. One more thing that has to be taken into account in simulations is the fact that one of the daughter nuclides exists as a gas namely ^{220}Rn and the relative concentration of the following daughter are slightly lower. The relative concentrations and layer thicknesses were fitted by iterative simulations as illustrated in section 2.3.

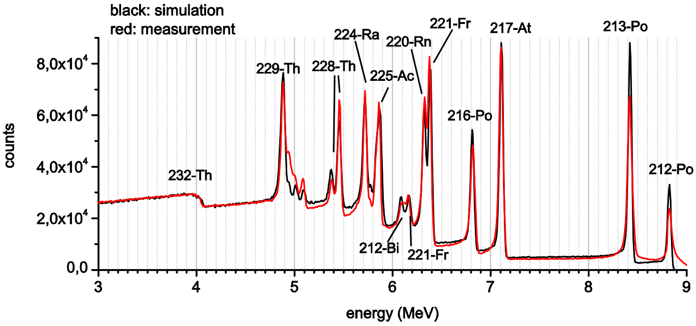

Figure 8. Measured (red) and simulated (black) spectra of the ^{232}ThO$_2$ pellet A with the concentrated layer of ^{229}Th on top of the pellet.

Thin layer was simulated to be maximum as 0.1 µm thick describing the thin precipitate. Thinner medium did not give better fit to measurements because of the limited energy resolution of the detectors. The thicker layer started to widen the peaks. Proportion between ^{232}Th and ^{228}Th was varied in simulation, as the half-life of ^{228}Ra, daughter nuclide of ^{232}Th, is relatively long (5.75 years) compared to the assumed age, 30-50 years, of the ^{232}ThO$_2$ pellet material. All daughter nuclei after ^{228}Th were considered to be in secular equilibrium as their longest T$_{1/2}$ is 3.6 days.

The surface layer very likely contains mostly ^{232}Th even though the clear alpha peak of ^{232}Th cannot be seen because of its homogenous nature to bulk ^{232}ThO$_2$ beneath the surface. In the imaginary case, in which the surface would have the even activities of ^{232}Th and ^{229}Th the quantity of ^{229}Th would be only 0.00005% of the total amount of Th atoms. Even if the activity of ^{229}Th would be 100 times that of ^{232}Th the share of atoms on the surface layer is only 0.005%

Direct alpha spectrometry on ^{232}ThO$_2$ pellets accompanied with AASI simulations supported the assumption of formation of Th precipitation on the ThO$_2$ pellet surface, which was obtained in the previous leaching experiments [25]. In the experiments, the relatively fast initial dissolution of ^{232}ThO$_2$ was observed in the presence of excess of ^{229}Th in 0.01 M NaCl solution in the leaching experiments [25]. In these experiments the initial dissolution was followed by significant decrease of ^{229}Th and ^{232}Th concentrations down to 10^{-10} mol/L within 20 days, suggesting the precipitation or sorption to occur.

4. Conclusions

The direct alpha measurement with Advanced Alpha Spectrometric Simulation turned out to be valuable technique, when studying the dissolution/precipitation behavior of ThO$_2$. The used methods gave information not only of the thorium isotopes present but also the behavior of daughter nuclides, owing different chemistry to mother nuclide. The concentrations of daughter nuclides of ^{232}Th and ^{229}Th were detectable only by alpha spectrometry. The direct alpha measurement found to be a useful tool to study ThO$_2$, the analogue material of spent nuclear fuel, which also contains numerous isotopes of different elements incorporated into the grains or grain boundaries of UO$_2$ matrix.

The alpha measurements showed concentrated amount of daughter nuclides in the surface of leached pellets in comparison to the intact ThO$_2$ pellet. In the ^{229}Th tracer experiment, the concentrated layer containing ^{229}Th and daughter nuclides from both ^{229}Th, ^{232}Th decay series was simulated to be less than 0.1 µm thick on the pellet surface. The narrow peaks above of step like spectra indicate the layer to be extremely thin. The existence of step like characteristics of ^{229}Th and its daughters suggest their intrusion also below the thin surface layer into the bulk ThO$_2$. Because of the energetically less stable nature of the grain boundaries, they are the most probable route for ^{229}Th and its daughter nuclides to intrude deeper into the bulk of ^{232}ThO$_2$ pellet below the <0.1 µm surface layer. The formation of solid solution in the ThO$_2$ matrix cannot be excluded totally. However, the fact that all the daughter nuclides of ^{229}Th showed step like characteristics in alpha spectrum indicates that the route or mechanism for intrusion would be same for all nuclides. The isotopic exchange between ^{229}Th and ^{232}Th could be one possible mechanism for the observation, but prevailing secular equilibrium of ^{229}Th and its daughters does not support this hypothesis.

An attempt was made to measure the depth profiles of thorium isotopes in the surface layer to evaluate the actual thickness of thin ^{229}Th layer. The ThO_2 pellet samples were studied with Secondary Ion Mass Spectrometry (SIMS) using a double focusing magnetic sector instrument VG Ionex IX-70S. A 12 keV Cs+ primary beam was used and aim was to measure the intensities of the negative secondary ions at m/z values of ^{16}O, ^{208}Pb, ^{229}Th and ^{232}Th. The sample was at -6kV potential during the analysis. In addition, an electron beam was applied in order to avoid charging up of the sample. However, SIMS analysis turned out to be very difficult (impossible) due to insulating nature of the sample and it was charging up during the ion bombardment.

In future plans, other methods like, Glow Discharge (GD-MS), which can measure isotopes on material surfaces at nm resolution or Time- of- Flight mass spectrometry (TOF-MS) could be tested to find out the actual depth of the ^{229}Th surface layer. Another interest is to study the chemical form of the layer.

Acknowledgements. This study has been a part of REDUPP project. The research leading to these results has received funding from the European Atomic Energy Community's Seventh Framework Programme (FP7) under grant agreement No. 269903. We thank Jaana Rantanen, who took part to the ICP analyses of Th. Martin Stennett and Neil Hyatt from Sheffield University, UK are acknowledged for the fabrication of the ThO_2 pellets. We thank companies Posiva, SKB, VTT, research program SAFIR2018 and YTERA doctroral school for partial finance of this study.

[1] J. Vandenborre, A. Abdelouas, B. Grambow, Discrepancies in Thorium Oxide Solubility Values: a new experimental approach to improve understanding of oxide surface solid/solution. RadioChim. Acta. 96 (2008) 515-520.

[2] J. Vandenborre, B. Grambow, A. Abdelouas, Discrepancies in Thorium Oxide Solubility Values: Study of Attachment/Detachment Processes at the Solid/Solution Interface. Inorg. Chem. 49 No. 19 (2010) 8736-8748.

[3] V. Neck, J. Kim, Solubility and hydrolysis of tetravalent actinides. Radiochim. Acta. 89 (2001) 1-16.

[4] V. Dekoussar, G.R. Dyck, A.Galperin, C. Ganguly, M. Todosow, M. Yamawaki, Thorium fuel cycle – Potential benefits and challenges. IAEA, IAEA-TECDOC-1450, Vienna, 2005.

[5] G. Heisbourg, S. Hubert, N. Dacheux, J. Purans, Kinetic and thermodynamic studies of the dissolution of thoria-urania solid solutions. Journal of Nuclear Materials. 335 (2004) 5-13.

[6] Advanced Fuel Pellet Materials and Fuel Rod Design for Water Cooled Reactors, IAEA TECDOC-1654, p 165.

[7] H.T. Akie, T. Muromura, H. Takano, S. Matsuura, A New Fuel Material for Once-Through Weapons Plutonium Burning, Nucl. Techol., 107 (1994) 182-192.

[8] B. Fourest, T. Vincent, G. Lagarde, S. Hubert, P. Baudoin, Long-term behaviour of a thorium-based fuel, J. Nucl. Mater. 282 (2000), 180-185.

[9] S. Hubert, K. Barthelet, B. Fourest, G. Lagarde, N. Dacheux, N. Baglan, Influence of the precursor and the calcination temperature on the dissolution of thorium dioxide, J. Nucl. Mater., 297, 2 (2001) 206-213.

[10]. B. Fourest, S. Hubert, G. Lagarde, T. Vincent, Thorium as a waste management option: residual risk of final disposal, project report nuclear Science and technology, edited by H. Gruppelaar, J.P. Schapira EUR19142 (2000)

[11] L.R. Morss, N.M. Edelstein, J. Fuger, J.J. Katz,The chemistry of the actinide and transactinide elements. (2006) Springer, New York

[12] M. C. Stennett, C.L Corkhill, L. A. Marshall, N.C.Hyatt, Preparation, Characterisation and Dissolution of a CeO_2 Analogue for UO_2 Nuclear Fuel, J. Nucl. Mater, 432 (2013) 182 –188.

[13] C. Corkhill, E. Myllykylä, D. Bailey, S. Thornber, J. Qi, P. Maldonado, M. Stennett, A. Hamilton, N.C. Hyatt, The contribution of energetically reactive surface features to the dissolution of CeO_2 and ThO_2 analogues for spent nuclear fuel, ACS Applied Materials & Interfaces. ACS Applied Materials & Interfaces. 6 (2014) 12279−12289

[14] L. Claparende, N. Clavier, N. Dacheux, P. Moisy, R. Podor, J. Ravaux, Influence of crystallization state and microstructure on the chemical durability of Cerium-Neodymium mixed oxides, Inorg. Chem. 50 (2011) 9059-9072.

[15] P.D. Edmonson, Y, Zhang, S. Moll, F. Navamar, W.J Weber, Irradiadiation effects om microstructure change in nanocrystalline ceria – Phase, lattice stress, grain size and grain boundaries, Acta Materialia 60 (2012) 5408-5416

[16] J. Fuger, M. Rand, I. Grenthe, V. Neck, D. Rai, *Chemical Thermodynamics of Thorium,* OECD Nuclear Energy Agency. (2007)

[17] V. Neck, R. Müller, M. Bouby, M. Altmaier, J. Rothe, M.A. Denecke, J.I. Kim, Solubility of amorphous Th(IV) hydroxide – application of LIBD to determine the solubility product and EXAFS for aqueous speciation. Radiochim. Acta, 90 (2002) 485 –494.

[18] V. Neck, M. Altmaier, R Müller, A Bauer, T. Fanghänel, J.I. Kim, Solubility if crystalline thorium dioxide, Radiochim. Acta, 91, (2003) 253-262.

[19] E. Myllykylä, T. Lavonen, M. Stennett, C. Corkhill, K. Ollila, and N.Hyatt: Solution composition and particle size effects on the dissolution and solubility of a ThO_2 microstructural analogue for UO_2 matrix of nuclear fuel Radiochim. Acta; 103(8) (2015) 565–576.

[20] R. Pöllänen, T. Siiskonen, M. Moring, J. Juhanoja, Direct alpha spectrometry for charactherising hot particle properties, Radiation Measurements, 4, 10 (2007) 1666–1673.

[21] T. Siiskonen, R. Pöllänen, Advanced simulation code for alpha spectrometry, Nuclear Instruments and Methods in Physics Research Section A: Accelerators, Spectrometers, Detectors and Associated Equipment, 550, 1–2 (2005) 425–434.

[22] R. Pöllänen, T. Siiskonen, Minimum detectable activity concentration in direct alpha spectrometry from outdoor air samples: continuous monitoring versus separate sampling and counting, Health Physics, 90 (2006) 167-175.

[23] R. Pöllänen, T. Siiskonen, High-resolution alpha spectrometry under field conditions – fast identification of alpha particle emitting radionuclides from air samples, Journal of Environ-mental Radioactivity, 87 (2006) 279-288.

[24] T. Siiskonen, R. Pöllänen, New approach to alpha spectrum analysis: Iterative Monte Carlo simulations and fitting, Progress in Nuclear Science and Technology, 2 (2011) 437-441. ¨

[25] E. Myllykylä, T. Lavonen, L. Koivula, K.Ollila, M. Siitari-Kauppi, Dissolution of Crystalline ThO_2: study of dissolution process with initial ^{229}Th spike, Journal of Radioanalytical & Nuclear Chemistry, 2017, 311(1): 225-235

[26]] NuDat 2.6 database, available in http://www.nndc.bnl.gov/ nudat2/. Accessed 21 of October 2016

[27] James F. Ziegler, Jochen P. Biersack, Matthias D. Ziegler: SRIM, The Stopping and Range of Ions in Matter, www.srim.org

[*] Correspondence author (e-mail:emmi.myllykyla@vtt.fi)

Series title and number

VTT Science 156

Title	**Investigation of ThO2 as a structural analogue for spent nuclear fuel dissolution under repository conditions**
Author(s)	Emmi Myllykylä
Abstract	Currently, the preferred option for the long-term disposal of spent nuclear fuel (SNF) in Finland and Sweden is disposal in a geological repository. In deep bedrock, the release of Th, U and other radionuclides through man-made barriers and the geo- and biosphere will be controlled by the dissolution of the fuel by groundwater. Thorium dioxide is isostructural to uranium dioxide, sharing the same fluorite structure (space group Fm3m) and making it a useful analogue material for nuclear fuel, which mainly consists of UO_2 (>95%). This thesis aimed to investigate the dissolution of ThO_2, which was synthesised to approximate as closely as possible the microstructure of UO_2 in a nuclear fuel matrix. The investigation consists of dissolution studies conducted using pellets, fragments (2 to 4 mm) and particles (80 to 160 µm) of $^{232}ThO_2$. The evolution of dissolving surfaces and grain boundaries were examined by combining different microscope imaging techniques (scanning electron microscopy (SEM), atomic force microscopy (AFM), SEM with electron backscattering diffraction detector (SEM-EBSD) and profilometer imaging). High resolution inductively coupled plasma mass spectrometer (HR-ICP-MS) was used for analyses of low thorium concentrations in leaching solutions. Part of the dissolution experiments were conducted in the presence of a ^{229}Th tracer to gain additional data on the dissolution and precipitation by following the change in isotopic ratio $^{229}Th/^{232}Th$. Furthermore, the pellets from these experiments were measured with direct alpha spectrometry to estimate the contents and thickness of the ^{229}Th-rich layer formed on the pellet surface. The results of all dissolution studies showed a relatively fast release of thorium during the early stage of the experiment followed by a slow decrease in the thorium concentration and suppression of the dissolution rate. The fast intial release most likely occurs due to "high energy surface site" (grain boundaries and defects sites) dissolution. Microscopic tehniques and direct alpha measurument gave evidence of formation of the dissolution suppressing surface layer. Temporal variation between the non-filtered and ultrafiltered solutions indicated that colloids play a role in experimental conditions.
ISBN, ISSN, URN	ISBN 978-951-38-8547-2 (Soft back ed.) ISBN 978-951-38-8546-5 (URL: http://www.vttresearch.com/impact/publications) ISSN-L 2242-119X ISSN 2242-119X (Print) ISSN 2242-1203 (Online) http://urn.fi/URN:ISBN:978-951-38-8546-5
Date	June 2017
Language	English, Finnish abstract
Pages	68 p. + app. 54 p.
Name of the project	
Commissioned by	
Keywords	ThO2, thorium, microstructure, dissolution, solubility, nuclear fuel, UO2
Publisher	VTT Technical Research Centre of Finland Ltd P.O. Box 1000, FI-02044 VTT, Finland, Tel. 020 722 111

Julkaisun sarja ja numero

VTT Science 156

Nimeke	**Käytetyn ydinpolttoaineen liukoisuus loppusijoitusolosuhteissa käyttäen toriumoksidia polttoaineanalogiana**
Tekijä(t)	Emmi Myllykylä
Tiivistelmä	Tällä hetkellä geologinen loppusijoitus on todennäköisin vaihtoehto käytetylle ydinpolttoaineelle niin Suomessa kuin Ruotsissakin. Sama konsepti on potentiaalinen myös mahdollisille tulevaisuuden torium-pohjaisille polttoaineille. Polttoaineen liukoisuus pohjaveteen määrää uraanin, toriumin ja muiden radionuklidien vapautumista eri vapautumisesteiden ja geosfäärin läpi aina biosfääriin asti. Toriumdioksidilla (ThO_2) on samanlainen fluoriittityypin kiderakenne kuin uraanidioksidilla. Tämän takia ThO_2:a voidaan käyttää analogimateriaalina myös tutkimuksissa, jotka koskevat pääosin uraanioksidista (UO_2 > 95 %) koostuvaa polttoainetta. Tämän väitöskirjan päämääränä oli tehdä liukoisuustutkimuksia sellaisella syntetisoidulla toriumoksidilla, jonka mikrorakenne muistuttaa mahdollisimman tarkasti käytetyn polttoaineen UO_2:n mikrorakennetta. Tutkimus sisältää ThO_2-pelleteillä, -murskeilla (2 - 4 mm) ja -partikkeleilla (80 - 160 µm) tehtyjä liukenemiskokeita. Liukenevien pintojen ja raerajojen kehittymistä/muuntumista liuotuskokeissa seurattiin erilaisin mikroskooppisin kuvantamistekniikoin (elektronimikroskopia (SEM), atomivoimamikroskopia (AFM), SEM-mikroskopia varustettuna elektronien takaisinsirontadiffraktiodetektorilla (SEM-EBSD) ja profilometrinen kuvantaminen). Osa liukenemiskokeista tehtiin siten, että liuosfaasiin oli lisätty ^{229}Th- merkkiainetta, jotta saataisiin lisätietoa liukenemisesta ja saostumisesta seuraamalla ^{229}Th/^{232}Th -isotooppisuhdetta. Merkkiainekokeista saatujen pellettien pinnan koostumusta ja muodostuneen pintakerroksen paksuutta arvioitiin mittaamalla ja mallintamalla alfaspektri suoraan pellettien pinnasta. Kaikki liukoisuuskokeet osoittivat, että torium liukenee suhteellisen nopeasti kokeiden alkuvaiheessa. Alkua seuraa toriumkonsentraatioiden hidas lasku liuoksessa ja liukoisuuden väheneminen. Nopea vapautuminen tapahtuu todennäköisesti niin kutsutuilta "korkean energian" paikoilta kuten raerajoilta ja kidevirhepaikoilta. Mikroskopiatutkimukset ja suora alfaspektrometrinen mittaus antoivat näyttöä myös siitä, että pintaan muodostuu liukenemista hidastava pintakerros. Suodatettujen ja suodattamattomien liuosnäytteiden konsentraatioissa havaittiin eroja kokeiden aikana, mikä indikoi, että kolloideilla on rooli liuoskemiassa.
ISBN, ISSN, URN	ISBN 978-951-38-8547-2 (nid.) ISBN 978-951-38-8546-5 (URL: http://www.vtt.fi/julkaisut) ISSN-L 2242-119X ISSN 2242-119X (Painettu) ISSN 2242-1203 (Verkkojulkaisu) http://urn.fi/URN:ISBN:978-951-38-8546-5
Julkaisuaika	Kesäkuu 2017
Kieli	Englanti, suomenkielinen tiivistelmä
Sivumäärä	68 s. + liitt. 54 s.
Projektin nimi	
Rahoittajat	
Avainsanat	ThO2, torium, mikrorakenne, liukeneminen, liukoisuus, ydinpolttoaine, UO2
Julkaisija	Teknologian tutkimuskeskus VTT Oy PL 1000, 02044 VTT, puh. 020 722 111

VTT SCIENCE 156

Investigation of ThO2 as a structural analogue for...

Investigation of ThO2 as a structural analogue for spent nuclear fuel dissolution under repository conditions

Currently, the preferred option for the long-term disposal of spent nuclear fuel (SNF) in Finland and Sweden is disposal in a geological repository. In deep bedrock, the release of Th, U and other radionuclides through man-made barriers and the geo- and biosphere will be controlled by the dissolution of the fuel by groundwater. Thorium dioxide is isostructural to uranium dioxide, sharing the same fluorite structure (space group Fm3m) and making it a useful analogue material for nuclear fuel, which mainly consists of UO_2 (>95%).

This thesis aimed to investigate the dissolution of ThO_2, which was synthesised to approximate as closely as possible the microstructure of UO_2 in a nuclear fuel matrix. The investigation consists of dissolution studies conducted using pellets, fragments (2 to 4 mm) and particles (80 to 160 µm) of $^{232}ThO_2$. The evolution of dissolving surfaces and grain boundaries were examined by combining different microscope imaging techniques (scanning electron microscopy (SEM), atomic force microscopy (AFM), SEM with electron backscattering diffraction detector (SEM-EBSD) and profilometer imaging). High resolution inductively coupled plasma mass spectrometer (HR-ICP-MS) was used for analyses of low thorium concentrations in leaching solutions. Part of the dissolution experiments were conducted in the presence of a ^{229}Th tracer to gain additional data on the dissolution and precipitation by following the change in isotopic ratio $^{229}Th/^{232}Th$. Furthermore, the pellets from these experiments were measured with direct alpha spectrometry to estimate the contents and thickness of the ^{229}Th-rich layer formed on the pellet surface.

ISBN 978-951-38-8547-2 (Soft back ed.)
ISBN 978-951-38-8546-5 (URL: http://www.vttresearch.com/impact/publications)
ISSN-L 2242-119X
ISSN 2242-119X (Print)
ISSN 2242-1203 (Online)
http://urn.fi/URN:ISBN:978-951-38-8546-5